5-3-2017

Modeling of Structural, Elastic, and Polar Properties of Organic and Inorganic Ferroelectrics

Fu-Chang Sun
fu-chang.sun@uconn.edu

Modeling of Structural, Elastic, and Polar Properties of Organic and Inorganic Ferroelectrics

Fu-Chang Sun, Ph.D.
University of Connecticut, 2017

ABSTRACT

Computational materials science has become an important branch of research with the advent of high performance computers and efficient algorithms. The viability of solving fundamental theories allows not only to understand experimental results, but predict properties of exotic materials or materials at extreme conditions. There exists fundamental theories that has been applied in different domains of length and time scales, where certain approximations are employed which enable improved performance with minimum compromise of accuracy.

In this Thesis, various computational approaches at different length scales are considered to investigate different classes of organic and inorganic ferroelectric materials to describe structural-property relations. The in-plane and out-of-plane piezoelectric properties of (001) strontium titanate ($SrTiO_3$, STO)

epitaxial thin films on pseudo-cubic (001) substrates are computed as a function of in-plane misfit strain. A nonlinear thermodynamic model is employed, which takes into account the appropriate mechanical boundary conditions, the electromechanical coupling between the polarization and the in-plane lattice mismatch, and the self-strains of the ferroelastic and ferroelectric phase transformations. The piezoelectric behavior of epitaxial STO films is described in various strain-induced ferroelectric phase fields in a temperature range from −50 to 50 °C. These results indicate that strain engineered STO films may be employed in a variety of sensor and actuator applications as well as surface acoustic wave devices and thin-film bulk acoustic resonators.

Implementing the same technique, piezoelectric properties of epitaxial (001) barium strontium titanate (BST) films are computed as functions of composition, misfit strain, and temperature using a non-linear thermodynamic model. Results show that through adjusting in-plane strains, a highly adaptive rhombohedral ferroelectric phase can be stabilized at room temperature with outstanding piezoelectric response exceeding those of lead based piezoceramics. Furthermore, by adjusting the composition and the in-plane misfit, an electrically tunable piezoelectric response can be obtained in the paraelectric state. These findings indicate that strain engineered BST films can be utilized in the development of electrically tunable and switchable surface and bulk acoustic wave resonators.

The theoretical model of ferroelectric bilayers using basic thermodynamics

taking into account the appropriate electrical boundary conditions and electrostatic fields is present. We show that ferroelectric multilayers are not simple capacitors in series (CIS) and treating these as CIS may lead to misinterpretation of experimental results and to erroneous conclusions. The spontaneous polarization mismatch in ferroelectric/ferroelectric (FE/FE), FE/paraelectric (FE/PE), and FE/dielectric (FE/DE) bilayers results in a non-linear electrostatic coupling which produces significant deviations in the overall dielectric response if it is computed using the simple capacitor-in-series (CIS) model. Our results show that the CIS approach is a good approximation only for DE/DE multilayers and for FE heterostructures if the individual layers are electrostatically screened from each other.

As a second method for this Thesis, classical molecular dynamics computations are considered to calculate the structural, elastic, and polar properties of crystalline ferroelectric β phase poly(vinylidene fluoride), PVDF, with randomized trifluoroethylene TrFE as a function of TrFE content. The results show that molecular dynamics can be used to predict the mechanical and polarization-related behavior of ferroelectric poly(VDF-*co*-TrFE). The same computational approach might be also utilized for other polymeric materials in the desired temperature and/or composition range. Furthermore, temperature-induced and deformation-induced phase transitions are reported, which are consistent with the experimental observation.

Finally, the fundamental theory of electron physics, also called the first-

principles formalism, is applied to study the polarization of the layered ferroelectric bismuth titanate (BiT). The electronic structure studies of pure BiT and technologically significant lanthanum-doped bismuth titanate (La-doped BiT) are performed. The results and the extension of current progress of A-site substitutional BiT using first-principle calculations could provide the theoretical evidence of the formation of oxygen vacancies, which is recognized to be associated with the leakage current and polarization properties. Studies on the optical properties of BiT are performed using a beyond-density functional theory (beyond-DFT) method. This is done because the regular approximation for electron-electron coupling in the DFT specific generalized gradient approximation (GGA) has limitations in predicting the band gap of semiconductors/insulators. The Heyd-Scuseria-Ernzerhof (HSE) screened hybrid-functional method is adopted.

Modeling of Structural, Elastic, and Polar Properties of Organic and Inorganic Ferroelectrics

Fu-Chang Sun

M.Sc. Physics, University at Buffalo, New York, USA, 2010

A Dissertation
Submitted in Partial Fulfillment of the
Requirements for the Degree of
Doctor of Philosophy
at the
University of Connecticut

2017

APPROVAL PAGE

Doctor of Philosophy Dissertation

Modeling of Structural, Elastic, and Polar Properties of Organic and Inorganic Ferroelectrics

Presented by
Fu-Chang Sun, M.Sc. Phys.

Major Advisor _____
S. Pamir Alpay

Associate Advisor _____
Gayanath W. Fernando

Associate Advisor _____
Niloy Dutta

University of Connecticut
2017

ACKNOWLEDGEMENTS

During the journey through my doctoral research, I have received tremendous support and encouragement from many people. It is very difficult to fully express my sincere gratitude, but I will do my best to put my appreciation into words. It is possible that I might have missed few people in the list below, but no doubt that I have benefitted from you all.

First of all, my sincere gratitude goes to my primary advisor Prof. Pamir Alpay, who provided invaluable advice and relentless support for years. Prof. Alpay not only cared about students' scientific achievements, but also encouraged them while they were away from work. I would consider myself lucky to have pursuit the beauty in science and knowledge through his direct and indirect assistance.

I would like to thank to my associate advisors Prof. Gayanath Fernando and Prof. Niloy Dutta for their cooperation and helpful guidance. I would always remember the time we have discussed physics – anywhere we ran into each other. My thanks also go to Prof. Serge Nakhmanson and Prof. Ilya Sochnikov for not only being my committee members, but also giving me lots of suggestions on improving my thesis. I had opportunity to collaborate with Prof. Serge Nakhmanson and it was a pleasant experience. I was benefitted by scientists from both physics (PHY) and materials science engineering (MSE) departments, including, but not limited to, Prof. Robin Côté, Prof. Gerald Dunne, Prof. Alex Asandei, Prof. Rampi Ramprasad, Prof. Avinash Dongare, Prof. Jason Hancock, Prof. Philip Mannheim, Prof. Susanne Yelin, and Prof. Thomas Blum. They have demonstrated the intellectual curiosity in science which has been an inspiration to me to go beyond the boundary.

I had a pleasant experience working with the group members of Dr. Alpay and others in the graduate school. To this end, I would like to thank Mehmet Kesim, Hamidreza Khassaf, Tulsi Patel, Yomery Espinal, Dr. Liang Dong, Dr. Jialan Zhang, Dr. Sanjubala Sahoo, and to the office mate Nasser Khakpash, Dr. Ching-Chang Chung, and Dr. Richard Pérez Moyet. We have met almost daily for years and exchange our thoughts on different aspects of our experiences, which became an important ingredient of my life. I appreciated their talent and dedication. Special thanks goes to Dr. Sanjeev Nayak, who joined the group about year ago but has made a great impact on this journey. We discussed physics, talked about science, shared the thoughts, and joked about lots of things. I also had a chance to meet good friends in both PHY and MSE departments. I would like to thank Sanka Piyadasa, who has been a nice friend since my first day at UConn. I really enjoyed the moments being with friends

and colleagues. These occasions do add sweetness to the otherwise tough PhD life.

I would like to thank my family and friends who have tolerated my absence from home and encourage me through my PhD. No matter if they are locally within US, or far away back home in Taiwan, my gratitude always remains for their support. My parents, parents-in-law, sister, brother, and sisters-in-law, need a special mention for spiritually supporting me and emotionally encouraging during the ups and downs. Because of them, I stand tall and proceed with confidence. Special thanks go to my sisters-in-law, Hsiu-Jiun Chang and Hsiu-Chiung Chang, who took good care of my son while I was busy and away from him. I would like to thank my son, Nate Sun, who is so cooperative and cheerful being with me.

None of the work in this thesis would have been accomplished without the warm support from my wife, Hsiu-Iun Chang. It is because of her love, support, and patience, I could go ahead in the pursuit of knowledge. With my head held high, I would like to dedicate my dissertation to my lovely wife and honor her sacrifice. There are too many people to thank, I render thanks to God.

TABLE OF CONTENTS

LIST OF FIGURES

Chapter 1
Methodology

In order to study the systems using computational approaches, suitable model should be considered as a prerequisite for the desired phenomena. The interactions are the essential ingredients for the recipe to accurately describe the materials properties. Depending on the time and length scales of the system, as long as the questions to ask, classical molecular dynamics and *ab initio* approaches are applied to investigate the ferroelectric materials behavior. Such approaches are well-established in the field and more advanced techniques are introduced to enhance its capability and accuracy in various topics. The following sections cover the basis understanding and current developments are also discussed.

1.1 Classical Molecular Dynamics

Molecular dynamics (MD) simulations become a standard and powerful computational tool for condensed matter physics, materials science, and biophysics disciplines. For chemical bonding and reactivity, molecular interaction, electrochemistry, and photochemistry, a MD simulations also provide a simplified formalism for tackling a very complicated system. Most of the

time, exact solution is not available. The experimental and theoretical works together usually offer in-depth knowledge while computations supply the insight into atomic scale process, and even predict experimental results. On the other hand, the experimentalist always need the explanation on their observations and verification of their thoughts. Here I would like to summarize a few key points which are necessary to carry out MD simulation. And bear that in mind, we may always want to see how the simulations work comparing to the experimental measurements, and want to know the underlying physics behind the seem-to-be no rule realistic system. Shortly speaking, there are two mathematical formalism concepts driving the classical MD simulations. One is the potential energy surface, associated with the atomic interacts between atoms. And the other one is force, which allows us to accelerate the atoms moving in the trajectory direction.

1.1.1 Interatomic Potentials

For a given system, we need to know the forces acting on the atoms, governed by Newton's second law, and forces are associated with the negative gradient of the potential.

$$m_i \ddot{\mathbf{r}}_\mathbf{i} = \mathbf{F}_i, \quad \mathbf{F}_i = -\frac{\partial}{\partial \mathbf{r}_i} U \tag{1.1.1}$$

where m_i represents the mass of i particle, $\ddot{\mathbf{r}}_i$ represents the acceleration of i particle, and $U(\mathbf{r}_i)$ represents the potential energy, as a function of atomic coor-

dinates $\mathbf{r}_i$. Depending on the complexity of the problem, in general, there are 1-body, 2-body, 3-body or n-dimensional type interactions, in the category of non-bonded interaction. One common method is to ignore the $n-$body, where $n \leq 3$, and only consider pair potential interaction. The essential idea might still be captured, even though pair potential seems to be a rather over-simplified approximation. Among all the pair interaction, Lennard-Jones potential, or $6-12$ potential, is considered as the most simple format. Although the simplicity of the formula, it is still being commonly used due to its well-representative and computational feasible form

$$v_{\mathrm{LJ}}(r) = 4\epsilon\Big[\Big(\frac{\sigma}{r}\Big)^{12} - \frac{\sigma}{r}\Big)^{6}\Big] \tag{1.1.2}$$

where ϵ represents the depth of the potential well (or the strength of the interaction), σ represents the distance at where the inter-particle potential is zero, and r represents the distance between the particles. If electrostatic charges are present in the system, there exists the Coulomb potentials

$$v_{\mathrm{Coulomb}}(r) = \frac{Q_1 Q_2}{4\pi\epsilon_0 r} \tag{1.1.3}$$

where Q_1 and Q_2 represent the charges, and ϵ_0 represents the permittivity of the free space. Again, depending on the system, the format might be modified to better describe the desired interaction.

For system contains molecular, we must consider another type of interac-

tion, the intramolecular bonding potential. The format of bonding interaction is more fruitful, but the most common ones can be categorized as bonds, bend angles, and torsional angles type.[6] Or,

$$
\begin{aligned}
E_{\text{bonds}} &= \frac{1}{2}\sum_{bonds} k^{r}_{ij}\Big(r_{ij} - r_{eq}\Big)^2 \\
E_{\text{angles}} &= \frac{1}{2}\sum_{angles} k^{\theta}_{ijk}\Big(\theta_{ijk} - \theta_{eq}\Big)^2 \\
E_{\text{torsionalangles}} &= \frac{1}{2}\sum_{tors.}\sum_{m} k^{\phi,m}_{ijkl}\Big(1 + cos(m\phi_{ijkl} - \gamma_m)\Big)
\end{aligned}
\tag{1.1.4}
$$

where $r_{ij} = |r_i - r_j|$ represents the distance between adjacent pairs of atoms in a molecular, the "bend angles" θ_{ijk} represents the angle between successive bond vectors r_{ij} and r_{jk}. The "torsion angles" ψ_{ijkl} represents the angle between three connected bonds, or mathematically

$$
\cos\phi_{ijkl} = -\hat{\mathbf{n}}_{ijk} \cdot \hat{\mathbf{n}}_{jkl}, \text{where } \mathbf{n}_{ijk} = \mathbf{r}_{ij} \times \mathbf{r}_{jk},\ \mathbf{n}_{jkl} = \mathbf{r}_{jk} \times \mathbf{r}_{kl} \tag{1.1.5}
$$

where $\hat{n} = \mathbf{n}/n$ represents the normalized unit vector perpendicular to the plane determined by two bonds.

In general, the energy term showing in Eq. 1.1.4 is oversimplified. Various simulation package possess their own format to represent the interaction, to different degree of accuracy. Since the force field potential, essentially, is constructed through parameterization. The simulation accuracy depends critically on the choice of parameters. For instance, the effect of electronic polarization isn't taken into account in fixed point charge model. Fixed bond topology

doesn't cover the chemical interaction, breaking or generate bonds. Fortunately, various technique can compensate some effect. For example, instead of considering the fixed charge for individual atom, partial charges might recover the polarization effects while parameterizing the force field potential. We emphasize the importance of the fitting parameters that parameterization follows the concept of "Garbage in, garbage out". Overall, the force field provides the potential energy and force gives the acceleration of the atoms, both integrating to the equations of motion.

For the detailed introduction of MD simulations in more fundamental level, I highly recommend the book from Daan Frenkel and Berend Smit's "Understanding Molecular Simulation"[7] and M. P. Allen, D. J. Tildesley "Computer Simulation of Liquids"[8]

1.1.2 Ensembles

In order to describe the state of the system, typically one uses temperature T, volume V, pressure P, and number of atoms N. These macroscopically observable variables are used and the systems can be described by ensemble, where the most common ones are canonical ensemble, microcanonical ensemble, and grand canonical ensemble. For canonical ensemble, it describes a system in contact with a heat bath where the number of particles is fixed and temperature is specified. A microcanonical ensembles represents a isolated system where the number of particles and total energy are fixed. A grand canonical

ensemble is used for a system contacting with a heat and particle bath, where heat and particles can be exchanged between the system and the surroundings. Depending on the criteria, the appropriate ensemble is considered for desired problem in hand.

1.1.3 Periodic Boundary Conditions

In this Thesis, the MD simulations are introduced to study the properties of a system in bulk, where the behavior is very differ to surface. The appropriate size of the simulation is essential to compromise the balance between the demanding of the resources and the accuracy of the computation. To eliminate the surface effect, where the particles interact differently at the surface region than at the bulk region, the simulation box is repeated throughout the space and form the infinite lattice. The particles behave exactly the same within one central unit box as the surrounding box. Thus if one particle moves out of the central box, the image of such particle moves into the box from the other side of the boundary. A schematic representation of two-dimensional periodic system is shown in Fig. 1.1.1. The number of particles in the central box remains the same throughout the simulations.

1.1.4 Thermodynamic Properties

Energy E, temperature T, and pressure P provide the connection between the microscopic and macroscopic level, such properties can be easily computed through classical molecular dynamics simulations. It is worth to emphasize

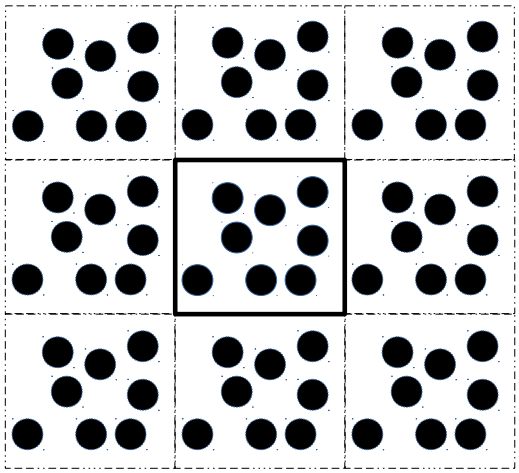

Figure 1.1.1: Periodic boundary conditions. The central box is defined by thicker lines.

that the average quantities are being computed, through Ergodic hypothesis where all accessible microstates are equally possible over a long period of time. A MD simulation should be sufficiently long so that the ensemble is properly sampled.

1.1.5 Conclusion

Even though the pioneer work of MD simulation can be traced by to 70s,[?] the development remains active especially in the field of biophysics, chemistry, and materials science. As addressed earlier, the most essential ingredient of a successful simulation is the representative potential. Empirical potentials have been frequently used in chemistry and materials physics. The interaction are taken into consideration by pair and many-body potentials. The matrix representation are implemented in semi-empirical potentials, where the matrix

elements are constructed through empirical fitting. Most of these potentials are within the region of classical mechanics, where the charge distribution remains the same throughout the entire simulation. This is not always the case in reality, while the chemical reactions and more accurate representation are necessary. Therefore quantum mechanical based method, such as density functional theory, is considered for taking electronic behavior into account. One can imagine that the computational demanding is much more higher so that the system is limited to fewer number of atoms. With the assistance of growing computational power, the system with few thousands of atoms become accessible and representative. The balance between computational cost and desired accuracy is the most critical factor, while simulation is involved.

1.2 Electronic Structure Calculations

Nowadays, the density functional theory (DFT) becomes the most favorable approach to investigate the electronic structure of materials, especially in the field including but not limited to materials science, condensed matter physics, chemistry, and most of the computational subdisciplines. The power to compute, or even predict the structural-property relationships has a huge impact on experimental fields, or even become the standard approach to interpret the experimental observation in the atomic scale. The great progress has been built up in computing the electronic structure, structural properties, chemical reaction, dielectric and optical properties, vibrational and thermody-

namic regime. The concept of DFT is based on the methodology by simplifying the many body problem into the one body problem by introducing functional– a function of another function. Instead of working explicitly how all the atoms interact with each other, the atoms now are considered interacting in the field, the electron density, and the reason how name of density functional theory is given.

Even though the great development in recent year, there are still lots of challenges standing ahead. For instance, the van der Waals interaction has been considered being very critical to determine the stability of DNA and protein structure. Not only in bio-related system, In solid,[9,10] in molecular self-assembly,[11] and in the process of adsorption,[12,13] the behavior are also highly depending on the van der Waals interaction. Moreover, using the single-particle approximation of density functional theory, an excited-state cannot be well described by the exchange-correlation energy term, which is unknown and can only be approximated by uniform electron gas.

1.2.1 Density Functional Theory

Here, we start our discussion by solving the time-independent Schrödinger equation

$$\left(\sum_{i=1}^{N}\left[-\frac{\hbar^2}{2m}\nabla_i^2 + V_{\text{ext}}(\mathbf{r}_i)\right] + \frac{1}{2}\sum_{i\neq j=1}^{N}\frac{e^2}{\left|\mathbf{r}_i - \mathbf{r}_j\right|}\right)\Psi(\mathbf{r}_1, \cdots, \mathbf{r}_N) = E\,\Psi(\mathbf{r}_1, \cdots, \mathbf{r}_N), \tag{1.2.1}$$

where $\mathbf{r}_i$ is the position of the i^{th} electron, N is the total number of electrons in the system, V_{ext} is the external field, and E is the total electronic energy. The Born-Oppenheimer approximation treats the electronic and the nuclear degrees of freedom as separable variables, where the assumption comes from the idea that the heavier nuclei should move way slower than the lighter electrons; each proton has more than 1800 times more mass than an electron. The eigenfunction Ψ contains $3N$ degrees of freedom and thus it is not possible to solve Eq. (1.2.1) in general. The electron-electron interaction term prohibits Eq. (1.2.1) to be expressed with reduced degrees of freedom. Therefore instead of solving the wave function as a many-body system using the Schrödinger's formalism, the Thomas-Fermi model, arise and develop on top of the idea of electronic density. For one particle with its corresponding wavefunction, the density can be considered as the probability to be found in real space, or

$$\rho(\mathbf{r}) = \psi^*(\mathbf{r})\psi(\mathbf{r}) \tag{1.2.2}$$

For a system with N particles, the density then can be written as

$$\rho(\mathbf{r}) = N \int \Psi^*(\mathbf{r}, \mathbf{r_2}, \ldots, \mathbf{r_N})\Psi(\mathbf{r}, \mathbf{r_2}, \ldots, \mathbf{r_N}) d\mathbf{r_2} \ldots d\mathbf{r_N} \tag{1.2.3}$$

and be interpreted as the probability amplitude to find any particle near the position $\mathbf{r}$ in real space. The essential idea of the Thomas-Fermi method is to avoid the discussion of the wavefunction, focusing on the density as a

variable. Although the idea is an important step in solving the equation, somehow the accuracy is limited because the expression of kinetic term is only an approximation. The method also doesn't include the exchange energy of atom, which is the essential conclusion of the Pauli principle.

1.2.2 The Hohenberg-Kohn Theorem

The idea of Hohenberg and Kohn theorem[14] is started from the argument that the movement of the electron is influenced by an external potential. In their theorem I, "The external potential, and hence the total energy, is a unique functional of the electron density." The Hamiltonian in Eq. (1.2.1) can be expressed and can be constructed by the charge density, hence, determining the total energy. One of the important message is that the Hohenberg-Kohn theorem shows the existence of functionals, but doesn't express how to obtain the functionals. The theorem II, "The ground-state energy can be obtained variationally, the density that minimizes the total energy is the exact ground-state density.", which can be proved by the variational principle. Even though it is a great progress and the extremely useful theorem, one still have no ability to compute the ground-state density. Fortunately, one year later Kohn and Sham[15] introduced a simple method for DFT calculations, where the feature of DFT remains persist. Suddenly, it becomes one of the most powerful computational method.

1.2.3 The Kohn-Sham Method

The central idea of Kohn-Sham method is that the full interacting system turns into a fictitious non-interacting system. Now instead of explicitly expression of the interaction, the electrons now move within the effective potential, namely "Kohn-Sham" single-particle potential. The advantage is that the calculations become feasible, with remaining the exact ground-state density as a real interacting system. The difference arise between the Kohn-Sham method and the Thomas-Fermi model by various format in kinetic energy term. In summary, a unique way of one to one mapping can be established to simplify the very difficult N interacting electrons problem into a solvable N non-interacting electrons problem. Instead of solving the N interacting system in an external potential, now the question becomes solving the N non-interacting electrons in an "external effective potential", where the charge density remains the same.

By mapping the problem from interacting electrons into a fictitious non-interacting electrons, the variational principle is applied with the Lagrange multiplier μ and the constrain of the total number of electrons to be N. The equation can be written as

$$\delta\Big[E_{\text{eff}}[\rho] + \int V_{\text{ext}}(\mathbf{r})\rho(\mathbf{r})d\mathbf{r} - \mu\Big(\int \rho(\mathbf{r})d\mathbf{r} - N\Big)\Big] = 0 \tag{1.2.1}$$

where $N = \int \rho(\mathbf{r})d\mathbf{r}$ is the number of electrons. Kohn and Sham separated $E_{\text{eff}}[\rho]$ into three terms

$$E_{\text{eff}}[\rho] = T[\rho] + \frac{1}{2}\int \frac{\rho(\mathbf{r})\rho(\mathbf{r}')}{|\mathbf{r}-\mathbf{r}'|}d\mathbf{r}d\mathbf{r}' + E_{XC}[\rho] \tag{1.2.2}$$

where $T[\rho]$ represents the kinetic energy of a non-interacting particles with density $\rho(\mathbf{r})$, the second term represents the classical electrostatic (Hartree) energy, and the last term $E_{XC}[\rho]$ represents the exchange-correlation energy which consists of non-classical electrostatic interaction energy and the different between the kinetic energies of both interacting and non-interacting systems. The first two terms in Eq. 1.2.2 can be simply handled but the trouble comes from the exchange correlation part. Combining with Eq. 1.2.1, one can re-write

$$\frac{\delta T[\rho]}{\delta \rho(\mathbf{r})} + V_{\text{eff}}(\mathbf{r}) = \mu \tag{1.2.3}$$

where effective potential is

$$V_{\text{eff}}(\mathbf{r}) = \int \frac{n(\mathbf{r}')}{|\mathbf{r} - \mathbf{r}'|} d\mathbf{r}' + V_{\text{XC}}(\mathbf{r}) + V_{\text{ext}}(\mathbf{r}) \tag{1.2.4}$$

and now the exchange-correlation potential becomes

$$V_{\text{XC}}(\mathbf{r}) = \frac{\delta E_{\text{XC}}[\rho]}{\delta \rho(\mathbf{r})} \tag{1.2.5}$$

By viewing N non-interacting particles move in another type of "effective" potential V_{eff}, the situation is the same as the real interacting system. To find the ground state energy, (or $\rho(\mathbf{r})$), now one can solve the non-interacting one-

electron Schrödinger equations, namely,

$$\left[-\frac{\hbar^2}{2m}\nabla^2 + V_{\text{eff}}(\mathbf{r})\right]\psi_i(\mathbf{r}) = \varepsilon_i\psi_i(\mathbf{r}) \tag{1.2.6}$$

$$\rho(\mathbf{r}) = 2\sum_{i=1}^{N}\left|\psi_i(\mathbf{r})\right|^2. \tag{1.2.7}$$

where V_{eff} represents the average potential be seen by electron i, $\psi_i(\mathbf{r})$ represents the one-electron wave function with 3 coordinates variables, the factor of 2 in Eq. 1.2.7 appears because electrons have spin and the Pauli exclusion principle says that two separate electrons having different spins can occupy one electron wavefunction, and ε_i represents the one-electron energy. The Eq. 1.2.6 is exact, if V_{eff} is known. Since it is not the case, V_{eff} is approximated. Depending on the system, the representative approximation of V_{eff} can provide very accurate results.

Because V_{eff} depends on $\rho(\mathbf{r})$ which is essential the solution of the equation, the Kohn-Sham equation are self-consistently. The workflow of solving the equation in Kohn-Sham formalism is as follows. First, one has to provide the initial guess of one-electron wave function $\psi_i(\mathbf{r})$. and solve the equation Eq. 1.2.6. Then new charge density is generated via Eq. 1.2.7. The comparison is made between new and old charge density. The self-consistent calculations go on until the difference is smaller than the desired tolerance, then we can further compute other physical quantities.

1.2.4 Local Density Approximation

Even though Kohn-Sham theory is exact in principle, the approximation is considered for the unknown exchange-correlation functional in practice. The first attempt of the approximation is called local density approximation (LDA),[15] where the density is treated locally as an uniformly distributed electron gas. At each point in the system, the exchange correlation energy term is the same as an uniform electron gas of the same charge density, and it can be expressed as

$$E_{\mathrm{XC}}^{\mathrm{LDA}} = \int \rho(\mathbf{r})\epsilon_{\mathrm{XC}}[\rho]d\mathbf{r} \tag{1.2.1}$$

where $\epsilon_{\mathrm{XC}}(\rho)$ is the exchange correlation energy per particle of an uniformly distributed electron gas of charge density ρ. The exchange correlation potential is given by

$$V_{\mathrm{XC}}^{\mathrm{LDA}}[\rho(\mathbf{r})] = \frac{\delta E_{\mathrm{XC}}^{\mathrm{LDA}}[\rho]}{\delta\rho(\mathbf{r})} = \epsilon_{\mathrm{XC}}[\rho] + \rho(\mathbf{r})\frac{\delta\epsilon_{\mathrm{XC}}[\rho]}{\delta\rho} \tag{1.2.2}$$

In practice, the $\epsilon_{\mathrm{XC}}[\rho]$ can be split into exchange and correlation potentials.[16–18]

1.2.5 Generalized Density Approximation

Despite the great success of LDA, there are limitations due to the nature of such approximation. For systems where the density slowly varies, LDA always provides a good result. However, an independent particles picture is no longer valid for strongly correlated systems so that LDA is not adequate. An improvement is established by considering both density and gradient of the

density as the argument of the exchange correlation energy, which is so-called generalized gradient approximation (GGA). Since there is no unique form to define the correlation energy term, PW91,[19] PBE,[20] and BLYP[21] are the most commonly accepted functionals by the DFT community.

1.2.6 Beyond DFT

Finally, for the cases that exchange correlation greatly dominates the system, such as unnegligible electron-phonon coupling,[22] and underestimation of electronic band gap,[23] accurate description is essentially important for the satisfactory results. Even though the determination of exchange correlation is still unclear, the development of hybrid functional[24] is still an active research of interest.[25] Beyond ground-state DFT, there is growing interest of research associated with excited state energies, such as charge transfer,[26,27] and time-dependent DFT (TDDFT).[28] Excited state properties such as emission, absorption, photochemical and photophysical phenomena, can therefore be systematically analyzed. The fundamental understanding of such approaches provide deeper insight of the complex systems, and help us to go beyond the boundary.[29]

1.2.7 Periodic Boundary Conditions and Bloch's Theorem

The N-body problems has been simplified to a single particle problem, but most of materials contain lots of electrons (in the order of 10^{23}). In practice, periodic potential is considered in Schrödinger equation to describe the crystal

structure for a solid system. The nuclei are arranged in a periodic manner, the electrons within such environment also behave with periodicity. The crystals can be exploited by Bloch's theorem stating the wavefunction of an electron within a periodic potential, where

$$\psi_k(\mathbf{r}) = u_k(\mathbf{r})e^{i\mathbf{k}\cdot\mathbf{r}} \tag{1.2.1}$$

where $u_k(\mathbf{r})$ is the function with the periodicity of the potential, *i.e.* $u_k(\mathbf{r}+\mathbf{T}) = u_k(\mathbf{r})$, where $\mathbf{T}$ is the length of the unit cell. $\mathbf{k}$ is a wavevector confined to the first Brillouin Zone. It implies that the probability of finding an electron at $\mathbf{r}$ is the same as its equivalent position $\mathbf{r}+\mathbf{T}$. The electron density is calculated through the integration over all possible $\mathbf{k}$, and it can be approximated with a summation containing sufficient amount of k points. Or,

$$\rho(\mathbf{r}) = \int |\psi_k(\mathbf{r})|^2 d^3\mathbf{k} \quad = \sum_k |\psi_k(\mathbf{r})|^2 \tag{1.2.2}$$

Because $u_k(\mathbf{r})$ is a periodic function, it can be written as a Fourier series,

$$u_k(\mathbf{r}) = \sum_{\mathbf{G}} c_{k,\mathbf{G}} e^{i\mathbf{G}\cdot\mathbf{r}}, \tag{1.2.3}$$

where $c_{k,\mathbf{G}}$ are complex plane wave expansion coefficients. The sum is over all reciprocal lattice vectors $\mathbf{G}$, defined through $\mathbf{G}\cdot\mathbf{R} = 2\pi m$, where m is an integer and $\mathbf{R}$ is a real space lattice vector. Every basis function $e^{i\mathbf{G}\cdot\mathbf{r}}$ represents

a plane-wave. Combining Eqs. 1.2.1 and 1.2.3, one obtains

$$\psi_k(\mathbf{r}) = \sum_{\mathbf{G}} c_{k,\mathbf{G}} e^{i(\mathbf{k}+\mathbf{G})\mathbf{r}}. \quad (1.2.4)$$

In principle, there are infinite number of **G**, but the expansion coefficients $c_{k,\mathbf{G}}$ decrease while $|\mathbf{G}|^2$ increases.

1.2.8 Pseudopotentials

It has been shown that when plane waves are applied to represent the electron wave function, the computation is still very demanding if one has to explicitly consider valence and core electrons. Large energy cut off for plane wave approximation is required for accurate electronic structure due to highly oscillating behavior of valence electrons and tightly bound core orbitals.[30] However, most of the physical properties of solids depend on the valence electrons while core electrons are non-sensitive to the environment. The pseudopotential approximation is introduced such that wave functions change smoothly near the nucleus, and therefore plane wave cut off energy is reduced.[31,32] Eventually nucleus and core electrons are considered as an ion, and pseudopotential is generated to have the same effect on the valence electrons.

1.2.9 Conclusion

First principal calculation has become a great success in materials science research. It provides the fundamental tool to investigate the ground-state

energy of the system without too much prior knowledge. The great agreement between calculation and experiment shows qualitative insights and capability of such approach. Various attempts to improve upon the calculations are still very active. The new algorithm has been introduced to shorten computational time and to reduce computational resources. With this effort the larger system is accessible that new phenomena can be realized through the sophisticated model. Bridging model with size scale from couple nanometers to hundred even thousand nanometers using DFT provides the useful information which can be extended to other computational method, or to explain experimental observation. As an exploratory tool for materials discovery, lots of successful stories can be told and there are more to be done in a nearly future.

Chapter 2
Strain Engineering

2.1 Strain Engineering of Piezoelectric Properties of Strontium Titanate Thin Films

In this chapter, a nonlinear thermodynamic model is employed to investigate the in-plane and out-of-plane piezoelectric properties of (001) strontium titanate ($SrTiO_3$, STO) epitaxial thin films on pseudo-cubic (001) substrates as a function of in-plane misfit strain. The appropriate mechanical boundary conditions, the electromechanical coupling between the polarization and the in-plane lattice mismatch, and the self-strains of the ferroelastic and ferroelectric phase transformations are taken into account. The piezoelectric behavior of epitaxial STO films is described in various strain-induced ferroelectric phase fields in a temperature range of $-50°C$ to $50°C$. These calculations show that by carefully tailoring in-plane misfit strains in both tensile and compressive ranges, piezoelectric coefficients that are of the order of prototypical lead zirconate titanate and other lead-based piezoceramics can be realized. These results indicate that strain engineered STO films may be employed in a variety of sensor and actuator applications as well as surface acoustic wave devices

and thin-film bulk acoustic resonators.

2.1.1 Introduction

Since the first observation of piezoelectricity in late 19th century in material systems such as sodium chlorate and quartz[33] as a phenomenon coupling mechanical and electrical properties, extensive research has been carried out in this field due to its potential applications such as in sensors and actuators,[34] transducers,[35] generators,[36] and emitters and receivers for sonar applications.[37] From the aspect of crystallo-chemical considerations, piezoelectricity is found in systems with loss of crystalline centro-symmetry.[38,39] In that regard, several different ceramic-based material systems have been shown to have relatively high piezoelectric coefficients. Among such piezoceramics are conventional perovskite materials with the prototypical ABO_3 chemical formula such as $PbTiO_3$,[40] $Pb(Zr_xTi_{1-x})O_3$ (PZT),[41] $BaTiO_3$ (BTO),[42] $(K_{0.5}Na_{0.5})NbO_3$ (KNN),[43] and $Ba_xSr_{1-x}TiO_3$ (BST)[44] where the centro-symmetrical arrangement is lost below the ferroelectric-paraelectric phase transformation temperature (T_C, Curie temperature). Although piezoelectricity is also observed in tungsten bronze type structured materials like $Sr_xBa_{1-x}Nb_2O_6$ (SBN)[45] and simple oxides and nitrides such as ZnO[46] and AlN,[?] the magnitude of the piezoelectric coefficient is typically one to two orders of magnitude smaller than PZT and its derivatives. A list of selected materials and their piezoelectric properties that are extracted from Refs.[40,43,45,47–66] is presented in Table I.

In radio frequency (RF), surface acoustic wave (SAW), and bulk acoustic wave (BAW) applications, current resonators are typically based on AlN[67] which has a very modest piezoelectric coefficient (d_{33}=5.15 pm/V) compared to PZT (Table I). Such devices benefit from the strong chemical stability, excellent mechanical properties, and low dielectric losses combined with low leakage currents of AlN.[67] However, AlN has relatively poor electromechanical coupling coefficients and lower dielectric constant compared to PZT. Furthermore, AlN has a wurtzite crystal structure (P63mc) and does not undergo a ferroelectric phase transformation. It is a linear dielectric and its deposition onto a suitable substrate is not as straightforward as the growth of an oxide film. Taking these limitations into account, in order to enhance device properties and introduce additional functionalities, a logical alternative is an environmentally friendly ferroelectric oxide with PZT-like piezoelectric behavior coupled with low loss tangent and leakage. Alternatives such as $BiFeO_3$ (BFO) have been considered for this purpose[68,69] but the dielectric losses and leakage in BFO-based systems can be prohibitively high.[70]

We note that there exists a vast amount of literature on lead-free electroceramics which are developed by varying the chemistry through doping in systems that have a morphotropic phase boundary. Panda provides an excellent review of the current state-of-the-art in Ref.[71] While significant efforts were devoted to the discovery of such piezoelectrics, the prototypical perovskite strontium titanate ($SrTiO_3$ or STO) has not received much attention

compared to materials with significantly more complex chemistries.[71,72] STO ($Pm\bar{3}m$ – Fig. 2.1.1) is an incipient ferroelectric with coupled instabilities.[73] Under no geometrical constraint, an anti-ferrodistortive (AFD) structural phase transition takes place at $-168^{\circ}C$ from a cubic to a tetragonal symmetry with space group I4/mcm, which is attributed to the rotation of TiO_6 octahedra about the pseudo-cube axes caused by the softening, or the instability, of the soft optical phonon mode.[74] The crystal structure of STO and the structural order parameters $q=q_i$ (i=1,2,3) that result in the ferroelastic phase transformation are shown in Fig. 2.1.1(a). In a stress-free and unconstrained system, pure STO crystals remain paraelectric down to absolute zero. However, electrical,[75] chemical,[76] and/or mechanical[77,78] manipulations result in the formation of ferroelectric phase(s).[79] Theoretically, the formation of different ferroelectric phases under different choices of electrical, thermal and mechanical boundary conditions has been studied using Monte Carlo simulations,[80] phase-field approaches,[81] molecular dynamics,[82] first-principles calculations,[83] and thermodynamic models.[84] For STO in particular, a thermodynamic analysis by combining theory of elasticity and the Landau theory of phase transformations was carried out by Pertsev *et al.*[85,86] in which it is shown that it is possible to stabilize a variety of different ferroelectric phases in epitaxial STO thin films that are monolithically unstable in bulk polycrystalline or single-crystal form. Indeed, for epitaxial (001) STO thin films at room temperature (RT=298K=25$^{\circ}C$) ferroelectricity is observed experimentally by carefully adjusting the equi-biaxial

in-plane misfit strain.[79] These findings provide the motivation for the current study wherein the piezoelectric properties of monodomain epitaxial (001) STO thin films are computed using a non-linear thermodynamic theory as a function of the in-plane misfit strain. We show that by tailoring the magnitude of the in-plane lattice mismatch, piezoelectric properties of the order of hundreds of pm/V can be achieved in STO films.

It should be noted that STO has a large bulk tunable permittivity and a relatively low dielectric loss and is, as such, a potential candidate for microelectronic applications such as oscillators, phase shifters in radio frequency and microwave tunable devices, tunable filters, and delay lines.[67,87] Furthermore, STO films can be fabricated on a variety of substrates via different methods including chemical solution deposition techniques (CSD),[78] metallo-organic chemical vapor deposition (MOCVD),[88] molecular beam epitaxy (MBE),[79,89] and pulsed laser deposition (PLD).[90] We have shown that a dielectric permittivity of 325 at 100 kHz with a tunability of ~28% at ~650 kV/cm and a loss of $\leq$ 2% can be obtained in STO films deposited using industry standard methods on commercial metallized Si substrates.[78] From the viewpoint of finding alternatives in the development of environmentally friendly electroceramics with piezoelectric coefficients that are comparable to PZT and PZT-based materials, the results of this study enable strain engineered STO as a viable candidate for applications such as sensors and actuators, surface acoustic wave devices, and thin-film bulk acoustic resonators.

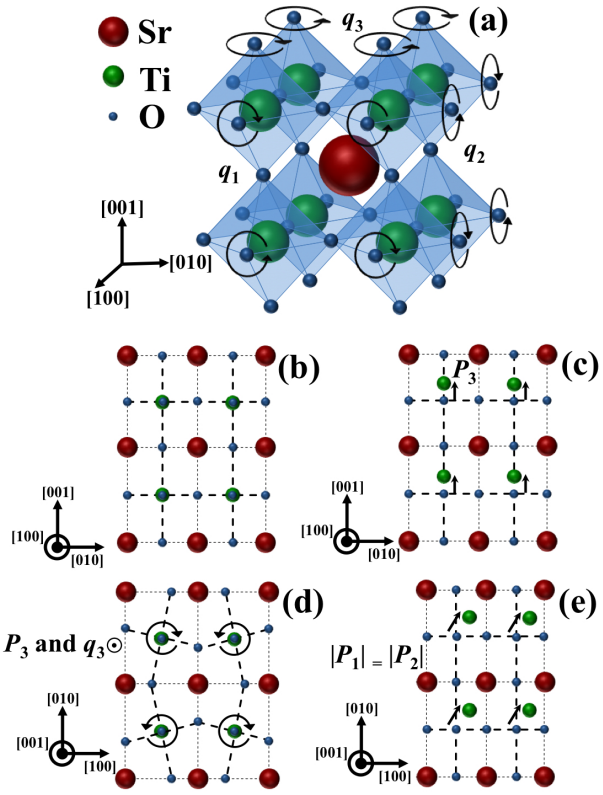

Figure 2.1.1: (a) The prototypical perovskite STO lattice (Pm $\bar{3}$ m). Also shown are the TiO_6 octahedra and the structural order parameters q = q*i* (*i* = 1,2,3) of the ferroelastic phase transformation at −168 °C; (b) 2-dimensional projection of high-temperature tetragonal (HT) phase in the [100] plane where P_1 =P_2 = P_3 =0 and q_1 = q_2 = q_3 = 0; (c) ferroelectric tetragonal FTI phase in the [100] plane where P_1 =P_2 = 0, P_3 =0, and q_1 = q_2 = q_3 = 0; (d) ferroelectric tetragonal FTII phase in the [001] plane where P_1 = P_2 = 0, P_3 = 0, and q_1 = q_2 = 0, q_3 = 0; and (e) ferroelectric orthorhombic (FOI) in the [100] plane where P_1 = P_2 =0, P_3 =0, and q_1 = q_2 = q_3 = 0

2.1.2 Theoretical Methodology

We consider here a (001) monodomain STO film on a thick (001) cubic substrate. Taking into account the equi-biaxial in-plane misfit strain um and

an applied electrical field **E**=E_i (i=1,2,3) the total free energy is given by[85,86]

$$\begin{aligned} G(P_i, q_i, u_m, E_i, T) = G_0 &+ \tilde{a}_1(P_1^2 + P_2^2) + \tilde{a}_3 P_3^2 + \tilde{a}_{11}(P_1^4 + P_2^4) + \tilde{a}_{33} P_3^4 + \tilde{a}_{12} P_1^2 P_2^2 \\ &+ \tilde{a_{13}}(P_1^2 + P_2^2) P_3^2 + \tilde{b_1}(q_1^2 + q_2^2) + \tilde{b_3} q_3^2 + \tilde{b_{11}}(q_1^4 + q_2^4) \\ &+ \tilde{b}_{33} q_3^4 + \tilde{b}_{12} q_1^2 q_2^2 + \tilde{b}_{13}(q_1^2 + q_2^2) q_3^2 - \tilde{t}_{11}(P_1^2 q_1^2 + P_2^2 q_2^2) \\ &- \tilde{t}_{33} P_3^2 q_3^2 - \tilde{t}_{12}(P_1^2 q_2^2 + P_2^2 q_1^2) - \tilde{t}_{13}(P_1^2 + P_2^2) q_3^2 \\ &- \tilde{t}_{31} P_3^2 (q_1^2 + q_2^2) - t_{44}(P_1 P_2 q_1 q_2) - \tilde{t}_{44}(P_1 P_3 q_1 q_3 + P_2 P_3 q_2 q_3) \\ &+ (c_{11} + c_{12} - 2c_{12}^2/c_{11}) u_m^2 - E_1 P_1 - E_2 P_2 - E_3 P_3 \end{aligned} \tag{2.1.1}$$

where G_0 is the free energy density of the paraelectric cubic phase, P=P_i are the components of the polarization vector, q=q_i are the structural order parameters describing the rotation of the TiO_6 octahedra, and c_{mn} are the elastic stiffnesses at constant P_i and q_i in the Voigt notation. The re-normalized coefficients $\tilde{a}_i$

and $\tilde{a}_{ij}$, $\tilde{b}_i$ and $\tilde{b}_{ij}$ and $\tilde{t}_{ij}$ entering Eq. 2.1.1 are given by:[83,84]

$$\tilde{a}_1 = a_1 - \Big(g_{11} + g_{12} - 2\frac{c_{12}}{c_{11}}g_{12}\Big)u_m, \quad \tilde{a}_3 = a_1 + 2\Big(\frac{c_{12}}{c_{11}}g_{11} - g_{12}\Big)u_m \tag{2.1.2}$$

$$\tilde{a}_{11} = a_{11} - \frac{g_{12}^2}{2c_{11}}, \quad \tilde{a}_{33} = a_{11} - \frac{g_{11}^2}{2c_{11}}, \tag{2.1.3}$$

$$\tilde{a}_{12} = a_{12} - \frac{g_{12}^2}{c_{11}}, \quad \tilde{a}_{13} = a_{12} - \frac{g_{11}g_{12}}{c_{11}} - \frac{g_{44}^2}{2c_{44}}, \tag{2.1.4}$$

$$\tilde{b}_1 = b_1 - \Big(\lambda_{11} + \lambda_{12} - 2\frac{c_{12}}{c_{11}}\lambda_{12}\Big)u_m \tag{2.1.5}$$

$$\tilde{b}_3 = b_1 - 2\Big(2\frac{c_{12}}{c_{11}}\lambda_{11} - \lambda_{12}\Big)u_m \tag{2.1.6}$$

$$\tilde{b}_{11} = b_{11} - \frac{\lambda_{12}^2}{2c_{11}}, \quad \tilde{b}_{33} = b_{11} - \frac{\lambda_{11}^2}{2c_{11}}, \tag{2.1.7}$$

$$\tilde{b}_{12} = b_{12} - \frac{\lambda_{12}^2}{c_{11}}, \quad \tilde{b}_{13} = b_{12} - \frac{\lambda_{11}\lambda_{12}}{c_{11}} - \frac{\lambda_{44}^2}{2c_{44}}, \tag{2.1.8}$$

$$\tilde{t}_{11} = t_{11} + \frac{g_{12}\lambda_{12}}{c_{11}} \quad \tilde{t}_{33} = t_{11} + \frac{g_{11}\lambda_{11}}{c_{11}}, \tag{2.1.9}$$

$$\tilde{t}_{12} = t_{12} + \frac{g_{12}\lambda_{12}}{c_{11}} \quad \tilde{t}_{13} = t_{12} + \frac{g_{12}\lambda_{11}}{c_{11}}, \tag{2.1.10}$$

$$\tilde{t}_{31} = t_{12} + \frac{g_{11}\lambda_{12}}{c_{11}} \quad \tilde{t}_{44} = t_{44} + \frac{g_{44}\lambda_{44}}{c_{44}}, \tag{2.1.11}$$

where a_i and a_{ij}, b_i and b_{ij}, and t_{ij} are the stress-free, monodomain dielectric stiffness coefficients, structural order parameter susceptibility coefficients, and coupling coefficients between the polarization Pi and the structural order parameter q_i, respectively. In Voigt notation, g_{ij} are the electrostrictive constants and λ_{ij} are the coupling coefficients between the strain and q_i.

The piezoelectric coefficient can be determined from the free energy func-

tional given in Eq.2.1.1 using the appropriate Maxwell relations

$$dS = \left(\frac{\partial S}{\partial T}\right)_{x,E} dT + \left(\frac{\partial S}{\partial x_m}\right)_{T,E} dx_m + \left(\frac{\partial S}{\partial E_i}\right)_{T,x} dE_i \tag{2.1.12}$$

$$dX_m = \left(\frac{\partial X_m}{\partial T}\right)_{x,E} dT + \left(\frac{\partial X_m}{\partial x_n}\right)_{T,E} dx_n + \left(\frac{\partial X_m}{\partial E_k}\right)_{T,x} dE_k \tag{2.1.13}$$

$$dD_i = \left(\frac{\partial D_i}{\partial T}\right)_{x,E} dT + \left(\frac{\partial D_i}{\partial x_m}\right)_{T,E} dx_m + \left(\frac{\partial D_i}{\partial E_j}\right)_{T,x} dE_j \tag{2.1.14}$$

where S is the entropy, X is the stress tensor, x is the total strain tensor, D_i is the electric displacement field with temperature (T), applied electric field (E_i), and strain (x) as independent variables. Eqs. 2.1.13 and 2.1.14 for an isothermal process can be rewritten in an integrated form as:

$$X_m = c_{mn^E} x_n + e^u_{km} E_k \tag{2.1.15}$$

$$D_i = e^E_{im} x_m + \epsilon^u_{ij} E_j \tag{2.1.16}$$

$$\tag{2.1.17}$$

with

$$c^E_{mn} = (\frac{\partial X_m}{\partial x_n})_E \tag{2.1.18}$$

$$e^u_{km} = (\frac{\partial X_m}{\partial E_k})_x \tag{2.1.19}$$

$$e^E_{im} = (\frac{\partial D_i}{\partial x_m})_E \tag{2.1.20}$$

$$\tag{2.1.21}$$

and

$$\epsilon_{ij}^{u} = (\frac{\partial D_i}{\partial E_j})_x \tag{2.1.22}$$

The coefficients of piezoelectric tensor are then defined as

$$d_{in} = \epsilon_{ij}^{u} h_{jm} (c_{nm}^{E})^{-l} \tag{2.1.23}$$

where ϵ_{ij}^{u} is the dielectric permittivity at constant strain, h_{jm} is the voltage coefficient, and c_{nm}^{E} are elastic stiffnesses at constant electric field.

2.1.3 Results and Discussion

Using the appropriate property coefficients in Eqs. 2.1.1 and 2.1.2−2.1.11 which are given in Ref.,[85] and evaluating the equations of state $\partial G/\partial P_i = 0$ and $\partial G/\partial q_i = 0$ at E_i=0, the Pertsev misfit strain-temperature phase diagram in the temperature range of $-50°C$ to $50°C$ and misfit strain range of −2% to 2% can be reproduced as shown in Fig. 2.1.2. The phases that appear in Fig. 2.1.2 are defined as:

$$HT : P_1 = P_2 = P_3 = 0,\ q_1 = q_2 = q_3 = 0, \tag{2.1.1}$$

$$FTI : P_1 = P_2 = 0, P_3 \neq 0,\ q_1 = q_2 = q_3 = 0, \tag{2.1.2}$$

$$FOI : P_1 = P_2 \neq 0, P_3 = 0,\ q_1 = q_2 = q_3 = 0, \tag{2.1.3}$$

$$FTII : P_1 = P_2 = 0, P_3 \neq 0,\ q_1 = q_2 = 0, q_3 \neq 0 \tag{2.1.4}$$

and are schematically illustrated in Figs. 2.1.1(b-e).

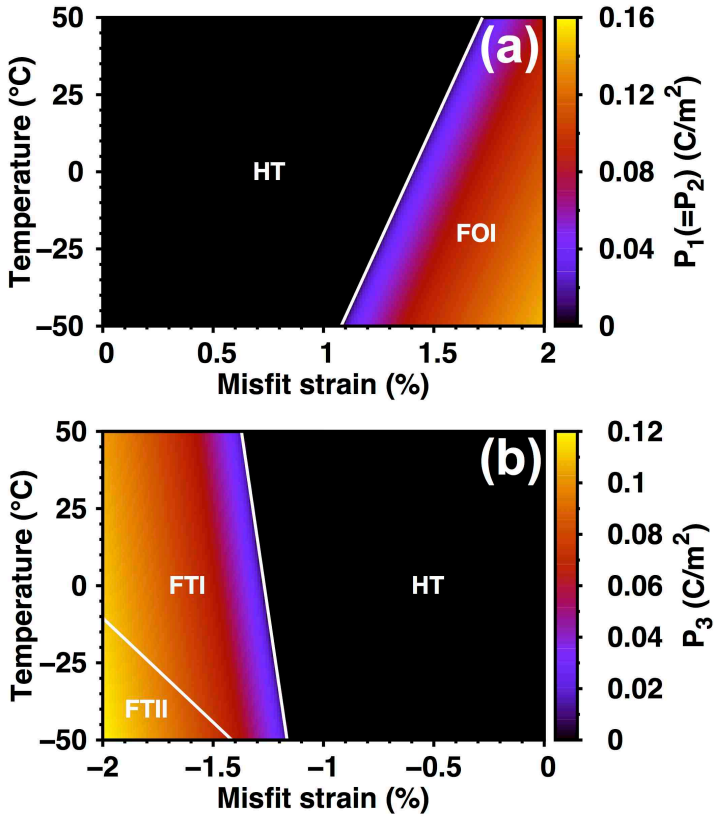

Figure 2.1.2: Phase diagram of monodomain epitaxial (001) STO films under (a) tensile and (b) compressive misfit strains on a thick (001) pseudo-cubic substrate in the temperature range from −50 to 50 °C. The map also shows variations in the out-of-plane and in-plane polarizations (P_3 and P_1) in the ferroelectric phase fields

Depending on u_m and T, three ferroelectric phases (FTI, FTII, and FOI) can be thermodynamically favorable over the HT phase. HT is tetragonally distorted along the [001] direction (out-of-plane) but is paraelectric like its parent cubic ($Pm\bar{3}m$) phase. As it can be seen in these phase diagrams, FTI and FTII phases can be expected in the case of in-plane compressive misfit strains while FOI phase will be thermodynamically stable for in-plane tensile strains.

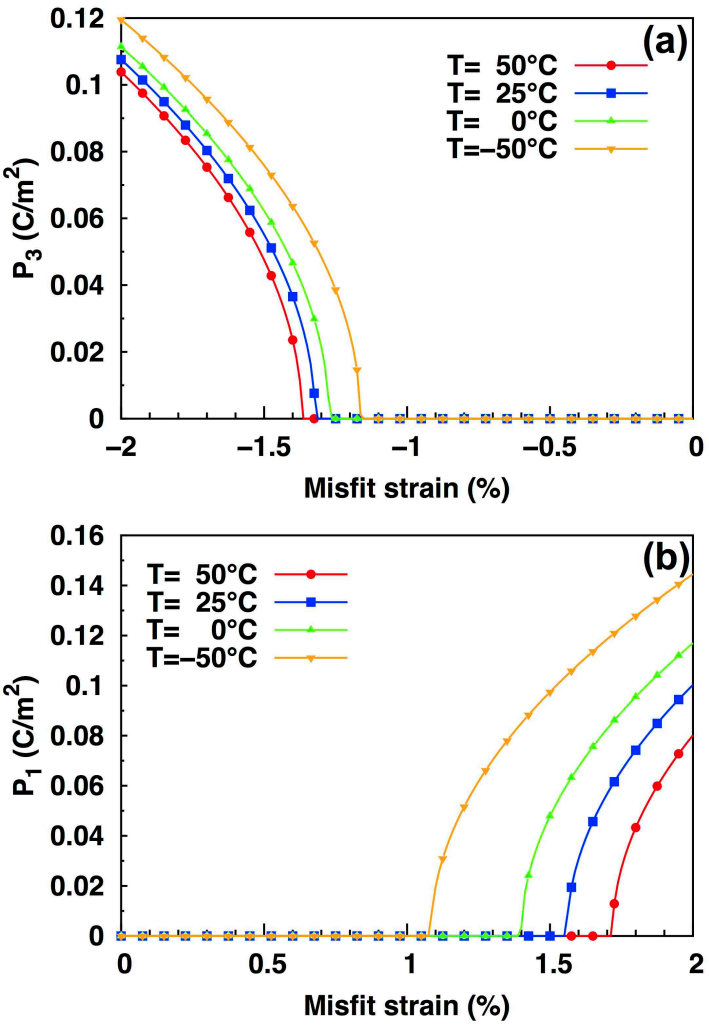

Figure 2.1.3: Variation of the (a) out-of-plane polarization (P_3) and (b) in- plane polarization (P_1) as a function of misfit strain at selected temperatures

Figs. 2.1.2a and 2.1.2b also display the variation of the in-plane and out-of-plane polarizations (P_1=P_2 and P_3, respectively) as a function of temperature and misfit strain. For low lattice mismatches, the paraelectric HT phase remains stable. The range of the stability of the HT phase decreases with decreasing temperature. At RT=25°*C*, HT has the lowest total free energy over a misfit strain

range corresponding to $-1.32 < u_m < 1.55$. For higher magnitudes of in-plane compressive and tensile misfit strains, ferroelectric phases FTI, FTII, and FOI become more stable. In these regions, however, there is a gradual variation in the magnitude of the components of the polarization as a function of the misfit strain at a given temperature. The misfit strain and temperature dependence of the phase transformations shown in Fig. 2.1.2 can be better understood by tracing the polarization components at a given temperature. In Fig. 2.1.3, we plot P_3 and P_1=P_2 as a function of misfit strain at four different temperatures. On the compressive misfit strain side, there is a HT (P_1=P_2=P_3=0) to FTI (P_1=P_2=0, P_3 ≠0) transition for um=−1.16%, −1.27%, −1.32%, and −1.37% at T=$-50°C$, $0°C$, $25°C$, and $50°C$, respectively. This behavior is similar to the emergence of a ferroelectric phase below T_C and is accompanied by lambda-type instability in the second-order property coefficients. Experimental data presented by Warusawithana *et al.*[89] confirms that large internal compressive strains in STO films on silicon (−1.7%) result in ferroelectricity. On the other hand, for sufficiently large tensile misfit strains, the paraelectric HT phase is expected to transform to the ferroelectric FOI phase (P_1=P_2≠0, P_3=0) for um=1.07%, 1.40%, 1.55%, and 1.72% at T=$-50°C$, $0°C$, $25°C$, and $50°C$, respectively. Essentially, large tensile misfit strains force the emergence of in-plane polarization components.

Since in-plane compressive strains promote out-of-plane polarization (shown in Fig. 2.1.2a), FTI (with out-of-plane spontaneous polarization along the [001] direction) and FTII phases are stable for compressive misfit strains below cer-

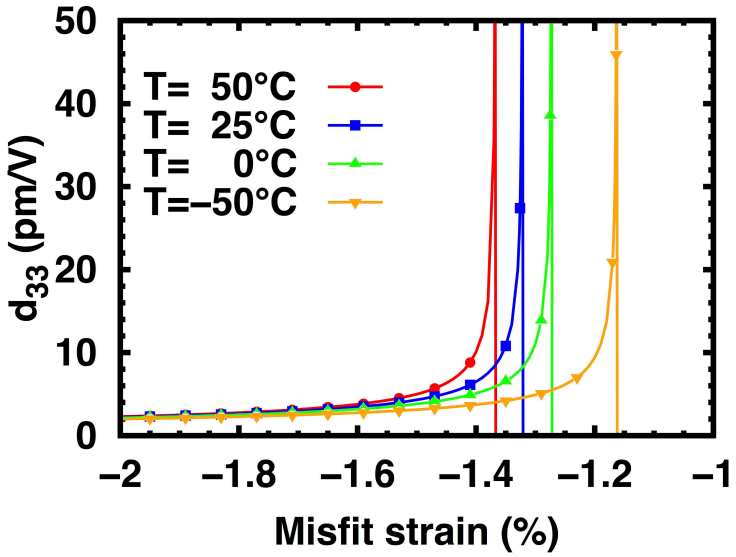

Figure 2.1.4: Piezoelectric response d_{33} versus misfit strain in the compressive range for different temperatures

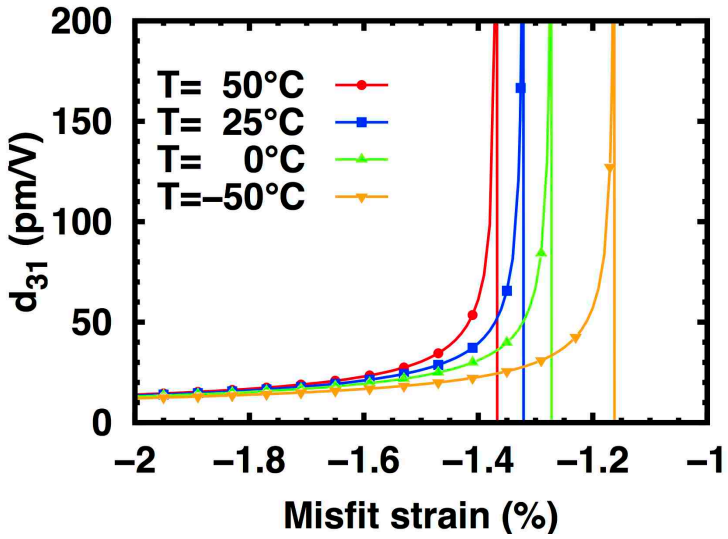

Figure 2.1.5: Piezoelectric response d_{31} versus misfit strain in the compressive range for different temperatures

tain temperatures. The difference between FTI and FTII is that for FTII one has to consider the coupling between the ferroelectric and ferroelastic order parameters for describing the displacements of the Ti atoms and the rotation of the TiO_6 octahedra. The FTII phase region is shown in the lower left corner of Fig. 2.1.2b. At T=$-50°C$, the FTI to FTII inter-ferroelectric transition should be expected at um=-1.41%. The out-of-plane polarization shows only a small change in slope with respect to T or u_m that is accompanied by comparatively small but discontinuous change in $\partial P_3/\partial T$ introduces a change in the magnitude of polarization along the [001] direction and $\partial P_3/\partial u_m$ (not shown). The strain dependence of the out-of plane (d_{33}) and the in-plane (d_{31}) piezoelectric coefficients are determined via Eqs. 2.1.12 $-$ 2.1.23 as a function of the misfit strain and temperature. Here, we consider a metal/insulator/metal heterostructure (MIM) for which the (001) epitaxial STO film is sandwiched between metallic electrodes. In this this configuration, Ei=[0,0,E3]. By assuming that the bottom electrode is grown pseudomorphically onto the substrate, we ensure that both the sign and magnitude of um are entirely controlled by the mismatch between the film and the substrate. The results plotting the misfit strain dependence of d_{33} and d_{31} at selected temperatures are given in Figs. 2.1.4 and 2.1.5, respectively. Firstly, these figures confirm that the HT phase is not piezoelectric because of its centro-symmetrical crystal structure (Fig.. 2.1.1b). Secondly, and more importantly, at a given temperature as the HT to FTI or HT to FOI phase transformations are approached with increasing compres-

sive or tensile misfit strain, there is a significant increase in the piezoelectric coefficients. This is analogous to instabilities in the second-order property coefficients near a second order phase transformation. These results show that if the misfit strain can be controlled such that it is near the um-induced phase transformation from the HT to the FTI or the FOI phases, piezoelectric properties similar to PZT can be obtained. Away from the critical misfit strains corresponding to phase transitions from the HT phase to a ferroelectric phase, the piezoelectric response decreases dramatically. For example, at RT for u_m=−1.4%, d_{33}=6.1 pm/V and d_{31}=40 pm/V in the FTI phase fields. While these values are much smaller than what is expected near the critical misfit strains discussed above, they are comparable to those of non-ferroelectric materials such as AlN and ZnO. The lattice mismatch between STO and commonly used materials as substrates such as Si, sapphire ($\alpha-Al_2O_3$), $DyScO_3$, $LaAlO_3$, and MgO can introduce sufficiently large in-plain strains (um=1.7%, −10.8%, 1.18%, −3%, 7.5%, respectively) and may indeed stabilize ferroelectric phases at RT. It should also be noted that high lattice mismatches between STO and the substrate potentially could facilitate the process of strain relaxation that would hinder the accessibility of ferroelectric phases at RT. In practice, there are several key factors that have impact on the interaction between the film and the substrate. It is shown that the stresses are almost completely relaxed with increasing the film thickness through the formation of misfit strain dislocations at the STO/substrate interface. The higher the lattice mismatch between

STO and the substrate, the thinner the critical thickness for relaxation through the generation of interfacial dislocations.[91] Deposition/processing/annealing temperatures also play an important role on the relaxation procedure. The straightforward application of the Matthews-Blakeslee criteria indicates that the critical thickness of misfit dislocation formation is relatively larger for lower processing temperatures due to the smaller thermal strain.[92] Taking all these factors into account, experimental studies still suggest that even for lattice mismatches as large as 7.5% in STO/MgO and -3% for STO/$LaAlO_3$, which are well above the critical mismatch, although the thickness at which the relaxation starts is very small, depending on the mechanism as well as the kinetics of the misfit dislocation process, complete relaxation does not occur until the film thickness reaches $50-250$ nm and bellow this thickness the film remains unrelaxed.[93]

2.1.4 Conclusion

A non-linear thermodynamic model based on Landau theory of phase transformations was employed to investigate the piezoelectric behavior of epitaxial (001) STO films by considering the electromechanical coupling between the polarizations and the in-plane lattice mismatch. Our results suggest that manipulations of the STO system through structurally imposed boundary conditions introduces piezoelectric coefficients that are of the order of prototypical lead zirconate titanate and other lead-based piezoceramics and provide the

possibility of fine-tuning polarization. Strain engineered STO films then can be utilized in industries such as sensor and actuator applications and surface acoustic wave devices and acoustic resonators.

2.2 Strain Engineered Barium Strontium Titanate for Tunable Thin Film Resonators

In previous section, STO films were investigated for sensor, actuator, acoustic wave devices, and acoustic resonators application. Here, barium strontium titanate ($Ba_xSr_{1-x}TiO_3$, BST), a ferroelectric material possess the features of high dielectric constant, low cost, and phase transition temperature around 20 °C, has been considered as a good candidate for tunable microwave devices. In order to enhance its tunability, not only by in-plane lattice mis-match, the composition of BST also provide extra degree of freedom for the desirable properties. With the consideration of electromechanical coupling between the polarization and the in-plane lattice mismatch, a nonlinear thermodynamic model is employed that takes into account the appropriate mechanical boundary conditions. The emergence of piezoelectricity in ferroelectric (FE) and paraelectric (PE) regions is observed and under the application of electric field, d_{33} values as large as 1500 pm/V in the FE-phase is obtained. By adjusting the composition and in-plane misfit, an electrically tunable piezoelectric response can be achieved, even in its paraelectric state. The computational results show that in order to develop electrically tunable and switchable surface and bulk acoustic wave resonators, one might consider BST films as a potential candidate with strain engineering technique.[94]

2.2.1 Introduction

The diversity of commercialized application, which consist of surface and bulk acoustic wave, SAW and BAW respectively, provokes the studies of interest both scientifically and practically. Among several electronic devices, such as remote controls, microprocessor clocks, mobile component, piezoelectric thin films sandwiched by two metal layers, operate within radio frequency (RF) range is commonly used for telecommunication system. The geometry architecture, as long as the selected materials, play an important role on determining the resonant frequency in SAW and BAW resonators. Compound semiconductors such as GaAs or micro-electromechanical systems (MEMS) are then used as RF switches to select the appropriate fixed frequency filter. AlN exhibits strong chemical stability, excellent mechanical properties, and low dielectric losses combined with low leakage currents[95,96] and can be manufactured using recent developments in micro-machining techniques.[97] On the other hand, it is a linear dielectric with a wurtzite crystal structure ($P6_3mc$) and has a weak piezoelectric response ($d_{33} \sim 5$ pm/V)[2] compared to ferroelectrics (FE) such as (Pb,Zr)TiO_3 (PZT) and its derivatives (300 pm/V).[98,99]

Since the piezoelectric response of AlN is not electrically tunable, present AlN-based SAW and BAW resonators are fixed frequency devices.[100] Despite efforts to achieve electrical tuning in AlN-based resonators through implementation of sound guiding substrates and varying device dimensions, tuna- bility in these systems is less than 1%.[101,102] Furthermore, current SAW and BAW devices must employ semiconductor or MEMS switches for frequency selection.

As such, there exists a tremendous potential for the development of tunable and switchable thin film acoustic resonators. This would reduce the total parts count for RF products and would thus provide opportunities to manufacture smaller and cheaper devices. Piezoelectric tunability would enable frequency agile opera- tion, eliminate filter banks as a costly and lossy source, and provide the possibility to get rid of the need for frequency trimming. For this purpose, FE materials have attracted atten- tion as potential alternatives for AlN.[?] Because the electrome- chanical coupling depends on the spontaneous polarization, resonance in the FE state exhibits hysteresis.[97,103] However, since an appropriate electric field can distort central symmetry, emergence of piezoelectricity is possible in the paraelectric phase with the application of an external field. There are incipient FE or FE perovskites such as strontium titanate ($SrTiO_3$, STO)[97,104,105] and barium strontium titanate [$Ba_xSr_{1-x}TiO_3$, BST x/(1-x)][101,102,106–113] for which voltage induced electrostrictive resonance has been demonstrated in free-standing film or solidly mounted resonator (SMR)[101,106] device geometries.

In bulk, unconstrained BST, the phase transition temperature TC can be varied by adjusting the relative amounts of Ba and Sr. T_C for pure barium titanate ($BaTiO_3$, BTO) is 120 °C, but by alloying systematically with STO, T_C can be lowered. For example, for BST 70/30 and 60/40, the cubic paraelectric to tetragonal FE transformations occur at ~34 °C and ~5 °C, respectively.[113] The ability to adjust T_C by controlling the composition is one of the most promising

aspects of using BST in different types of resonators since piezoelectric response and its electric field tunability can be maximized near T_C. Misfit strain-temperature phase diagrams that were developed for monodomain epitaxial BST films[113,114] show that it is possible to induce FE phases with orthorhombic and rhombohedral symmetry that are not observed in bulk form.[115] In Fig. 2.2.1, we depict the prototypical perovskite BST crystal structure ($Pm3m$) in the bulk PE state and the FE states that can be induced through in-plane equi-biaxial misfit strains. The phases that appear in Fig. 2.2.2 are defined through the spontaneous polarization vector P_i (i = 1, 2, 3) such that: PE phase (P4mm) with $P_1 = P_2 = P_3 = 0$, c-phase ($I\bar{4}3$ m) with $P_1 = P_2 \neq 0, P_3 = 0$, aa−phase (Amm2) with $P_1 = P_2 \neq 0, P_3 = 0$, and r-phase (R3m) with $P_1 = P_2 \neq 0, P_3 \neq 0$. In this

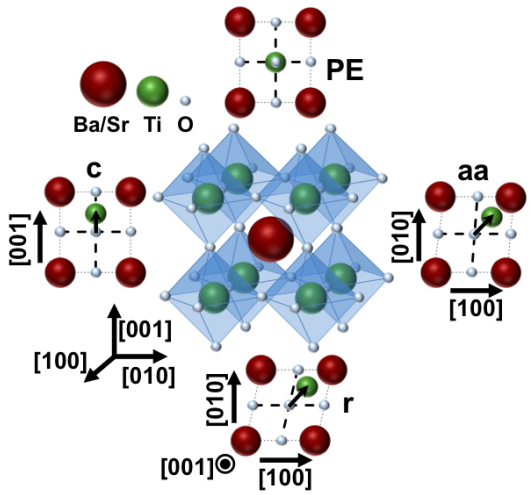

Figure 2.2.1: At the center is the prototypical perovskite BST crystal structure where Ba/Sr atoms are surrounded by eight TiO_6 octahedra. Also shown are the possible strain induced phases. Polarization components in the tetragonal PE phase are $P_1 = P_2 = P_3 = 0$. The c-phase is tetragonal with $P_1 = P_2 = 0$, $P_3 \neq 0$.The aa-phase has an orthorhombic structure where $P_1 = P_2 \neq 0$ and $P_3 = 0$ and the r-phase is rhombohedral with $P_1 = P_2 \neq 0$ and $P_3 \neq 0$.

study, we provide a theoretical analysis of piezo- electric response of epitaxial (001) BST films using a nonlinear thermodynamic model taking into account the appropriate electromechanical boundary conditions. We show that strain engineering is a powerful tool that could assist in the development of a new generation of acoustic resonators with extremely large piezoelectric coefficients which are also electrically tunable and/or switchable. Our results indicate that for certain BST compositions and small misfit strains ($-0.07 < u_m < 0.08\%$ and $-0.12 < u_m < 0.13\%$ for BST 80/20 and 90/10, respectively), the FE r-phase can be stabilized at room temperature (RT = 25 °C). The spontaneous polarization in this state can adapt itself to external stimuli through appropriate rotations and thus has very large piezo- electric response. BST films with lower Ba concentrations such as BST 60/40 remain paraelectric at RT for small misfit strains ($-0.04 < u_m < 0.04$). We demonstrate here that in this range, piezoelectric coefficients as high as ~ 300 pm/V can be realized with the application of external electric fields (400 kV/m). This behavior could be useful in certain telecommunication applications for which a paraelectric state may be preferred in order to avoid hysteresis losses associated with nucleation and growth of electrical domains.[107,116] The piezoelectric tunabilities of BST 60/40 in the FE c-phase region are 19% and 29% at 200 and 400 kV/m. These results suggest that tailoring the strain state in FE oxides could provide outstanding piezoelectric response compared to current simple oxide and nitride piezoelectric ceramics. **2.2.2 Methodology**

We employ here a Landau−Devonshire approach to compute the piezoelectric properties of heteroepitaxial BST films in different phase fields.

$$\begin{aligned}\widetilde{G} = {} & a_1^*(P_1^2 + P_2^2) + a_3^* P_3^2 + a_{11}^*(P_1^4 + P_2^4) + a_{33}^* P_3^4 \\ & + a_{13}^*(P_1^2 P_3^2 + P_2^2 P_3^2) + a_{12}^* P_1^2 P_2^2 + a_{111}^*(P_1^6 + P_2^6 + P_3^6) \\ & + a_{112}^*[P_1^4(P_2^2 + P_3^2) + P_3^4(P_1^2 + P_2^2) + P_2^4(P_1^2 + P_3^2)] \\ & + a_{123} P_1^2 P_2^2 P_3^2 + \frac{u_m^2}{S_{11} + S_{22}} - E_3 P_3\end{aligned} \tag{2.2.1}$$

where the renormalized coefficients is defined as

$$\begin{aligned}a_1^* &= a_1 - u_m \frac{Q_{11} + Q_{22}}{S_{11} + S_{22}}, \\ a_3^* &= a_1 - u_m \frac{2Q_{11}}{S_{11} + S_{22}}, \\ a_{11}^* &= a_{11} + \frac{1}{2(S_{11}^2 - S_{12}^2)}[(Q_{11}^2 + Q_{12}^2)S_{11} - 2Q_{11}Q_{12}S_{12}], \\ a_{33}^* &= a_{11} + \frac{Q_{12}^2}{S_{11} + S_{22}}, \\ a_{12}^* &= a_{12} - \frac{1}{(S_{11}^2 - S_{12}^2)}[(Q_{11}^2 + Q_{12}^2)S_{12} - 2Q_{11}Q_{12}S_{11}] + \frac{Q_{44}^2}{2S_{44}},\end{aligned}$$

and

$$a_{13}^* = a_{12} + \frac{Q_{12}(Q_{11} + Q_{12})}{S_{11} + S_{22}}, \tag{2.2.2}$$

where P_i represents the polarization component, $a_1=(T-T_0)/2\epsilon_0 C$ is the dielectric stiffness, T_0 is Curie-Weiss temperature, C is Curie-Weiss constant of a bulk ferroelectric, and ϵ_0 is the permittivity of free space, a_{ij} and a_{ijk} are higher

order stiffness coefficients, Q_{ij} are the electrostrictive coefficients, and S_{ij} are the elastic compliances of the film in Voigt notation.

A (001) monodomain epitaxial BST film on a thick (001) cubic substrate is considered. Taking into account the equi-biaxial in-plane polarization-free misfit strain $u_m = (a_S - a_F)/a_S$, where a_S and a_F are the lattice parameters of the substrate and the (pseudo-cubic) film, respectively, and an applied electrical field E_3//[001] perpendicular to the film-substrate interface, the (excess) free energy density of the film can be expressed as[113]

u_m-T phase diagrams are obtained by evaluating the equations of state $\partial \Delta G/\partial P_i = 0$ for $E_3 = 0$. The property coefficients used in the calculations are compiled from the literature.[113] In Fig. 2.2.2, we plot the stability regions of the FE and paraelectric phases for four compositions of BST (60/40, 70/30, 80/20, and 90/10) in temperature and misfit ranges of $-50 < T < 150$°C and $0.5 < u_m < 0.5\%$. Also shown in Fig. 2.2.2 is the total spontaneous polarization ($P = P_S = \sqrt{2P_{S,1}^2 + P_{S,3}^2}$) in each phase region. Regardless of the BST composition, the phase diagrams indicate that depending on T, there are two different sequences of phase transformations with increasing um from in-plane compressive to in-plane tensile misfits. At relatively higher temperatures, the c-phase which is more stable for in-plane compressive misfit strains transforms to the PE phase with increasing um at a critical misfit strain u m . At T = 100 °C, for BST 60/40, 70/30, 80/20, and 90/10, u_m is −0.22%, −0.16%, −0.09%, and −0.01%, respectively. With increasing in-plane tensile strains, the aa-phase becomes

more stable (u_m > 0.20% for BST 60/40 at T = 100 °C). Significant shifts in T_C and stabilization of metastable phases have been confirmed experimentally in similar epitaxial systems.[117,118] The c−PE and PE−aa transitions are of second-order due to the positive sign of the coefficients a_{11}^* , a_{12}^*, a_{13}^*, and a_{33}^*. This can also be verified by inspecting the variations in the polarization components in this field region. In Fig. 2.2.3(a), we plot as an example the change of the out-of-plane and in-plane spontaneous polarization of BST 60/40 at RT. Fig. 2.2.3(a) indicates that there are no jumps in P_3 and $P_1 = P_2$ at the critical misfit strains of −0.04% and 0.04% corresponding to the c−PE and PE−aa phase boundaries. Without applying electric field, P_3 vanishes at the c−PE boundary while for $E_3 > 0$ the material is polarized in the [001] direction. In the case of in-plane polarization, however, application of electric field does not alter the material behavior since the out-of-plane electric field does not affect planar polarization. At relatively lower temperatures for the four compositions analyzed in this study, a c−r−aa phase transition sequence becomes possible. Both the c−r and r−aa phase transformations are of second order and this is confirmed in Fig. 2.2.4(a) where we plot the polarization components variation versus misfit strain for BST 80/20 at RT. We note that the stability region of the r-phase becomes narrower with decreasing Sr content. For BST 70/30 and BST 90/10, the phase fields of the r-phase are within $-0.018 < u_m < 0.02\%$ and $-0.112 < u_m < 0.129\%$.

The out−of−plane piezoelectric coefficients (d_{33}) for the four phases can be

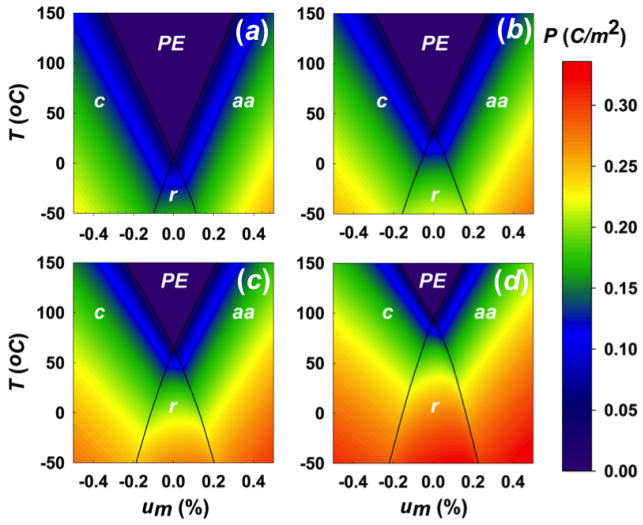

Figure 2.2.2: Phase diagrams of various compositions [60/40, 70/30, 80/20, and 90/10 from (a) to (d), respectively] of monodomain epitaxial (001) BST films under compressive and tensile misfit strains on a thick (001) pseudo-cubic substrate in the temperature range of 50 °C – 150 °C and variations of total polarization in the ferroelectric phase fields.

determined via

$$d_{33} = \begin{cases} \left(2\epsilon_0\eta_{33}Q_{11}P_3 & \text{PE} \\ 2\epsilon_0\eta_{33}Q_{11}P_3 & \text{c-phase} \\ 2\epsilon_0(\eta_{33}Q_{11} + \eta_{23}Q_{12})P_3 & \text{r-phase} \\ 2\epsilon_0(\eta_{11}Q_{11} + 2\eta_{12}Q_{12})P_3 & \text{aa-phase} \end{cases} \tag{2.2.3}$$

where $\eta_{ij} = A_{ij}/\Delta$ are dielectric susceptibility coefficients, and A_{ij} and Δ are the cofactor and determinant of relative dielectric stiffness tensor.[119]

Fig. 2.2.3(b) shows the variation in d_{33} of (001) BST 60/40 as a function of u_m

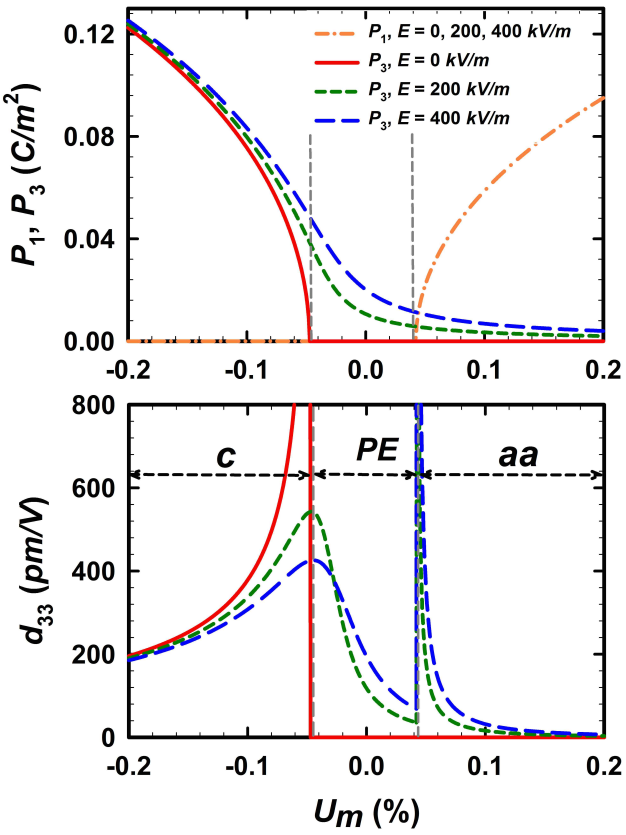

Figure 2.2.3: (a)Variation of the in-plane and out-of-plane spontaneous polarization components as a function of misfit strain and (b) RT out-of-plane piezoelectric response (d_{33}) of (001) BST (60/40) for different electric fields. d_{33} in the PE region is zero for $E_3 = 0$. For $E_3 > 0$, there is a piezoelectric response in the PE region for misfit strains close to the c-PE transition.

at RT for $E_3 = 0,\ 200,$ and 400 kV/m. This particular composition is chosen as an illustration of piezoelectric properties in the c−PE−aa phase fields at RT. In both PE and aa−regions, there is no piezoelectric response for $E_3 = 0$. However, for $E_3 > 0$, excellent piezoelectric properties can be obtained. For instance, for $u_m = 0.02\%$, $E_3 =$ 200and 400 kV/m produce piezoelectric coefficients as high as ~250 and ~300 pm/V, respectively. Here, piezoelectricity emanates only due to the fact that the central symmetry of the crystal is broken with

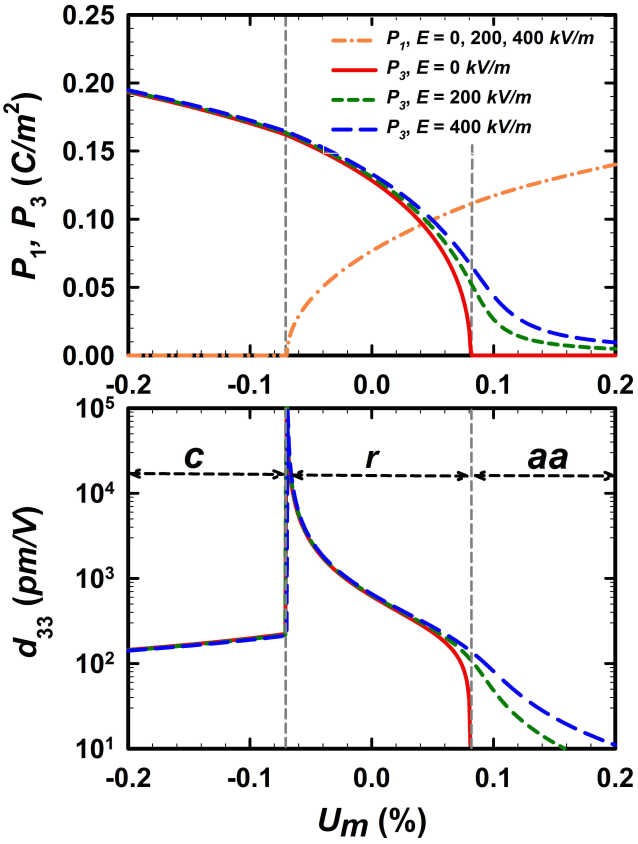

Figure 2.2.4: (a)Variation of the in-plane and out-of-plane spontaneous polarization components as a function of misfit strain and (b) RT out-of-plane piezoelectric response (d_{33}) of (001) BST (80/20) for different electric fields. d_{33} in the PE region is zero for $E_3 = 0$. For $E_3 > 0$, there is a piezoelectric response in the PE region for misfit strains close to the c-PE transition.

the application of an out-of-plane electric field. This is significant since it means that high values of d_{33} can be induced in the material system without hysteretic behavior−a fundamental characteristic of a FE material. To describe the piezoelectric behavior in c-r-aa phase fields, we chose (001) BST 80/20 at RT. Fig. 2.2.4(b) presents d_{33} for different electric field values. In the r-region, for misfit strains near the c−r phase transition, very high magnitudes of d_{33} values are predicted (e.g., d_{33} = 1500 pm/V for u_m = 0.05%). The large piezoelectric

properties in this region can be attributed to the ease by which the spontaneous polarization vector in the r-phase can adapt itself to external stimuli. The transition from the c-phase to the r-phase and then to the aa-phase occurs via a rotation of the spontaneous polarization from the [001] axis towards [110] direction. Because it is plotted in a log scale, in Fig. 2.2.4(b) the tunability of the piezoelectric coefficient in the r-region is not clearly displayed. For BST 80/20 and u_m = 0.06%, the piezoelectric coefficient varies from 179 pm/V to 223 pm/V with a change in the applied field from 0 kV/m to 400 kV/m. In the aa-phase region, however, out-of-plane piezoelectric response can only be obtained with the application of E3. While with zero electric field, piezoelectricity diminishes right before the r-aa transition. For E_3 = 200 and 400 kV/m, respectively, piezoelectric coefficients of 23 and 45 pm/V are achievable for u_m = 0.12%.

2.2.3 Discussions

It should also be noted that high lattice mismatches between BST and the substrate potentially could facilitate the process of strain relaxation that would hinder the accessibility of ferroelectric phases predicted by our calculations. In practice, there are several key factors that have impact on the interaction between the film and the substrate. It is shown that the stresses are almost completely relaxed with increasing film thickness through the formation of misfit strain dislocations at the film/substrate interface.[120] The higher the lattice mismatch between the film and the substrate, the smaller the crit-

ical thickness for relaxation through the generation of interfacial dislocations [Matthews−Blakeslee (MB) criteria].[121] The straightforward application of the MB criteria indicates that the critical thickness of misfit dislocation formation is relatively larger for lower processing temperatures due to the smaller thermal strain. Based on mechanisms by which interfacial dislocations are generated and the kinetics of the processes, experimental studies suggest that even for theoretical lattice mismatches larger than 7% for which the MB critical film thickness is typically of the range of 1−2 nm, complete relaxation does not occur until the film thickness reaches several hundred nanometers.[122] Therefore, depending on the deposition/processing/annealing temperatures and by the selection of substrate material, and film thickness, the level and sign of the misfit strain can be adjusted as to obtain optimum piezoelectric response.[113]

2.2.4 Conclusion

The epitaxial strains can be used to obtain very high piezoelectric properties in a lead-free soft FE material, in this case, barium strontium titanate (BST). In order to develop the electronic component, which is low voltage control or frequency tunable radio frequency resonators, the strain engineering on BST thin films is demonstrated being a promising candidate. It has been well-established in experimental point of view that composition and substrate selection are a tuning parameter and could result in desired piezoelectric response, both in paraelectric and FE phases. Moreover, electrically biased paraelectric

BST exhibits outstanding piezoelectric behavior that provides the opportunity to deliver hysteresis free behavior. This work provides the theoretical evidence that by carefully designing the combination of proper materials on suitable substrate with electrical field stimuli, the electrically tunable piezoelectric response can be obtained, and this would be beneficial in telecommunication technology to be established in tunable device configurations. The resulting components could reduce cost and improve performance for RF systems in a wide range of communications, radar, and wireless data applications.

Chapter 3

Ferroelectric Bilayers and Multilayers

In this chapter, a complete theoretical treatment of ferroelectric bilayers in the continuum limit using Maxwell's and Poisson's relations and Landau theory of phase transformations are reported in the first section. The spontaneous polarization mismatch in ferroelectric-ferroelectric (FE-FE), FE-paraelectric (FE-PE), and FE-dielectric (FE-DE) bilayers results in a non-linear electrostatic coupling which produces significant deviations in the overall dielectric response if it is computed using the simple capacitor-in-series (CIS) model. Our results show that the CIS approach is a good approximation only for DE-DE multilayers and for FE heterostructures if the individual layers are electrostatically screened from each other. Furthermore, our findings indicate that a negative dielectric constant in such constructs is thermodynamically not feasible. We provide an alternative explanation for the recent observations that seem to suggest that negative capacitance can be obtained in FE multilayers wherein the total dielectric constant is computed using the CIS model.

In second section, the experimental measurement for achieving high dielectric response over a wide temperature range was reported from our collaborators Deepam *et al.* at Virginia Tech.[123] The multilayer ceramic het-

erostructures with various constituent compositions are constructed for having strategically tuned Curie temperature. Moreover, these multilayer structures exhibited different dielectric behavior in series and parallel configuration due to variations in electrical boundary conditions resulting in the differences in the strength of the electrostatic coupling. It suggests the approach for designing high performance ceramic capacitors.

3.1 Are ferroelectric multilayers capacitors in series?

3.1.1 Introduction

The heterostructures of multilayers and superlattices have attracted significant interests because of their enhanced and novel functionality.[124] Quantum mechanical calculation has become the standard approach to tackle the problem in atomistic level.[125–129] On the other hand, phenomenological methods are applied to study the ferroelectric (FE) systems in the macroscopic scale. Using such continuum models, it is also possible to predict the electrical properties of epitaxial multilayers and superlattices by taking into account the gradient of polarization along the film thickness and size effects in the free energy expansion along with the appropriate electromechanical boundary conditions.[130,131] Regardless of the approach, theoretical works and experimental results indicate that the coupling between individual layers/units in a heterostructure should be taken into account.[132–136] Instead of showing the same or similar behavior of the individual layer, the properties of multilayer heterostructures might be-

come entirely exotic. For a FE-paraelectric (PE) heterostructure, it has been demonstrated that electrostatic interlayer interactions enhance the dielectric properties at a critical layer fraction corresponding to vanishing/appearance of out-of-plane polarization.[137,138]

It has been shown both theoretically and experimentally that introducing buffer layers to a FE film improves the dielectric properties,[139] specifically the loss and leakage characteristics.[116,140,141] Such buffer layers prevent charge injection from the electrodes and prevent inter-diffusion of species between the FE and the substrate that may lead to formation of non-FE compounds.[142,143] A bilayer/multilayer structure with a thin non-FE dead layer can also be formed unintentionally during processing of FEs. The dielectric constants of such dead layers have been estimated using the conventional capacitance-in-series model.[144–146]

Although these studies have provided some insights on the behavior of the heterostructures, two concerns remain unexplored. The dielectric responses of multilayer system have been intensively studied with dependences of material combination, superlattice periodicity and layer fraction,[147–150] but a few attentions were drawn on the effect of the interfacial charge.[135,151,152] It is well known that the control over the layer fraction is one of the tuning knobs to enhance the functionality of the heterostructures. Therefore, we theoretically analyze heterostructures constructed from a variety of commercially attractive FE and dielectric (DE) materials and emphasize the influence of the interfacial

charge on the dielectric properties as a function of layer fraction. Second, the concept of negative capacitance from a ferroelectric was proposed by replacing the standard insulator with a ferroelectric insulator at room temperature. The argument is based on the assumption that a metastable state very close to Curie temperature can be stabilized and become stable in a FE-DE bilayer heterostructure.[153–155] Therefore, it is implicitly claimed using the conventional formula of capacitors in series that the FE layer with a certain thickness shows a negative capacitance very close to the FE instability of the whole heterostructure without providing an extensive theoretical reasoning as to justify this argument.[156,157] It is still a striking puzzle whether in the industrial interests perspective or in the fundamental physics point of view. We propose the possible explanation that misinterpreting experimental results might inadvertently deduce the negative capacitance.

In this study, we systematically investigate four different bilayer heterostructures using the well-established phenomenological thermodynamics model, where electrostatic interaction is taken into account. To illustrate the concept in the most compact way, the current study is focused on the bilayer system and can be analogously extended to multilayer structure. Barium titanate/barium strontium titanate (BTO/BST), strontium titanate (STO) and alumina/hafnium oxide (Al_2O_3/HfO_2) are used to represent ferroelectric (FE), paraelectric (PE) and dielectric (DE) materials, respectively. A freestanding bilayer heterostructure with different combination of materials is sandwiched

between the electrodes, where the polarization axis is perpendicular to the layer interface. It has been realized that the interfacial effect might dominant the properties in such heterostructures. Two models are addressed to study the coupling effect and to explain the divergent behavior.

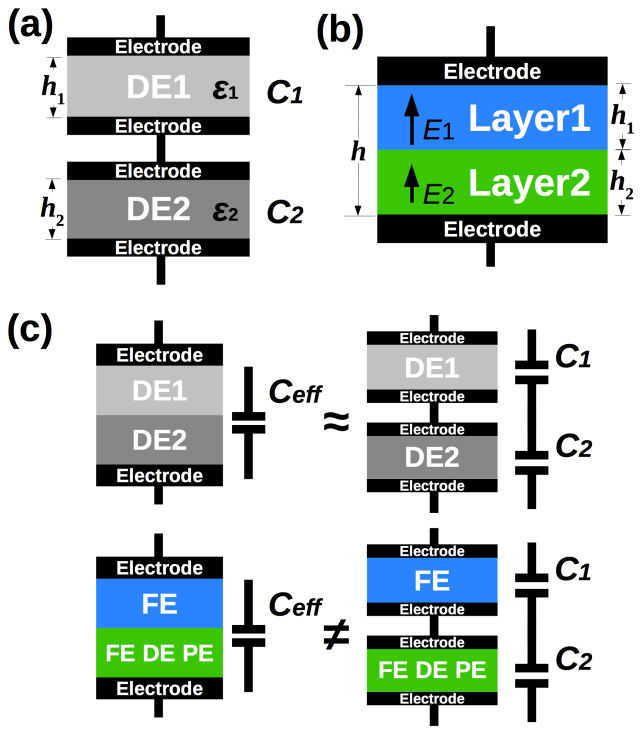

Figure 3.1.1: Schematic representation of freestanding bilayer systems of (a) CIS model and (b) ECM model. (c) Our results show that the CIS model is a good approximation of the ECM approach if the heterostructures consist of two DE or FE layers, but not for FE/DE or FE/PE bilayers.

3.1.2 Capacitors in Series (CIS) Model

By applying Gauss's law, electric field in the region of two metallic plates

with surface area A separated by a distance h in the vacuum can be written as

$$\begin{aligned} \oint_S E \cdot dA &= \frac{Q_{enclosed}}{\epsilon_0} \\ E_0 &= \frac{Q}{A\epsilon_0} \end{aligned} \tag{3.1.1}$$

where Q represents the enclosed charges and ϵ_0 represents the vacuum permittivity. Here we ignore the edge effects and consider the electric field is uniformly distributed within the layers while the layer thickness is relatively smaller than the length in the other two direction (field in the parallel infinite plates). While the dielectric material is introduced, induced electric field will reduce the total electric field with the factor of ϵ, or $E = E_0/\epsilon$ where ϵ is the dielectric constant.

While two dielectric layers are sandwiched with the top and bottom electrodes, potential drop of the bilayer system becomes

$$\begin{aligned} \Delta V &= -\int_{top}^{bottom} E \, \mathrm{d}l = -E_1 h_1 - E_2 h_2 \\ &= -\frac{Q}{A\epsilon_0}\Big(\frac{h_1}{\epsilon_1} + \frac{h_2}{\epsilon_2}\Big) \end{aligned} \tag{3.1.2}$$

where E_i and h_i represent the electric field and layer thickness in layer i ($i = 1, 2$), respectively. Capacitance is defined as the capacity of storing electric charge within the potential difference, or

$$C_{\text{eff}} = \frac{Q}{|\Delta V|} = A\epsilon_0 / \Big(\frac{h_1}{\epsilon_1} + \frac{h_2}{\epsilon_2}\Big). \tag{3.1.3}$$

It is equivalent to two capacitors connecting in series (CIS, Fig. 3.1.1(a)), namely

$$\begin{aligned} C_1 &= \frac{Q}{|\Delta V_1|} = A\epsilon_0 \frac{\epsilon_1}{h_1} \\ C_2 &= \frac{Q}{|\Delta V_2|} = A\epsilon_0 \frac{\epsilon_2}{h_2} \\ C_{\text{eff}} &= \frac{C_1 C_2}{C_1 + C_2} = A\epsilon_0 / \Big(\frac{h_1}{\epsilon_1} + \frac{h_2}{\epsilon_2}\Big) \end{aligned} \tag{3.1.4}$$

where C_i, $i = 1, 2$ represents the capacitance of i-layer.

3.1.3 Electrostatically Coupled Multilayer (ECM) Model

Now, we tackle the problem using nonlinear thermodynamics formalism. The well-established free energy density of the bilayer system, which is sandwiched by the electrode (Fig. 3.1.1(b)), can be expressed as:[137,158]

$$\begin{aligned} F = {} & \alpha_1[F_1(P_1) - EP_1] + \alpha_2[F_2(P_2) - EP_2)] \\ & + \frac{\alpha_1 \alpha_2}{2\epsilon_0}[(P_1 - P_2)^2 - \sigma(P_1 - P_2)] + \frac{F_s}{h} \end{aligned} \tag{3.1.1}$$

where $\alpha_i = h_i/(h_1 + h_2) = h_i/h$, $i = 1, 2$ represents the relative thickness of the layers, P_i represents the polarization of layer i normal to the interlayer interface, E is the applied electric field, σ is the interfacial charge density, F_s/h is the interfacial energy which can be neglected in the study, F_i is the uncoupled free energy density of layer i which can be determined by the Landau expansion coefficient

$$F_i(P_i) = F_{0,i} + \frac{1}{2} a_i P_i^2 + \frac{1}{4} b_i P_i^4 + \frac{1}{6} c_i P_i^6. \tag{3.1.2}$$

The free energy density in Eq. (3.1.1) was derived in detail in our previous

publication.[137,151,159] Furthermore, the electrostatic coupling was constructed through the internal depolarization fields such that the total free energy density can be expressed as:[158]

$$F_{\Sigma} = \sum_{i=1}^{n} \alpha_i \Big(F_{0,i} + \frac{1}{2} a_i P_i^2 + \frac{1}{4} b_i P_i^4 + \frac{1}{6} c_i P_i^6 - E^{\text{ext}} P_i \Big) - \frac{1}{2} \sum_{i=1}^{n} \alpha_i E_{D,i} P_i \tag{3.1.3}$$

where E^{ext} is the applied external electric field and $E_{\text{D,i}}$ is the depolarizing field in layer i.

The coupling of polarizations in each layer can be determined by the equation of equilibrium state $\partial F/\partial P_1 = \partial F/\partial P_2 = 0$. The corresponding electric field in each layer is governed by the electrostatic boundary conditions $\nabla \cdot D = \sigma$ and $\sum_i E_i h_i = V$, where D is the electric displacement field, E_i is the corresponding electric field in layer i, and V is the potential drop between electrodes. σ is introduced in Eq. (3.1.1) to incorporate the effect of interfacial surface charge, which is associated with the oxygen vacancies or trapped electrons. Moreover, since it is possible to have positive (oxygen vacancies) or negative (trapped electrons) charges within interface, the sign of σ should also be taken into consideration. Positive σ is used in our analysis to simplify the discussion without the loss of generality.

Applying small signal approximation, the effective dielectric constant of the heterostructure can be computed using $\langle \epsilon \rangle \cong \frac{1}{\epsilon_0} \frac{d\langle P \rangle}{dE}$ by the average polarization $\langle P \rangle = \alpha_1 P_1 + \alpha_2 P_2$. Therefore, effective capacitance computed by ECM

model becomes

$$C_{\text{eff}} = \epsilon_0\langle\epsilon\rangle\frac{A}{h} = A\epsilon_0\Big[\frac{1}{\epsilon_0}\Big(h_1\frac{dP_1}{dE} + h_2\frac{dP_2}{dE}\Big)\Big]. \tag{3.1.4}$$

In summary, we calculate the relative dielectric permittivity by

$$\epsilon_{\text{eff}} := \begin{cases} \dfrac{\epsilon_1\epsilon_2}{\alpha_1\epsilon_2 + \alpha_2\epsilon_1} & \text{CIS model} \\ \dfrac{1}{\epsilon_0}\Big(\alpha_1\dfrac{dP_1}{dE} + \alpha_2\dfrac{dP_2}{dE}\Big) & \text{ECM model} \end{cases} \tag{3.1.5}$$

3.1.4 Comparison of CIS and ECM model

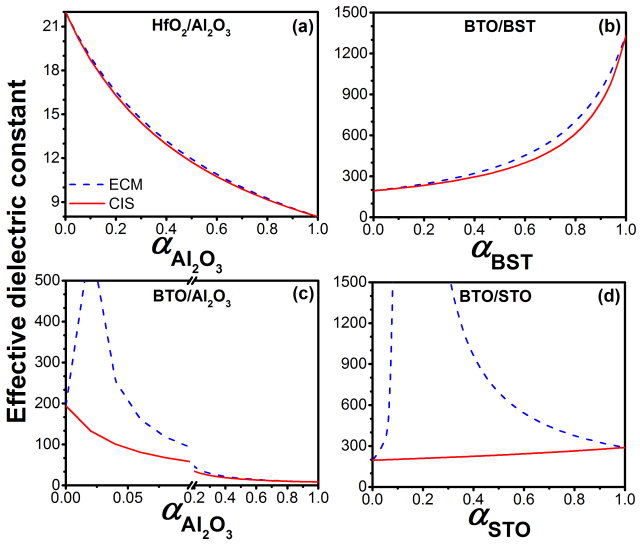

Figure 3.1.2: ϵ_{eff} as a function of layer fraction of four different bilayer systems using both the CIS and ECM approaches: (a) HfO_2-Al_2O_3, (b) BTO-BST, (c) BTO-Al_2O_3, and (d) BTO-STO.

Fig. 3.1.2 compares the relationship between relative dielectric permittivity and layer fraction of a bilayer system for both the CIS and ECM model. Four

different bilayer systems are represented: DE-DE in Fig. 3.1.2(a), FE-FE in Fig. 3.1.2(b), FE-DE in Fig. 3.1.2(c), and FE-PE in Fig. 3.1.2(d). In Fig. 3.1.2(a), the relative dielectric permittivity of DE-DE bilayer decreases from 22 to 8 with increasing $\alpha_{Al_2O_3}$. The calculated values obtained from different models are consistent. In Fig. 3.1.2(b), the relative dielectric permittivity of FE-FE bilayer monotonically increases from one end (BTO only) to the other end (BST only), which was shown in these two models. Because the coupling effect is only considered in ECM model, the discrepancy was observed while α_{BST} is larger than 40% whereas the electrostatic interaction becomes stronger. We note that the tendency remains the same but maximum discrepancy might shift to different layer fraction while we consider different composition of BST. Fig. 3.1.2(c) indicates the different behaviours computed with proposed models while $\alpha_{Al_2O_3} < 0.3$. More specifically, anomalous dielectric response happens at the critical layer fraction $\alpha_{Al_2O_3} \approx 0.8\%$ and can only be predicted by ECM model. The same argument is hold while we consider the combination of BTO and STO bilayer, FE-PE materials, in Fig. 3.1.2(d). The electrostatic interaction is only taken into account in ECM model, which the anomaly can be observed. It is realized that depolarizing field generated in each layer significantly affect by the other layer. Here we emphasize that the conventional CIS model can be used as a good approximation on DE-DE and FE-FE system, which the interlayer coupling is relatively weak. However, ECM model is required to incorporate the stronger coupling while FE-DE and FE-PE cases are investigated.

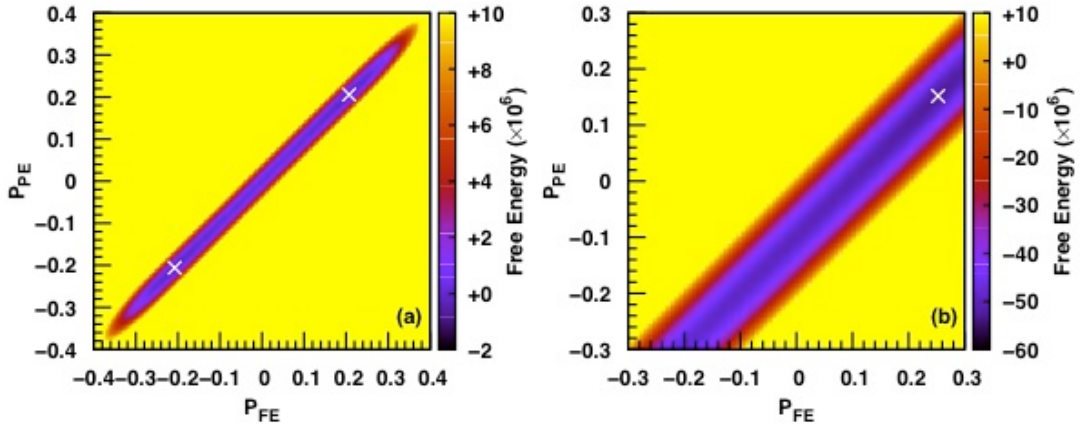

Figure 3.1.3: Free energy profile as the function of polarization in each layer with $\alpha_{\mathrm{STO}} = 0.1$. (a) While $\sigma = 0$, the free energy is symmetric such that the equilibrium polarization P^0_{FE} and P^0_{PE} are equally possible to be pointing upwards or downwards in the direction normal to the interface. (b) While $\sigma > 0$, the symmetry is broken such that there exists only one equilibrium state. The crosses indicate the global minimum in each figure.

ϵ_{eff} of BTO/STO bilayers as a function of the STO layer fraction and the interfacial charge density σ using the ECM model. For comparison, the dielectric response from the CIS approach is shown as well.

In Fig. 3.1.3, the free energy profile of BTO-STO (FE-PE) bilayer with $\alpha_{STO} = 0.1$ is computed as the function of polarization in individual layer, i.e. polarization in BTO layer ($\mathrm{P_{FE}}$) in x axis and polarization in STO layer ($\mathrm{P_{PE}}$) in y axis. While interfacial charge $\sigma = 0$ in Fig. 3.1.3(a), there are two equilibrium states (cross marks in the figure) such that the polarizations are equally likely pointing in either upward ($\mathrm{P_{FE}} > 0$, $\mathrm{P_{PE}} > 0$) or downward direction ($\mathrm{P_{FE}} < 0$, $\mathrm{P_{PE}} < 0$). This reversible electric polarization is one of the principal characteristics of ferroelectric materials. We note that the magnitude

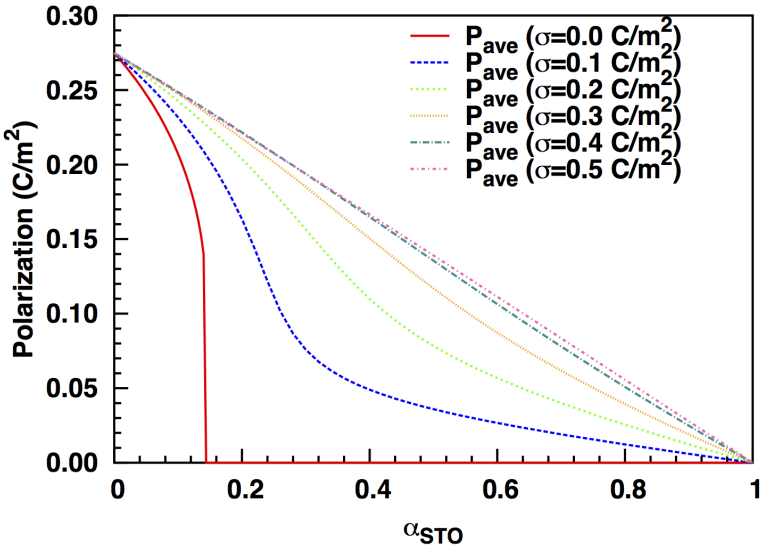

Figure 3.1.4: Average polarization as the function of layer fraction. While interfacial surface charge density $\sigma = 0$, the phase transition happens from FE state to PE state at critical layer fraction $\alpha \approx 0.142$. When $\sigma \neq 0$, the phase transition disappears because induced polarization never becomes zero. [σ unit: C/m^2].

of P_{FE} and induced P_{PE} are very close to, but not equal to each other. While interfacial charge σ is introduced (Fig. 3.1.3(b)), only one state remains stable. Mathematically speaking, the symmetry is broken due to the term associated with σ in Eq. (2.2.1). In physics point of view, the introduced positive interfacial charge enhances the polarization in top FE layer (P_{FE} increases) but suppresses the polarization in bottom PE layer (P_{PE} decreases).

Figure 3.1.4 plots the average out-of-plane polarization of freestanding BTO-STO bilayers as a function of STO layer fraction with and without interfacial charges. While $\sigma = 0$, average polarization (P_{ave}) decreases with increasing

layer fraction of STO. When critical layer fraction (α_c) is reached at $\alpha_{STO} \approx 0.14$, P_{ave} vanishes and ferroelectric to paraelectric phase transition occurs. On the other hand, polarization is smeared out in the presence of interfacial charges ($\sigma \neq 0$) and non-zero polarization values can be realized even above the critical STO layer fraction α_C of charge-free bilayers. This is as expected because the misfit polarization is compensated by the interfacial charge, the induced electronic polarization by such charges suppresses the phase transition. The change in polarization as a function of STO layer fraction becomes nearly linear for bilayers with interfacial charges higher than 0.4 C/m^2. In addition, the average polarization is more susceptible to changes in α_{STO} for bilayers with relatively lower density of interfacial charges, e.g. σ=0-0.2 C/m^2 range. The experiment[160] has shown that electrical properties are sensitive to the presence of interfacial charge and the functionality can be utilized for different application.[161] The ability of altering the interfacial charge might become one of the approaches to engineering the structural properties in the nearly future.[162]

The relative dielectric permittivity of freestanding BTO-STO bilayers is shown as a function of α_{STO} in Fig. 3.1.5. The dielectric anomaly vanishes as the interface charge density reaches very high value (0.5 C/m^2) accompanied with a broadened dielectric response. Moreover, α_C is also increased in the presence of interfacial charges owing to screening of the depolarizing fields by such charges; therefore the FE state is stabilized at larger STO layer fractions. The α_C is shifted to ~0.45 when the interfacial charge density is 0.25 C/m^2. This

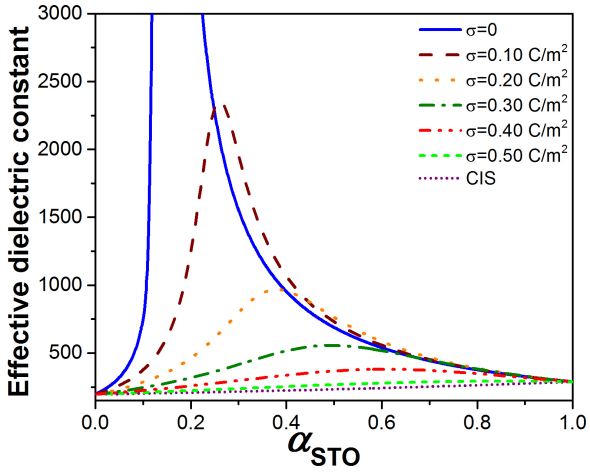

Figure 3.1.5: Relative dielectric permittivity of freestanding bulk BTO-STO bilayers with interfacial charge density σ as a function of STO layer fraction. Effective permittivity of the bilayer calculated from Eq. (3.1.5) is shown for comparison.

number is three times larger than the α_C of bilayers without interfacial charges. The shift in α_C and the suppression of dielectric maxima can be traced from the linearized polarization profiles of bilayers with very high interface charge density in Fig. 3.1.4. The effective dielectric constant calculated from ECM model approaches the values obtained from CIS model when interfacial charge density is very high. This is an anticipated outcome because the effective capacitance is considered as the decoupled individual layers connecting in series. The depolarizing fields are screened by interfacial charges, and the dielectric anomaly vanishes, i.e. both layers behave independently and both models give the similar result by Eq. (3.1.5).

3.1.5 Discussion

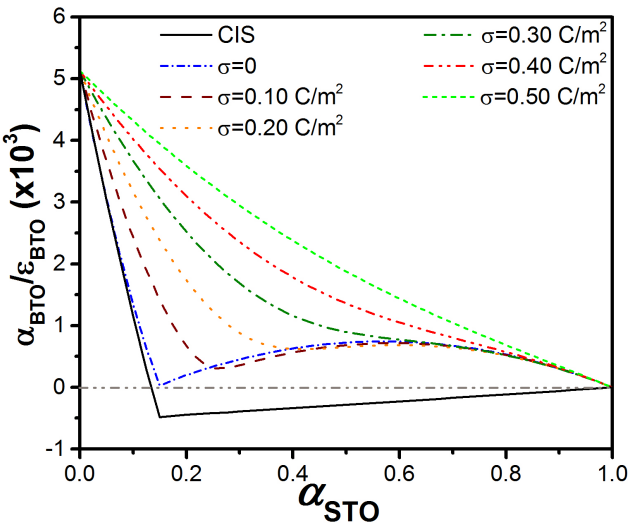

Figure 3.1.6: The quantity $\alpha_{\mathrm{BTO}}/\epsilon_{\mathrm{BTO}}$, which is associated with the capacitance of ferroelectric BTO layer, is computed as the function of layer fraction taking interfacial charge density into consideration. (a) is obtained from ECM model. (b) is computed using the assumption of fixed bulk dielectric constant in STO.

Direct measurement of capacitance for individual layer within the multilayer configuration requires extra design on experimental equipment, there are only a few experiments trying to address such issue with unavoidable complexity. Practically, it is well known that flat plate capacitance C is proportional to the dielectric constant ϵ and is related to the geometric structure, or $C = \epsilon A/d \propto \epsilon/d$ where A is the layer surface area and d is the layer thickness. Here the dielectric response of individual layer (i.e. ϵ_{BTO} and ϵ_{STO}) can be computed and entire bilayer system (ϵ_{eff}) can be approximated by proposed thermodynamic approach. We were convinced that the individual and effective capacitances computed by ECM model, which the interfacial interaction and interfacial charges are taken into account, would be the expected value as

measured from the experiment. With the assistance of conventional capacitor in series formula, effective capacitance of BTO-STO bilayer system obey the relation

$$\frac{1}{\epsilon_{\text{eff}}} = \frac{\alpha_{\text{BTO}}}{\epsilon_{\text{BTO}}} + \frac{\alpha_{\text{STO}}}{\epsilon_{\text{STO}}} \tag{3.1.1}$$

In Fig. 3.1.6 the quantity $\alpha_{\text{BTO}}/\epsilon_{\text{BTO}}$, associated with the capacitance of ferroelectric BTO layer, is computed as the function of layer fraction. In Fig. 3.1.6(a), the anomaly at critical layer fraction disappears while the interfacial charge is introduced. While the interfacial charge density increases, the behavior becomes more regularly. The inverse of C_{BTO} decreases proportionally to increased STO layer thickness with the very large trapping interfacial charge. More importantly, all the computed values are positive. On the other hand, the indirect approach has been used to evaluate the capacitance in ferroelectric layer by the known capacitance of dielectric/paraelectric material and the measured effective capacitance. In Fig. 3.1.6(b), we compute $\alpha_{\text{BTO}}/\epsilon_{\text{BTO}}$ through ϵ_{eff} obtained from ECM model and the fixed ϵ_{STO} value using Eq. (3.1.1). At certain criteria the computed value becomes negative. Moreover, the range given negative quantity is broadened if the interfacial charge is smaller. We emphasize the incorrect assumption of using fixed value of individual capacitance (i.e. STO in this demonstration) might accidentally give the misleading conclusion that the ferroelectric capacitance is negative.

3.1.6 Conclusion

In summary, anomalous behavior of relative permittivity predicted in the vicinity of the critical layer fraction can be captured by nonlinear thermodynamics model considering electrostatic interfacial coupling effect. Depending on the combination of the layer materials, different types of dielectric responses were obtained by controlling the relative layer fraction. It turns out the conventional capacitors in series model can be used as the approximation of effective dielectric constant only if the interfacial coupling is weak or the misfit polarization is compensated by the sufficient large interfacial charge density. We conclude that misinterpreting the experimental data might accidentally deduce the negative ferroelectric capacitance.

3.2 The Enhancement of Dielectric Response

In this section, collaborative work with the experimental group in Virginia Tech is reported, by using nonlinear thermodynamic model taking into account electrostatic interlayer interaction to investigate the underlying mechanism of interfacial coupling effect. The bilayer architecture is applied in the current theoretical study, but the higher stacking sequence of the layers (multilayer structure) should also be applicable with the same fashion of manner. We report a novel approach for achieving high dielectric response over a wide temperature range. In this approach, multilayer ceramic heterostructures with constituent compositions having strategically tuned Curie points (T_C) were designed and integrated with varying electrical connectivity. Interestingly, these multilayer structures exhibited dfferent dielectric behavior in series and parallel configuration due to variations in electrical boundary conditions resulting in the differences in the strength of the electrostatic coupling. The results are explained using nonlinear thermodynamic model taking into account electrostatic interlayer interaction. We believe that present work will have huge significance in design of high performance ceramic capacitors.[158,163]

3.2.1 Motivation

For ceramic capacitor industry, the high dielectric constant and temperature stability are very important. Depending on the desired properties and working temperature of the device, one should ensure that the materials re-

main in a proper condition without failure. Because of the new development on the high performance electronic materials, the capacitor should have high dielectric constant with thermal stability. Doping engineering has been considered as one of the standard approach to achieve the goal at Curie temperature. Furthermore, the modification on the compositional ratio of the element is also introduced, in order to shift the Curie temperature approach room temperature. Even though lots of efforts have been made, high dielectric constant with high stability in temperature is still hard to achieve. Hence, synthesis of core-shell grain microstructure was performed by Maurya *et al.*[123] to obtain the stable dielectric constant in the wider temperature range. Changing the multilayer architecture consisting of different compositions with varying Curie temperature is systematically demonstrated. However, the explanation of the experimental observation was missing. Thereafter, the theoretical evidence supporting the experimental observation is demonstrated by a nonlinear thermodynamic model, where the critical interfacial coupling effect is emphasized and plays a significant role.

3.2.2 Sample Preparation

The $0.975BaTiO_3{-}0.025Ba(Cu_{1/3}Nb_{2/3})O_3$ (BTBCN) ceramics were synthesized using conventional mixed oxide processing method. Stoichiometric concentrations of CuO (Alfa Aesar, 99.0%), TiO_2 (Alfa Aesar, 99.5%), Nb_2O_5 (Alfa Aesar, 99.5 %) and $BaCO_3$ (Alfa Aesar, 99.8 %) were mixed by ball milling

for 24h with ZrO2 balls in polyethylene bottle and calcined in the range of $800 - 1000\ ^{\circ}C$ for 2 hours. Calcined powder was again ball milled to achieve homogeneous powder. In order to synthesize Sn-doped $0.975BaTi_{1-y}Sn_yO_3$-$0.025Ba(Cu_{1/3}Nb_{2/3})O_3$ ceramics (y = 0.015, 0.025, 0.035, 0.05, 0.06); stoichiometric concentration of SnO_2 (Alfa Aesar, > 99%) was added to the base matrix before first ball milling. These ceramics powders were mixed with the binder system and ball-milled for 24 h to get homogenous slurry. This slurry was tape casted using doctor blade with the blade height of 400 μm resulting in 50 μm thickness of the dried green tape. These tapes were cut in desired shape and laminated together with different compositions to achieve the desired thickness. After binder burnout, sintering was performed at $1350\ ^{\circ}C$ for 2h. The total thickness of various multilayer compositions was kept around 2.0 mm irrespective of the number of layers (e.g. bilayer had two layers with each layer having thickness of 1.0 mm). To achieve 2.0 mm thickness of sintered capacitor, almost 70 tapes were stacked together. The variations in the thickness of layers for the different compositions were achieved by controlling the number of green tapes in the stack. The geometry of the parallel and series capacitors were kept similar with the dimension of the 3x3x2 mm^3 and therefore similar aspect ratio.

3.2.3 Experimental Results

Figure 3.2.1 shows the dielectric constant as a function of temperature at

various frequencies for pure and Sn-doped derivatives of $BaTiO_3$-$Ba(Cu_{1/3}Nb_{2/3})O_3$ (BTBCN). By increasing the doping level of Sn, one can easily observe that the shift of Curies temperature moves toward room temperature. The bell shape distribution of dielectric constant becomes wider while Sn increases. This should be realized being associated with the charge compensation due to the new created point defects by substituting Ti^{+4} by Cu^{+2}, Nb^{+5}, and Sn^{+2}. Interestingly all the compositions show very small value of loss tangent factor (< 1.6%) over a wide temperature range including phase transitions. The low loss feature of the materials, especially around the Curie temperature is desired in order to have a high performance capacitor. These results suggest BTBCN and its doped derivatives are quite suitable for ceramic capacitor applications. Next, Maurya *et al.* utilized these compositions to synthesize multilayer structures for ceramic composite capacitors. The fabricated bilayer, trilayer and multilayer with varying compositions and performed dielectric measurements in parallel and series electrical configurations are shown in schematic representation in Figure 3.2.2.

Figure 3.2.3 shows the temperature dependent dielectric constant and loss tangent at various frequencies for bilayer composites in parallel and series configurations. In series configuration, the Curie point corresponding to constituent compositions was not prominent especially for heavily doped composition. However, on measuring the dielectric response of the composites in parallel configurations (Figure 3.2.3a), the Curie peaks corresponding to both

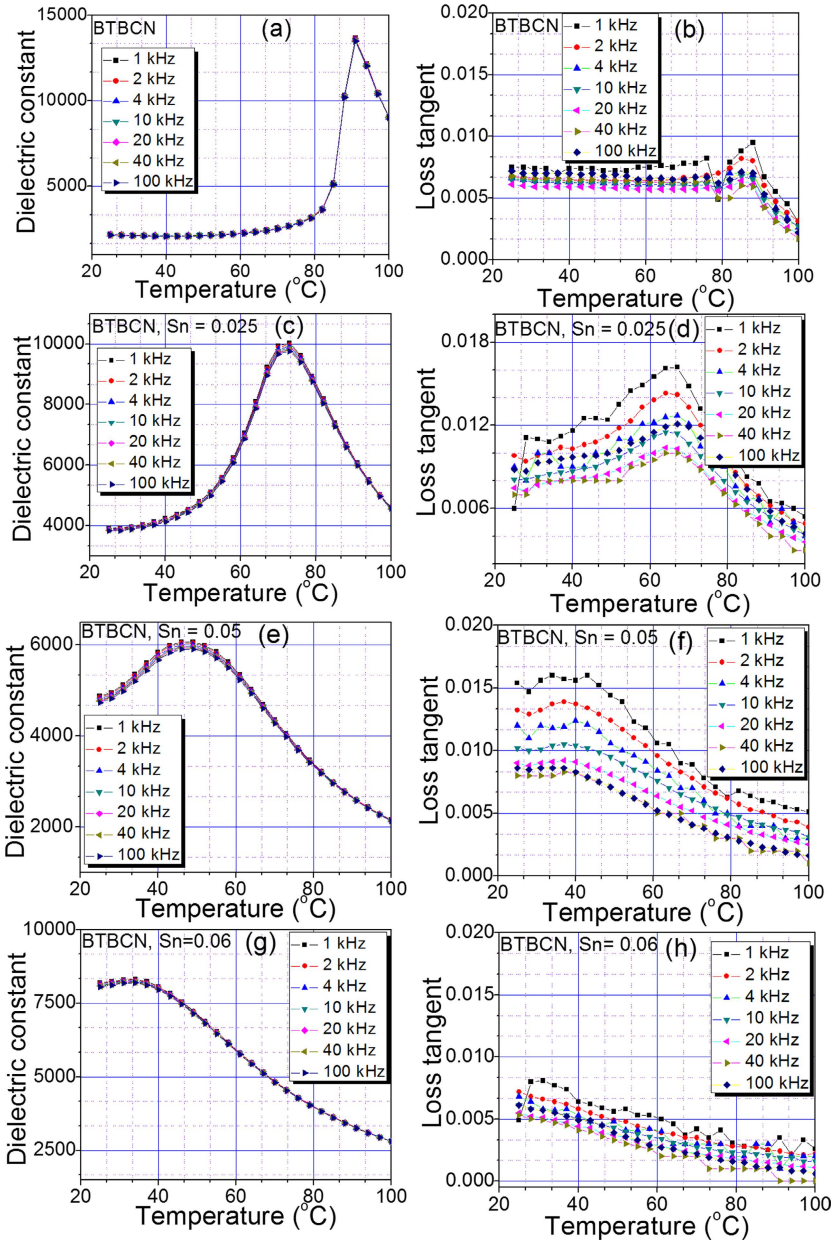

Figure 3.2.1: The temperature dependence of the dielectric response for various constituent compositions of laminate composites. Temperature dependence of dielectric constant and loss tangent at various frequencies for BTBCN with: (a,b) Sn = 0.0, (c,d) Sn = 0.025, (e,f) Sn = 0.05, (g,h) Sn = 0.06.

the compositions were quite prominent exhibiting high dielectric permittivity.

The values of loss tangent (< 0.8% for parallel and < 0.15% for series configura-

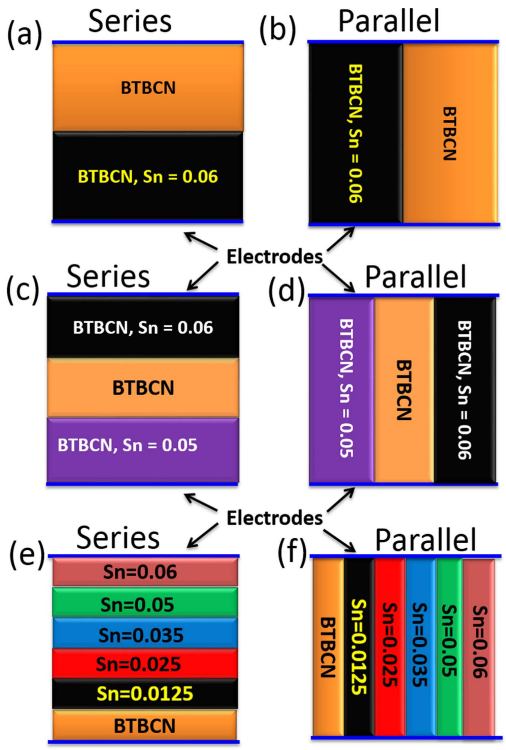

Figure 3.2.2: Schematic representations of various ceramic composites fabricated in this work. Series and parallel structures of (a,b) bilayer, (c,d) trilayer, (e,f) hexa-layer composites. The schematic representation are not to scale.

tions) were also quite low in the given temperature range. However, to reduce the temperature dependent dielectric response, we synthesized new trilayer composite having additional composition with different Curie temperature. In this configuration, BTBCN with higher Curie temperature was sandwiched between two Sn doped ceramic compositions.

3.2.4 Theoretical Modeling

In order to describe the phase transition characteristics and the dielectric properties of the two different configurations of the bilayers and the composi-

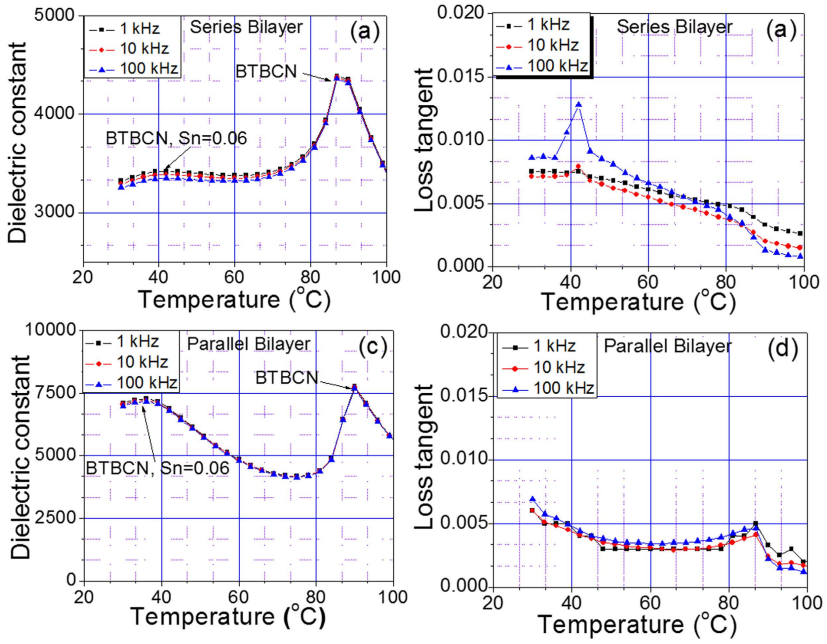

Figure 3.2.3: The phase transition behavior for bilayer laminate composites. The dielectric constant and loss tangent versus temperature plots at various frequencies for bilayer composites in: (a,b) series configuration, (c,d) parallel configuration.

tionally graded multilayers as a function of temperature (T), we employed a nonlinear thermodynamic model taking into account the electrostatic interaction between layers. We note that experimentally observed dielectric properties of ferroelectric multilayers have usually been described via a simple capacitor-in-series models. This, however, is only an approximation and cannot explain several unique properties of ferroelectric multilayers. Our approach was initially developed for freestanding and heteroepitaxial ferroelectric bilayers and has since been expanded to understand the electrostatic and electromechanical coupling in multilayer and polarization graded ferroelectrics. The relevant thermodynamic, elastic, and electromechanical coefficients of Sn-modified

$0.975BaTiO_3{-}0.025Ba(Cu_{1/3}Nb_{2/3})O_3$ (BTBCN) have not been determined experimentally. As such, to provide a meaningful explanation of experimental results, we considered $Ba_xSr_{1-x}TiO_3$ [BST x/(1-x)] as a model system for the theoretical computations. The Curie temperature of BST (90/10) is around 90 $^{\circ}C$, which is close to the T_C of BTBCN. An increase in the Sr concentration in BST results in a reduction of T_C, which is similar to the Sn-modified systems. The theoretical dielectric response of BST as a function of T obtained from the standard Landau theory of phase transformations is shown in Figure 3.2.4 as a reference.

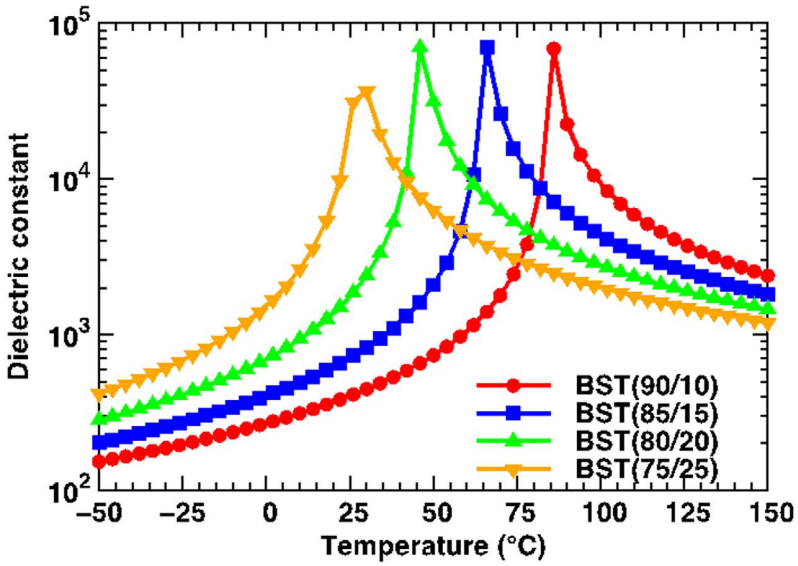

Figure 3.2.4: The phase transition behavior for various BST films having different compositions. The theoretical dielectric response as a function of temperature for monolithic, freestanding BST.

The total free energy density for a multilayer ferroelectric can be expressed

as:[158]

$$F_{\Sigma} = \sum_{i=1}^{n} \alpha_i \Big(F_{0,i} + \frac{1}{2} a_i P_i^2 + \frac{1}{4} b_i P_i^4 + \frac{1}{6} c_i P_i^6 - E^{\text{ext}} P_i \Big) - \frac{1}{2} \sum_{i=1}^{n} \alpha_i E_{D,i} P_i \tag{3.2.1}$$

with

$$\frac{1}{2} \sum_{i=1}^{n} \alpha_i E_{D,i} P_i = -\frac{\kappa}{2\epsilon_0} \sum_{i=1}^{n} \alpha_i (1 - \alpha_i) P_i^2 + \frac{\kappa}{\epsilon_0} \sum_{i=1}^{n-1} \Big[\alpha_i P_i \Big(\sum_{j=i+1}^{n} \alpha_j P_j \Big) \Big] \tag{3.2.2}$$

where α_i the volume fraction of layer i, $F_{0,i}$ is the free energy density at para-electric phase, P_i is the polarization of layer i perpendicular to the electrode surface, a_i, b_i and c_i are the dielectric stiffness coefficient of layer i. E^{ext} is the applied external electric field and $E_{\text{D,i}}$ is the depolarizing field in layer i.

For short-circuit boundary conditions, the potential drop between electrodes should be zero, or

$$\sum_{i=1}^{n} l_i E_{\text{D,i}} = 0 \tag{3.2.3}$$

where l_i is the thickness of the i-th layer. The normal components of electric displacement field D on adjacent side of the boundary surface are related according to

$$(D_{i+1} - D_i) \cdot k_{i+1,i} = \sigma_{i+1,i} \tag{3.2.4}$$

where i=1,2,$\cdots$,$n-1$. Here, $k_{i+1,i}$ is a unit vector normal to the surface, directed from media $i+1$ to media i and $\sigma_{i+1,i}$ is the macroscopic surface charge density

at a given interface.28 For n-layered case, we can rewrite Eq. 3.2.4 as

$$(P_i - P_{i+1}) + \epsilon_0(E_{D,i} - E_{D,i+1}) = \sigma_{i+1,i} \tag{3.2.5}$$

By introducing a scaling parameter κ, the surface charge density can be expressed as:

$$\sigma_{i+1,i} = (1 - \kappa)(P_i - P_{i+1}) \tag{3.2.6}$$

Therefore, $0 \leq \kappa \leq 1$ entering Eq. 3.2.2 is a parameter that characterizes the strength of the coupling between layers and is related to charges that may exist in the multilayer composite. This can compensate for the depolarizing fields between layers that are generated due to the polarization mismatch. For $\kappa = 0$, individual layers are completely decoupled because the internal fields due to polarization variations are entirely compensated by free charges in the multilayer composite. For this case, the total free energy is simply the sum of the free energies of each layers that can be expressed as Landau expansions in the polarization (first term in Eq. 3.2.1) since Eq. 3.2.2 is equal to zero. For $\kappa = 1$, there are no (localized) compensating charges at the interlayer interfaces resulting in strong depolarizing fields as described by Eq. 3.2.2.

By theoretical analysis, two different configurations of ferroelectric bilayers are demonstrated and multilayered ferroelectrics with systematical variations in the composition can then be applied in the same fashion of manner.

Figs. 3.2.5(a) and 3.2.5(b) show schematic representation of the two bilayers that were analyzed. We show schematically that the interlayer interfaces between the ferroelectric layers are parallel and perpendicular to the electrodes in Figs. 3.2.5(a) and 3.2.5(b), respectively. Figure 3.2.5(a) corresponds to the condition where the polarizations in each layer are strongly coupled whereas in Figure 3.2.5(b) the coupling is weak if the easy axis of the polarization in the layers is parallel to the z-direction. As such the bilayer configurations in Figure 3.2.5(a) and 3.2.5(b) can be numerically modeled via the free energy functional given in Eq. 3.2.1 and 3.2.2 with $\kappa \approx 1$ and $\kappa \approx 0$ describing Figures 3.2.5(a) and 3.2.5(b), respectively. Eqs. 3.2.1 and 3.2.2 with $\kappa \approx 1$ have been used to calculate dielectric properties of ferroelectric multilayers with an arrangement of layers as illustrated in Figures. 3.2.5(a) and 3.2.5(c). The justification for the approximation employed to describe the polarization and dielectric response of the configuration shown in Figure 3.2.5(b) (and by extension, Figure 3.2.5(d)) is provided by Chen *et al.*[164] wherein the authors show that the "sideways" coupling of polarization in such a ferroelectric layer is insignificant if the layer thicknesses are much larger than the transition length of the polarization from one layer to another (of the order of 1 nm). This is indeed the case for the multilayers analyzed in this study. As such, the polarization in each layer for the geometry in Figure 3.2.5(b) is very weakly coupled with $\kappa \approx 0$ for which the total free energy can be expressed as the summation of the free energies of each layer. Figures 3.2.5(c) and 3.2.5(d) illustrate two different

configurations of compositionally graded ferroelectric multilayer composites. Theoretically, these could be treated as extensions of the bilayer systems in Figures 3.2.5(a) and 3.2.5(b), respectively.

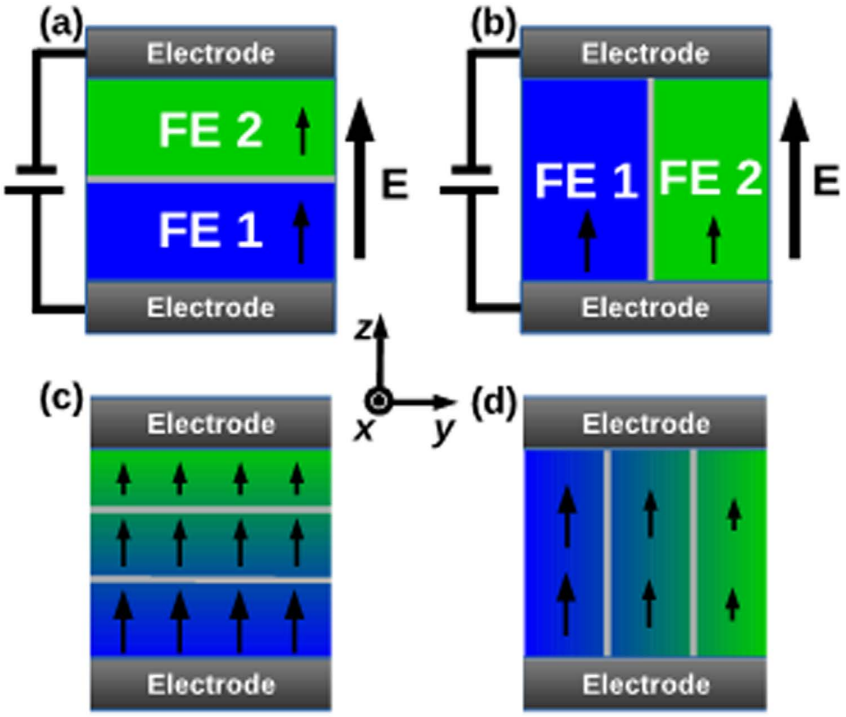

Figure 3.2.5: Schematic representations of the systems analyzed theoretically. (a) and (b) show two different configurations where the interface between the ferroelectric layers are parallel and perpendicular to the electrode, respectively. Configuration (a) corresponds to the condition where the polarizations in each layer are strongly coupled whereas in (b) the polarizations are weakly coupled. Likewise, (c,d) show compositionally graded constructs with the strongly and weakly coupled polarizations, respectively.

The small-signal average dielectric constant is calculated using

$$\langle \epsilon \rangle \cong \frac{1}{\epsilon_0} \frac{d\langle P \rangle}{dE} \tag{3.2.7}$$

where

$$\langle P \rangle = \sum_{i}^{n} \alpha_i P_i^0 \tag{3.2.8}$$

is the average polarization and P_i^0 follow from the equations of state, $\partial F_\Sigma / \partial P_i = 0$.

In Figs. 3.2.6(a) and 3.2.6(b), we plot the equilibrium polarizations in the layers that make up the bilayers in Fig. 3.2.6(a) and 3.2.6(b), respectively, as well as the average polarization of the bilayer. We choose an equi-fraction BST (90/10) / BST (75/25) bilayer in our analysis (bulk T_C = 82°C and 26°C, respectively). We note that properties of ferroelectrics, such as polarization, T_C and dielectric response, are extremely sensitive to the processing/deposition procedures and conditions. While extremely high-quality ceramic multilayers can be produced as shown in this study, it is difficult to compare the properties of interlayer interfaces in such samples to "perfect" heteroepitaxial, ultra-thin heterostructures.[165] Considering the mixed ionic and covalent interatomic bonding in perovskite ferroelectrics, their susceptibility to the formation of oxygen vacancies, and the presence of other structural defects such as impurities, dislocations, grain boundaries which have stress fields that generate commensurate polarization variations, the coupling between interlayers becomes extremely complex.[166] Taking into account that the interfaces in bulk ceramic samples are less than perfect ($\kappa \approx 1$ − no space charges), we take κ

= 10^{-4} for configuration of Figure 3.2.6(a), which corresponds to a modest, space charge density (0.05 0.15 C/m^2). Due to the coupling, equilibrium polarizations and gradually decrease and vanish around the same temperature (approximately 78°C). We note that Curie temperature of BST (90/10) layer does not vary significantly from monolayer ($T_C \approx 82°C$) to bilayer ($T_C \approx 78°C$) system but T_C of BST (75/25) shifts from 26°C in a monolayer to 78°C in bilayer case. In Figure 3.2.6(a), the average polarization smoothly decreases until the sudden drop at T_C of the bilayer. On the other hand, for the highly decoupled case $\kappa = 10^{-10} \approx 0$ corresponding to Figure 3.2.6(b), $P_i^0$and P_2^0in bilayer system display similar phase transformation characteristics of bulk BST (90/10) and BST (75/25) with $T_C \approx 82°C$ and 26°C, respectively. The weakly coupled bilayer system behaves as the combination of two independent freestanding single layers as evident from the average polarization in Fig. 3.2.6(b).

The dielectric properties of the two bilayers in Figure 3.2.5(a) and 3.2.5(b) follow from the polarization response shown in Figure 3.2.6(b) and 3.2.6(b). In Figure 3.2.7, we computed the average dielectric response for the freestanding, stress-free, equi-fraction $Ba_{0.9}Sr_{0.1}TiO_3$/$Ba_{0.75}Sr_{0.25}TiO_3$ bilayer as a function of temperature to investigate the effect of the interlayer coupling. For $1 \geq \kappa \geq 10^{-3}$, the coupling strength is relatively strong. As such, the bilayer system behaves as if it were a uniform ferroelectric material with a single sharp maximum in the dielectric behavior vs. T corresponding to approximately the average composition of the bilayer.[158] For $\kappa = 10^{-4}$, the interlayer interface is slightly decoupled

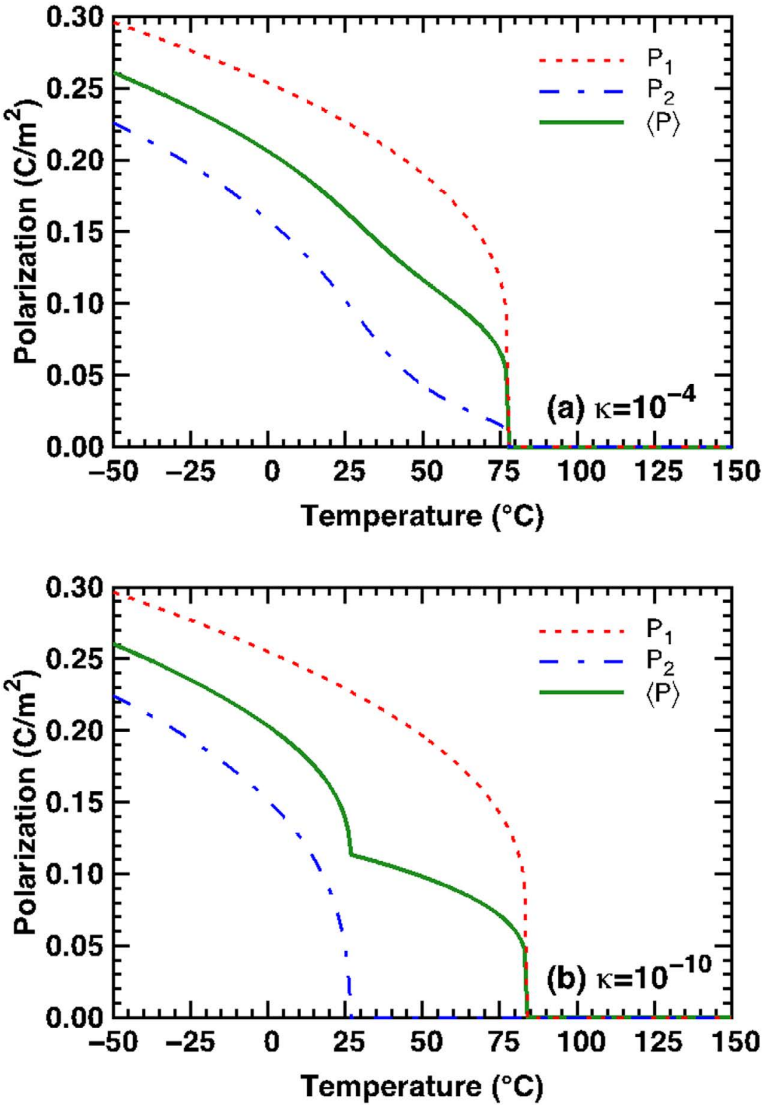

Figure 3.2.6: Effect of coupling on the polarization versus temperature plots for the BST bilayer system. BST (90/10) + BST (75/25) bilayer system with (a) strongly coupled polarization and (b) weakly coupled polarization, corresponding to configurations described in Fig. 3.2.2(a),(b) respectively.

and the average dielectric response is smeared out over a temperature range instead of a $\lambda-$type response for $\kappa \approx 1$. For $\kappa \approx 0$, there are two distinguishable peaks in the dielectric response corresponding to bulk BST (90/10) and

BST (75/25). In other words, the layers in such a geometry (having $\kappa \approx 0$) are entirely decoupled and standard relations for capacitors-in-parallel (Parallel) apply. The dielectric response using capacitors-in-series (Series) formula is also shown for comparison. The differences of the approximation using proposed nonlinear thermodynamics model and conventional capacitor formula are significant as expected.[158] Here, our theoretical model was successfully applied to understand dielectric response behavior of compositionally graded multilayer structures as shown in Figure 3.2.5(c) and 3.2.5(d). The trend of variations, of temperature dependent dielectric response of bilayer, with series and parallel configurations, were found to be similar to the theoretically predicted dielectric response behavior. As discussed previously, in series configurations, the bilayer specimen was found to exhibit only one prominent peak due presence of finite coupling at the interface. However, in case of the parallel configuration, Curie peaks due to both the constituents were prominent suggesting negligible coupling between the constituent layers. Similar behavior was observed for trilayer and multilayer composites in series and parallel configurations. Here, we experimentally demonstrated that by designing ceramic composite with strategically tuned phase transitions, high dielectric constant can be achieved over a wide temperature range. The presence of coupling, among constituent layers (depending on the magnitude of κ) of the composite, was found to modulate dielectric responses of the composites. Based on the theoretical results, the bilayer systems with parallel configurations were expected to be characterized

by negligible value of κ (which defines the presence of the charges at the interface) and thereby small coupling between the layers. Moreover, the low loss in multilayer architectures could also be attributed to the interlayer interfaces that would trap mobile point defects to minimize the polarization difference and reduce the coupling. We believe this coupling will be significantly stronger in multilayers of monodomain and fully poled single crystals.

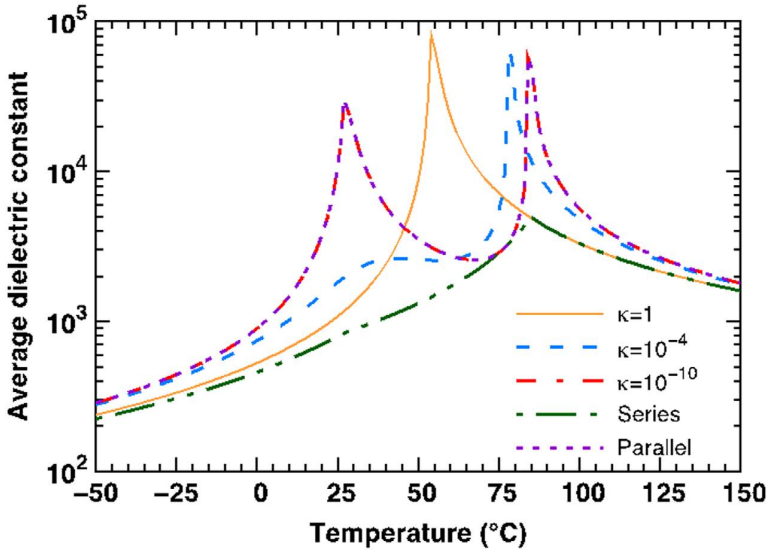

Figure 3.2.7: The magnitude of the coupling modulates the temperature dependence of the average dielectric response. The average dielectric constant of a freestanding, stress-free, equi-fraction $Ba_{0.9}Sr_{0.1}TiO_3/Ba_{0.75}Sr_{0.25}TiO_3$ bilayer is computed as a function of temperature. κ = 1, 10^{-4}, and 10^{-10} represent the strongly coupled, weakly coupled, and decoupled behavior of bilayer system, respectively. The approximations using conventional formulas for capacitor-in-series (Series) and capacitor-in-parallel (Parallel) are shown as well.

3.2.5 Conclusion

In this experimental and theoretical collaborative investigation, we successfully fabricated highly dense multilayer ceramic composite structure with

crack-free interface. These composites were fabricated using novel dielectric compositions having strategically tuned Curie temperatures. The dielectric response of these composites was different in series and parallel configurations. The multilayer specimen, with series configurations, demonstrated enhanced dielectric response over a wide temperature range. We further modelled the results to provide fundamental understanding of this behavior. Theoretical calculations indicated that the finite coupling at the interface modulates the dielectric responses in series and parallel configurations. These results further suggest that the high value of dielectric constant over a wide temperature range can be obtained through precise control of the interfacial coupling. The present work is expected to be helpful in designing advanced capacitive components for the future generations of the electronic devices.

Chapter 4

Temperature Dependent Structural, Elastic, and Polar Properties of Ferroelectric Polyvinylidene Fluoride (PVDF) and Trifluoroethylene (TrFE) Copolymers

Here in this chapter, the molecular dynamics, a type of atomistic simulation method, is utilized to describe a ferroelectric system in nm$-\mu$m length scale (and always in the time scale of nanoseconds). The physical properties are obtained through statistically sampling the interaction between each particles. Just to recall that the philosophy of MD simulation is very different than the electronic structure calculations and the nonlinear thermodynamic model. For electronic structure calculations, the interactions between electrons are explicitly taken cared of by introducing the electronic charge density. On the other hand, the physical properties, presenting by the order parameters where only the macroscopic phenomena of the system but not the microscopic interaction of the particles can be described, are directly computed in nonlinear thermodynamic model. It is worth to mention that the connection between one scheme to another is the key to construct the multiscale type of modeling. We have chosen PVDF using MD approach to investigate its structural and polar properties by modeling PVDF and its P(VDF-TrFE) microstructure. The polar phase

of PVDF is emphasized since the great interest for data storage as a ferroelectric materials. Furthermore, the phase transition behaviors are reported in second part of the chapter. The temperature-induced and deformation-induced type phase transitions are consistent with the experimental observation. It is shown that the representative recipe of atomistic interaction, or more precisely, the force-field potentials are the most important factors to accurately describe the system in MD simulations.

4.1 Introduction

Poly(vinylidene fluoride), PVDF $(\text{-}CH_2\text{-}CF_2\text{-})_n$ and its copolymers with trifluoroethylene (TrFE) or tetrafluoroethylene (TFE) stand out among the small number of known ferroelectric polymers due to their remarkable dielectric, piezoelectric and pyroelectric properties.[167–169] These outstanding electroactive characteristics have been exploited for a wide variety of applications, including biomedical,[170] energy storage,[171] sensors and actuators,[172] and filtration technologies.[173,174] Recent reports also emphasize excellent electrocaloric properties of PVDF and its TrFE copolymer, such as relatively high pyroelectric coefficients and low loss, making them attractive candidates for electrothermal energy harvesting where either the polymer by itself or a composite with a ceramic ferroelectric (*e.g.* $BaTiO_3$ or $Pb(Zr,Ti)O_3$) is used as a working medium.[175–178] Furthermore, relatively low ferroelectric-paraelectric transition temperature (343−413 K)[179] and the inherently large elastic, electrostrictive, and flexoelec-

tric responses of poly(VDF-*co*-TrFE) provide additional degrees of freedom for the development of multifunctional electromechanical and electrothermal devices. Such advanced properties have also triggered efforts in the preparation of well-defined PVDF and its random and block copolymers using controlled radical polymerization methods.[180–183]

The initial interest in elucidating the mechanisms underpinning the remarkable electroactive properties of this polymer family was sparked by the pioneering work of Kawai[184] in 1969, who discovered strong piezoelectricity in the uniaxially-drawn and poled films, and that of Bergman *et al.*[185] in 1971, who reported pyroelectricity in PVDF. However, it was soon realized that on both microscopic and mesoscopic levels, the PVDF structure is quite complex, containing both crystalline and amorphous regions, and exhibiting a variety of phase transitions between different crystalline polymorphs under changing external conditions. Depending on chain conformation and molecular packing, PVDF may have at least four polymorphs: α (form II),[186] β (form I),[186] γ (form III)[187] and δ (form VI).[188] Both α and δ forms include TGTG' (trans-gauche-trans-gauche) chain conformations, with α being non-polar and δ polar due to different orderings of the monomer dipole moments. The ferroelectric β form consists of a quasihexagonal close-packed arrangement of polymer chains in all-trans (TTTT) conformation, with all the monomer units aligned along a single polar axis. Finally, the polar γ form, which can be considered an intermediate phase between α and β, is composed of T_3GT_3G' chain conformations.

PVDF polymorphs can be produced by a number of different processing techniques,[167] *e.g.*, the α phase can be readily synthesized by melt crystallization, while the β phase is normally obtained by the combination of mechanical stretching[189] and electrical poling[190] of α-crystalline PVDF. The γ phase is rather hard to access because it requires relatively high temperatures (~450K)[191] and long term annealing. The δ phase (first observed experimentally more than 40 years ago[190]) can be derived from the α phase by applying high electric fields (1.7MV/cm)[188] that induce the rotation of polymer chains about the backbone axis without any conformational changes. Utilization of higher electric fields (~5MV/cm) was reported to induce an α to β phase transition, accompanied by unfolding of all the gauche bonds into the TTTT chain conformation. Very recent results show that the δ phase can be stabilized via applying a short electrical pulse (2.5 MV/cm) to a thin film at the elevated substrate temperature (373 K).[192] The reported remnant polarization (7 μC/cm^2) and coercive field (1.15 MV/cm) are comparable to those of β-PVDF and poly(VDF-*co*-TrFE).

By virtue of its close-packed crystalline arrangement of the all-trans PVDF chains, among all the abovementioned PVDF polymorphs, the β phase should exhibit the highest polarization and commensurately high electroactive properties, such as piezo- and pyroelectricity. Indeed, this structure is regarded as a mainstay theoretical model for "simple" polymer ferroelectricity. However, experimentally grown β-PVDF samples usually require extensive post-processing to become ferroelectric and even after these procedures they still remain far

from being perfectly ordered (~50-60%).[2] Nevertheless, it was shown that the β phase poly(VDF-*co*-TrFE) can be synthesized with a high degree of crystallinity (~90%) by increasing its TrFE content to 20-30%.[179,193,194]

During the two decades following the discovery of ferroelectricity in PVDF, a variety of classical interacting-dipole approaches had been used to evaluate the polarization and piezoelectric properties of this polymer family.[193,195–197] However, the output of these models was found to be inconsistent due to the lack of mechanisms accounting for redistribution of electronic charges, which could be accomplished only by quantum-mechanics based computational techniques. Nakhmanson *et al.*[1] have applied density functional theory (DFT) to study the polar properties of β-PVDF as a function of TrFE and TFE copolymer content, showing a large polarization enhancement within the crystal (as compared to the properties of individual all-trans PVDF chains) when quantum-mechanical effects are fully taken into account. Thereafter, DFT based methodology has been utilized, *e.g.*, by Wang *et al*,[198] who reported improved stability of the β phase in poly(VDF-*co*-TFE), and (with dispersion corrections) by Bohln *et al.*,[199] who show α and β as the most stable phases for pure PVDF and poly(VDF-*co*-TrFE), respectively. Furthermore, Pei *et al.*[200] have recently computed the structural and elastic properties for nine different polymorphs of PVDF.

Although a considerable amount of modeling effort was dedicated to elucidating the elastic, polar and piezoelectric properties of PVDF crystals, the

dependence of these properties on both the copolymer content and temperature, *i.e.* parameters that are most important for potential electrothermal applications, has not been sufficiently addressed. Due to the complexity and partially disordered nature of the PVDF crystal structure, empirical force field (FF) potentials are currently the most efficient tools capable of providing quantitative predictions of the temperature-dependent physicochemical properties of PVDF and its copolymers at the molecular level. The first such field (called MSXX FF) was parameterized from quantum mechanical simulations for the four already existing, as well as for five theoretically predicted PVDF crystal forms by Karasawa and Goddard,[201] who also computed structural, elastic, and dielectric properties for the experimentally observed phases showing that they are in a good agreement with the information available at the time. Later, Carbeck *et al.* used a quasi-harmonic lattice dynamics approach combined with the Karasawa-Goddard MSXX FF potential to incorporate the effects of electronic polarization and dipole oscillations as a function of temperature.[202,203] A modified FF potential was developed by Tashiro *et al.*[204] to accurately reproduce the structural properties, vibrational frequencies, as well as the IR/Raman spectra of PVDF and poly(VDF-*co*-TrFE). The same group then studied the details of the ferroelectric to paraelectric phase transition[205,206] in poly(VDF-*co*-TrFE) as a function of copolymer content, demonstrating that polymers with larger VDF content have higher transition temperatures, which is consistent with experimental findings.

In this investigation, the classical molecular dynamics (MD) simulations utilizing the well-established FF potential of Abe and Tashiro[206] to evaluate the elastic, polar and pyroelectric properties of β-PVDF as a function of temperature and TrFE comonomer amount is applied. The aforementioned FF model has already been employed for simulations of the ferroelectric-to-paraelectric phase transitions in PVDF.[205–207] Here, we report the temperature-dependent lattice parameters, elastic stiffnesses and spontaneous polarization of the β-poly(VDF-*co*-TrFE) structure, as well as its thermal expansion and pyroelectric coefficients. The obtained structural and elastic properties are in good agreement with previous computational studies.[1,200,201,203] The computed spontaneous polarization exhibits a similar trend with increasing TrFE content as already predicted with the DFT calculations at 0K,[1] but its magnitude is underestimated by about 20%. However, the obtained pyroelectric coefficients of -2.5 to -3.76 (10^{-3} μC/cm^2 K^{-1}) are in good agreement with the reported experimental results, which range from -3.1 to -4.0 (10^{-3} μC/cm^2 K^{-1}).[208]

4.2 Methodology

4.2.1 Force Field

A FF potential is usually specified as a set of equations that describe all of the simulated interactions (including many body) between atoms within a crystal. The parameters of the FF employed in this investigation were taken from Abe, Tashiro, and Kobayashi,[209] which contains modifications from the

original paper of Tashiro *et al.*[204] providing more accurate estimates for the structural properties of PVDF and poly(VDF-*co*-TrFE). Utilizing the modified FF, Tashiro and coworkers have obtained the crystal structure and vibrational frequencies of α, β, and γ phases in agreement with the X-ray data, and studied the β phase ferroelectric-to-paraelectric phase transitional behavior.[206,207] They demonstrated that the modified potential can reproduce experimental phase transition temperatures, at least qualitatively accounting for the effects of chain packing and domain wall motion.

The total energy of the system within this FF can be expressed as

$$E = E_{val} + E_{nb} \tag{4.2.1}$$

where E_{val} represents all the bonded interactions (valence energy) and E_{nb} represents non-bonded interactions. These include

$$\begin{aligned} E_{val} &= E_b + E_a + E_t + E_{ab} + E_{bb} + E_{1aa} + E_{2aa} \\ E_{nb} &= E_{vdWij} + E_Q \end{aligned} \tag{4.2.2}$$

where valence energy E_{val} consists of E_b (bond stretch), E_a (angle bend), E_t (torsional), E_{ab} and E_{bb} (cross terms), E_{1aa} and E_{2aa} (angle-angle terms). Non-bonded energy E_{nb} consists of E_{vdWij} (van der Waals) and E_Q (Coulomb interactions). The 1-2 (bond) and 1-3 (angle) of Coulomb interactions are excluded because these interactions are covered in the valence energy terms. The detailed description of each energy expression can be found in the original work.[204]

4.2.2 Computational Details

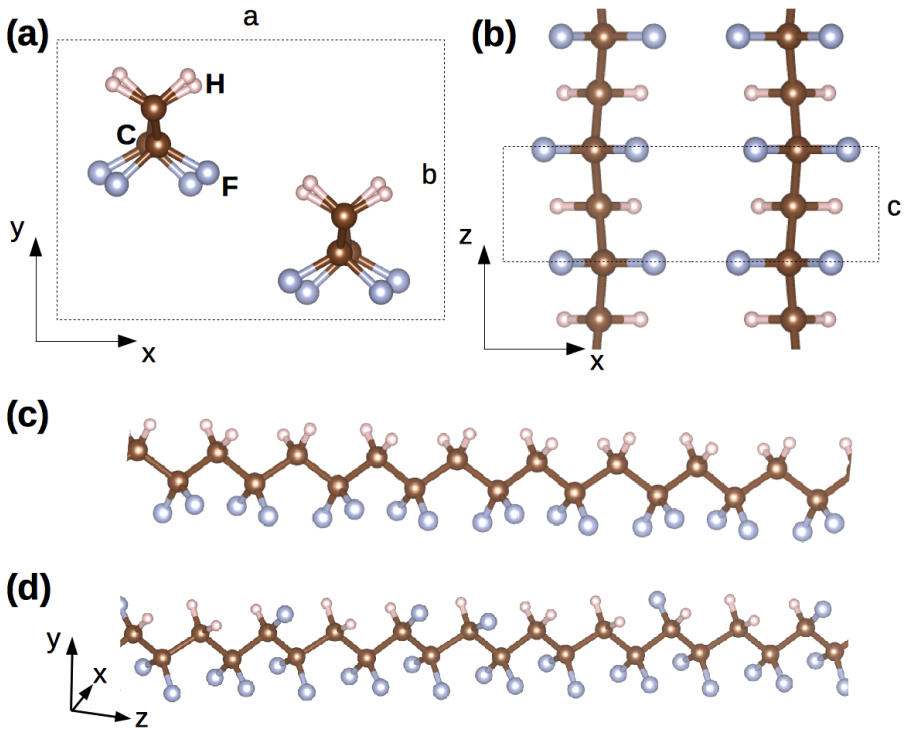

Figure 4.2.1: The crystal structure of β-PVDF and its poly(VDF-*co*-TrFE) copolymer. β-PVDF chain packing shown in (a) x-y plane, and (b) x-z plane. The *a*, *b*, and *c* represent lattice constants. Polymer chain structures of (c) β-PVDF and (d) 50-50 randomized poly(VDF-*co*-TrFE) copolymer. Hydrogen (H) and carbon (C) atoms are represented by small ivory and medium-sized brown spheres, respectively. Fluorine (F) atoms are represented by large blue spheres.

The initial crystal structures for the PVDF and poly(VDF-*co*-TrFE) copolymer systems were generated using Moltemplate[210] and are shown in Fig. 4.2.1. The simulation box setup involved aligning the lattice parameters a, b, and c of the orthorhombic β-PVDF unit cell with Cartesian directions x, y, and z, respectively. In this setup, the y axis is parallel to the direction of the monomer dipole

moments in β-PVDF, while the z axis is parallel to the direction of the polymer chain backbone. Different supercell geometries were tested to evaluate the influence of potential cell size effects on the properties under investigation. The simulation box size of 27Å $\times$ 30Å $\times$ 52Å ($\sim 3a \times 6b \times 20c$), *i.e.*, a arrangement of polymer chains each containing 20 monomers (720 monomers, 4320 atoms total), was found to be sufficiently large, *i.e.*, the change of the unit-cell lattice parameters upon further enlargement of the simulation box was below 0.1%. In all of our simulations, as well as all previous studies,[180–183,211] it is assumed that PVDF follows a perfect head-to-head monomer arrangement. In reality, PVDF obtained from free radical polymerization contains one in 10 to one in 20 units inverted, head-to-head (HH) units.

Three-dimensional periodic boundary conditions (PBC) were applied in all simulations, while simulations involving cell shape and volume relaxation were conducted at a condition of vanishing shear stresses, *i.e.* of preserving the orthorhombic symmetry of the supercell. Fig. 4.2.1(a-b) shows the molecular structure and chain packing of the β-PVDF phase. To accommodate the effect of the steric hindrance between the adjacent fluorine pairs, in our initial models, alternating deflections away from the "planar backbone" symmetry were introduced in consecutive VDF units along each chain.[186] In Fig. 4.2.1(c-d), we illustrate the process of creating a random and atactic VDF-*co*-TrFE copolymer chain out of the pure PVDF, by substituting hydrogen atoms with fluorine. This procedure was used to prepare the initial configurations of poly(VDF-*co*-TrFE)

copolymer-crystal structural models out of relaxed β-PVDF models.

All the energy terms discussed in the previous subsection were encoded in LAMMPS,[212] a classical MD simulation software package that was used to carry out all the calculations described herein. Standard Ewald summation was performed for non-bonded interactions within the cutoff distance of 7.6 Å. The PVDF crystal structure was optimized in a two-step process. On the first step, the system was relaxed to small ionic forces by the conjugate gradient (CG) algorithm in a fixed supercell until the energy change between successive iterations was less than 0.01%. In the second step, the final configuration from the previous step was relaxed further at a temperature below 0.01 K, using the NPT (isothermal-isobaric) ensemble with Parrinello-Rahman method[213] for pressure and temperature control, and Nose-Hoover thermostats,[214,215] until the average of each stress tensor components was below 2 bar.

Nine independent components of the elastic stiffness tensor in the orthorhombic crystal system were evaluated at 0 K by introducing small (±0.5%) distortions to the shape of the simulation cell, and converging the resulting constrained structure back to small ionic forces and energy tolerances. Individual elastic stiffness components C_{ij} could then be computed from the obtained values of stresses σ_i and strains ϵ_j using the tensorial form of Hooke's law

$$\sigma_i = \sum_j C_{ij}\epsilon_j \tag{4.2.1}$$

in conventional Voigt notation.[216]

To simulate the behavior of both the PVDF and poly(VDF-*co*-TrFE) at elevated temperatures, their structural models were equilibrated for 40,000 steps (20 picoseconds) after reaching the target temperature. At the end of that time interval, their properties were sampled for an NPT (isothermal-isobaric) ensemble.

The linear thermal expansion coefficients under constant applied stresses σ and electric field E were obtained as

$$\alpha_i = \frac{1}{x_i}\left(\frac{\partial x_i}{\partial T}\right)_{\sigma,E} \tag{4.2.2}$$

where x_i are the lattice parameters a, b, and c.[216]

Young's modulus along the chain direction E_c was computed by stretching the simulation box along the z-axis (by 2.5%) under fixed-volume condition. E_c is then obtained as the slope of stress-strain dependence

$$E_c = \sigma_c/\epsilon_c \tag{4.2.3}$$

where σ_c and ϵ_c are the stress and strain along the chain direction, respectively.

The polarization of the polymer crystals was computed by the summation over the dipole moments of all the (VDF or TrFE) monomers within the supercell

volume V

$$\mathbf{P} = \frac{1}{V}\sum_{j}\mu_j = \frac{1}{V}\sum_{i}\sum_{j} q_i \mathbf{r_{ij}} \tag{4.2.4}$$

where μ_j is the dipole moment of monomer j, with q_i being the electric charge of atom i, and r_{ij} its Cartesian coordinate vector.

Pyroelectric coefficients along the polar (y) direction were then calculated under conditions of constant stresses and applied electric fields as

$$p_y^{\sigma} \equiv \left(\frac{\partial P_y}{\partial T}\right)_{\sigma,E} \tag{4.2.5}$$

where P_y is the polarization along the y-axis.

4.3 Analysis of Results

Prior to investigating the finite-temperature properties of the polymer crystals, we evaluated the self-energies of different PVDF phases at 0 K. Employing the β phase as a reference, the energies of the δ and α phases were found to be lower by 2.42 and 2.34 (kcal/mol per monomer unit), respectively. These values are consistent with the ones in Ref.[204]. Su *et al.*[217] have observed a similar trend with DFT calculations, reporting the energies of the δ and α phases that are lower than that of the β phase by 0.62 and 0.59 (kcal/mol per carbon atom), respectively. On the other hand, for the 50/50 poly(VDF-*co*-TrFE) copolymer, we found the energies of the δ and α phases to be higher than that of the β phase by 1.94 and 1.80 (kcal/mol per monomer unit), respectively. The same

tendency was observed in DFT calculations,[217] with the energies of the δ and α phases being higher by 2.42 and 1.86 (kcal/mol per carbon unit). These results indicate that substituting hydrogen atoms with fluorines, and thus replacing VDF with TrFE, makes the β phase more energetically favorable, which is also observed experimentally.[179,194]

Table 4.3.1: Lattice parameters, density(g/cm^2), and polarization(μC/cm^2) of PVDF and poly(VDF-*co*-TrFE)

TrFE(%)	Method	a(Å)	b(Å)	c(Å)	ρ	P_b	Ref.
0	Exp	8.58	4.91	2.56	1.97	-	[218]
0	DFT	8.69	4.85	2.58	1.96	-	[200]
0	DFT	8.55	4.83	2.58	2.00	18.5	[1,219]
0	FF	8.39	4.61	2.56	2.15	18.2	[203]
0	FF	8.79	4.88	2.63	1.89	-	[204]
0	FF	8.64	4.82	2.64	1.93	14.9	This Work
10	FF	8.81	4.98	2.64	1.89	13.1	This Work
20	FF	8.93	5.10	2.65	1.86	11.7	This Work
30	FF	9.05	5.18	2.66	1.85	10.5	This Work
40	FF	9.13	5.25	2.66	1.86	9.3	This Work
50	FF	9.26	5.28	2.67	1.86	8.3	This Work

Table 4.3.1, presents the lattice parameters, density and spontaneous polarization for the β-PVDF and poly(VDF-*co*-TrFE) structural models considered in this investigation, at T = 0 K. Similar data from other computations is also included for comparison. Our results show that, with the increasing TrFE amount, the along-the-backbone lattice parameter *c* remains rather constant, while the polar-direction lattice parameter *b* and the remaining lattice parameter a expand strongly, by up to 10% and 7%, respectively, in the 50/50 copolymer. This trend is in a general agreement with other DFT-based calculations,[1] except

for the saturation of the lattice parameter a to a constant value for TrFE amounts of more than 20%. We should, however, point out that the poly(VDF-*co*-TrFE) structural models previously considered in the DFT investigation[1] were rather small (a 2 by 2 configuration of chains, each with 4 monomers), and not well randomized in the TrFE units position assignments at higher TrFE concentrations. Thus, they are most probably more tightly packed, by comparison with the better randomized large models utilized in this study.

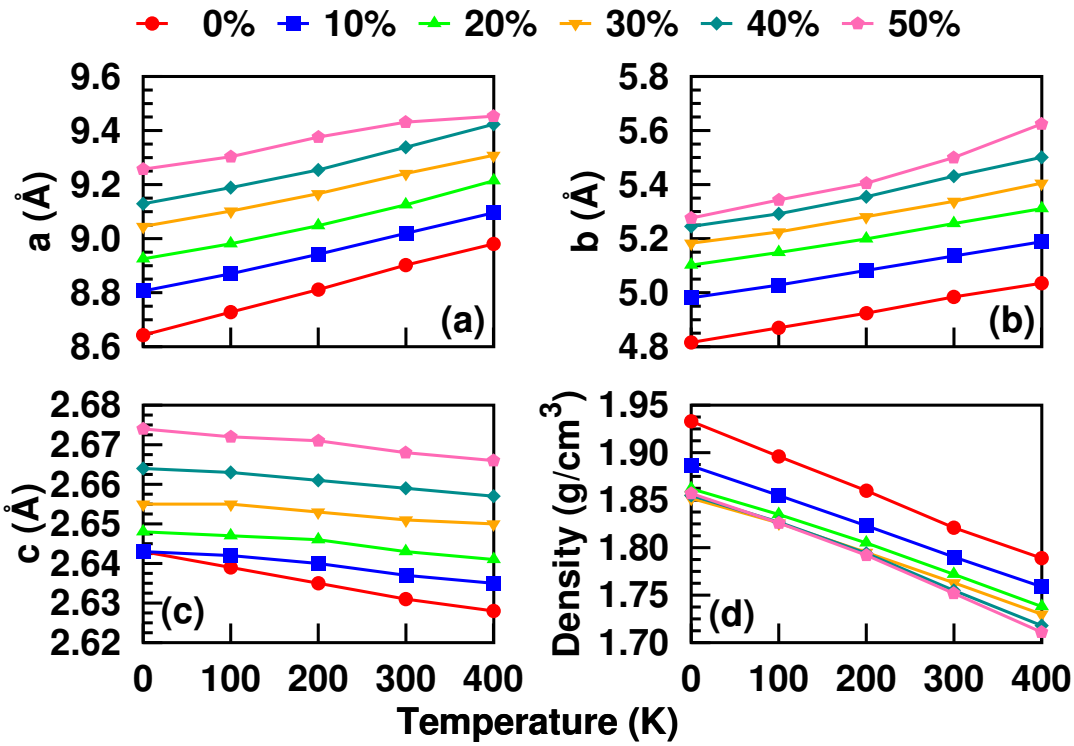

Figure 4.3.1: β-PVDF and poly(VDF-*co*-TrFE) copolymer crystals lattice parameters a, b, and c, and density as functions of temperature.

The evolution of the β-PVDF and poly(VDF-*co*-TrFE) crystals density and lattice constants with changing temperature is presented in Fig. 4.3.1. As the temperature increases, lattice constants a and b expand, while lattice constant

c contracts slightly. This behavior can be attributed to highly anisotropic cohesive interactions within the crystals, *i.e.* the strong covalent bonding between monomers along the polymer chain vs. weak non-bonding between individual chains. The density of each polymer crystal gradually decreases with increasing temperature. At room temperature, we obtain values in the range of 1.75-1.85 g/cm^3 that are consistent with reported experimental results of 1.68 to 1.97 g/cm^3, depending on the crystallinity of the sample.[211]

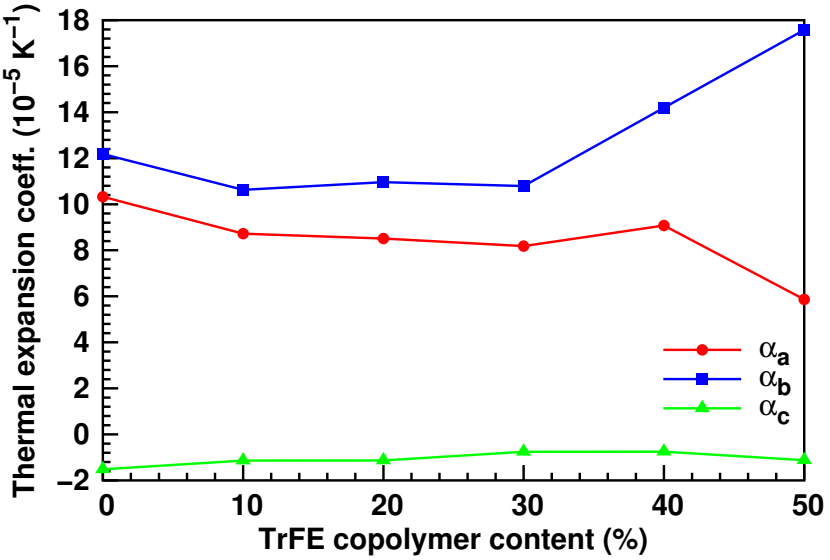

Figure 4.3.2: Room-temperature thermal expansion coefficients of β-PVDF and poly(VDF-*co*-TrFE) copolymer crystals as functions of the TrFE content.

The dependence of the room temperature thermal expansion coefficients on the TrFE copolymer content, obtained from the variation of the lattice constants presented in Fig. 4.3.1, is shown in Fig. 4.3.2. The values of the expansion coefficients α_a and α_b are much larger than that of α_c. Moreover, α_c, which is along the chain direction, is negative and an order magnitude smaller than

the others. Carbeck and Rutledge[203] reported similar values of the thermal expansion coefficients, including slight contraction along the chain direction with increasing temperature.

Although PVDF-based polymers have been studied for decades, their elastic properties remain elusive. This is due not only to partial crystallinity of PVDF or its structural complexity, but also to a wide variety of morphologically different samples that have been produced over the years utilizing a broad range of synthetic techniques.[211]

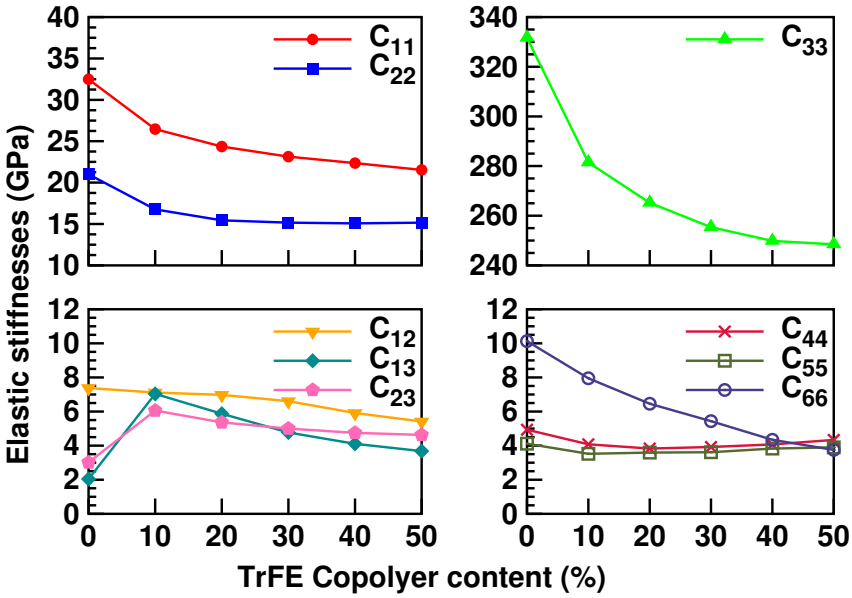

Figure 4.3.3: Elastic stiffness tensor components of the β-PVDF and poly(VDF-*co*-TrFE) crystals as functions of TrFE copolymer content.

The components of the elastic stiffness tensor for the β-PVDF crystal are presented in Table 4.3.2. The results of other known calculations are also provided for comparison and are in general agreement with our findings.[220] The dependence of the values of the elastic stiffness tensor components of

Table 4.3.2: Elastic stiffness tensor (GPa) of pure PVDF

Method	C_{11}	C_{22}	C_{33}	C_{44}	C_{55}	C_{66}	C_{12}	C_{13}	C_{23}	Ref.
EXP(10 K)	11.9	15.6	121	4.5	4.5	3.0	-	-	-	[220]
DFT	19.8	24.5	287	1.2	0.3	1.7	4.3	0.8	3.3	[200]
FF	23.2	10.6	237	2.2	4.4	6.4	-	-	-	[221]
FF	25.5	12.4	283	3.5	5.1	4.0	3.0	4.0	2.4	[201]
FF	31.0	32.9	293	-	-	-	2.9	4.7	8.5	[203]
FF	32.5	21.0	332	4.9	4.1	10.0	7.4	2.0	3.0	This Work

poly(VDF-*co*-TrFE) on composition are shown in Fig. 4.3.3. As expected, for all TrFE concentrations, the elastic stiffness component along backbone chain direction C_{33} remains about an order of magnitude larger, compared to the other two principal direction components C_{11} and C_{22}. The rest of the elastic stiffness components are an order of magnitude smaller, compared to the latter two components. Increasing the TrFE percentage results in a substantial drop in the copolymer stiffness, with the C_{11}, C_{22} and C_{33} components declining by up to 50, 30 and 25%, respectively, for the 50/50 system. This can be attributed to the disordering of the polymer crystal structure under the influence of increasing repulsive forces between and/or within the chains.[179] The experimental value of C_{33} in β-PVDF film was reported to be 177 GPa using X-ray diffraction under the assumption of homogeneous stress.[222] This is substantially lower than values of 280–330 GPa reported in this, and other computational studies.[200,201,203,220,221] This discrepancy can be explained by the fact that the type of randomness present even in large computational models of β-PVDF crystals includes only rotational disordering of the polymer chains, which still remain perfectly aligned and connected along the backbone direction. Furthermore,

with the exception of the head-to-head (HH) monomer arrangements, most other types of defects and impurities present in experimentally grown samples[221] are also usually not considered in such models. Moreover, the elastic properties measured in various PVDF samples that are prepared by different experimental approaches, would also lead to different results.[223]

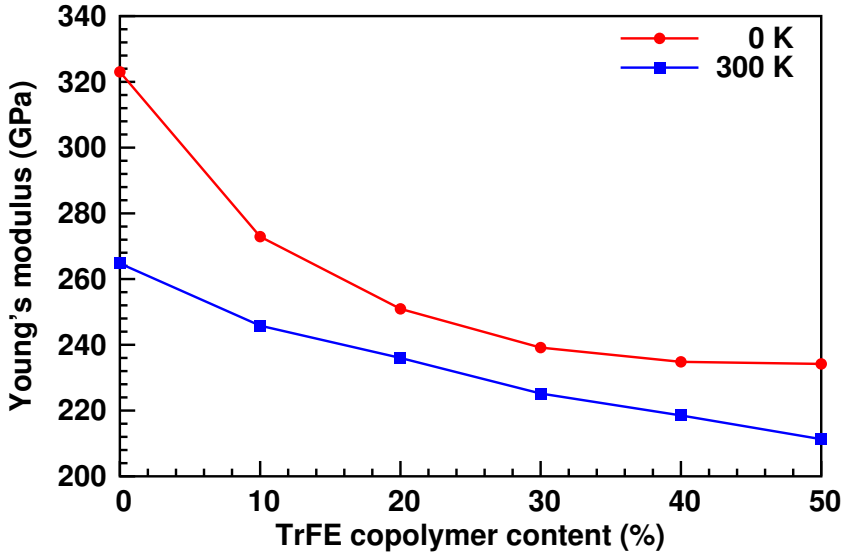

Figure 4.3.4: Young's modulus E_c along the polymer chain direction as a function of the TrFE copolymer content at 0 K and room temperature.

Fig. 4.3.4 shows the dependence of Young's modulus E_c in poly(VDF-*co*-TrFE) system at 0 K and room temperature on the TrFE concentration. Due to thermal expansion, E_c is lower at elevated temperatures. Furthermore, the presence of TrFE monomers significantly decreases the Young's modulus value. This effect is most pronounced at smaller copolymer compositions, which could be attributed to the initial rotational disordering of the polymer chains.

In terms of polar properties, Fig. 4.3.5 presents the results of our (point-

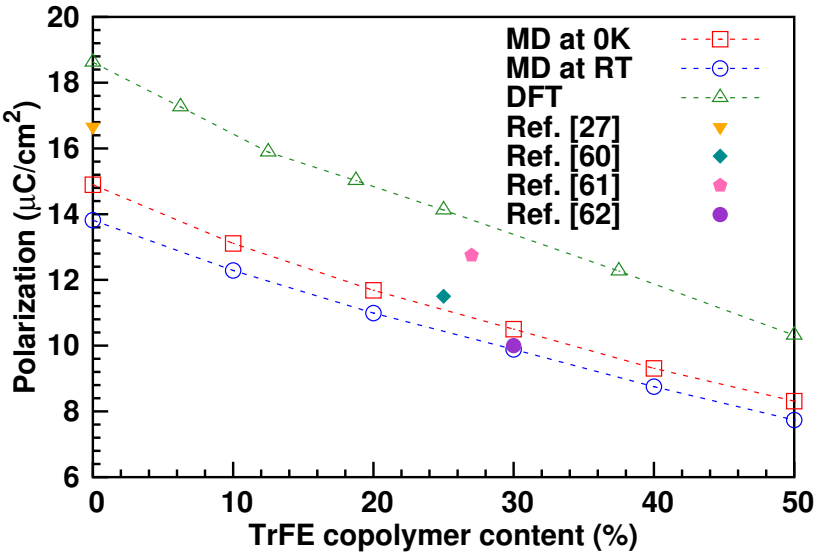

Figure 4.3.5: Polarization of the β-PVDF and poly(VDF-*co*-TrFE) crystals as a function of TrFE copolymer content at 0 K and room temperature(RT). Data from the DFT-based calculations of Ref.[1] (at 0 K) and experimental results of β-PVDF file from Ref.[2], 75-25% poly(VDF-*co*-TrFE) polycrystalline film from Ref.[3], 73-27% sample from Ref.[4], and 70-30% poly(VDF-*co*-TrFE) film from Ref.[5], are also shown for comparison.

charge based model)[221] calculations of spontaneous polarization at 0 K and room temperature as the function of TrFE concentration. Comparisons to the results of the DFT calculations[1] (at 0 K), as well as some experimental measurements for a variety of different samples are also included. Here, the FF combined with point-charge based dipole-moment computations reproduce the rate of decrease of the spontaneous polarization with increasing TrFE content, but these values are systematically underestimated vs. DFT values by as much as ~20% for the whole range of TrFE compositions. It is also noteworthy that the results of most experimental measurements assembled in Fig. 4.3.5, which are presumably made for not fully crystalline and defect-free samples,

also appear higher than the polarization values produced by this FF. At the same time, our results suggest that within the approximations of the utilized computational approach, the change in temperature from 0 to 300 K introduces only a marginal, ~7% decrease in polarization, which is mostly due to the thermal expansion of the simulation box. Therefore, the presented results demonstrate that in order to correctly simulate the polarization in such systems a successful FF parameterization (*e.g.*, such as the one introduced for PVDF in Ref.[1]) has to account for the contributions of the electronic degrees of freedom, *i.e.*, the polarization of electron clouds on the monomer under the influence of the internal electric field produced by the dipole moments of monomers around it. However, it may still be possible to obtain reasonable estimates for certain polarization-related properties that depend on polarization derivatives rather than on absolute values.

Table 4.3.3: Pyroelectric coefficient (10^{-3} μC/cm^2 K^{-1}) at room temperature

TrFE(%)	0	10	20	30	40	50
p_y^σ	-3.76	-2.89	-2.53	-2.97	-2.30	-2.50

As suggested by our further computations, the pyroelectric coefficient of β-PVDF is one of such properties. Table 4.3.3 presents the obtained values for the dependence of the room temperature pyroelectric coefficient on copolymer composition. Our result for β-PVDF compares favorably to the reported value -3.26 (10^{-3} μC/cm^2 K^{-1}) in another theoretical study[203] and -2.6~-3.5 (10^{-3} μC/cm^2

K^{-1}) from the experimental measurements.[224,225] While we predict smaller pyroelectric coefficients in psoly(VDF-*co*-TrFE) copolymer crystals, this declining trend is not monotonous, displaying a relatively large pyroelectric response in the 70/30 system.

4.4 Conclusion

Finite temperature MD simulations of the structural, elastic, polar and pyroelectric properties of ferroelectric β-PVDF and of poly(VDF-*co*-TrFE) of various compositions were carried out. A refined FF of Tashiro *et al.*[204,209] was utilized in all the calculations. Our study demonstrates that this FF reproduces the structural, pyroelectric and, in the absence of experimental data, some of the elastic characteristics of highly crystalline β-PVDF and copolymers. However, the spontaneous polarization, obtained through point-charge summation over the ionic coordinates produced by the FF, is underestimated by ~20% for all the copolymer compositions. Therefore, a further modification of this FF, *e.g.*, by augmenting it using a shell model, will be very useful for further modeling of polar, piezoelectric and electrocaloric properties of these materials. Moreover, the inclusion of HH PVDF defects, as well as that of polymer chain ends will lead to further refinement of our models.

4.5 Phase Transition of PVDF and its P(VDF-TrFE) Copolymer

In previous section, we mainly focus our discussion on ferroelectric β phase PVDF and its copolymer poly(VDF-*co*-TrFE). Encouraged by the well-behaved description of implemented force filed (FF) potential, we extend our study on dynamic behavior and compare our results with the experimental observation. There are four crystalline phases (α, β, γ, and δ) of PVDF at different external conditions. These phases mainly depend on its atomic configuration and packing orientation. Most studies are focus on the pure crystalline of non-polar α phase and of polar β phase. If phase transition occurs, the system is in order at low temperatures and disorder at high temperatures, so called order-disordered phase transition. At the following section, we would like to investigate two different type of phase transitions, one is temperature-induced, and the other is deformation-induced phase transition.

4.5.1 Introduction

It has been experimental observed that the phase transition temperature of P(VDF-TrFE) copolymer increases by increasing the VDF content.[179,226] They have observed a change in crystal lattice spacing associated with remanent strain and an anomalous specific heat. These characteristic evidence shows the observation of ferroelectric phase transition. Tanaka *et al.* have reported that "the ferroelectric transition of P(VDF-TrFE) is strictly of the first order, however, it has the second-order character especially in the copolymers with low PVDF

content. The observation of the rotation of dipole is always accompanied by cooperative conformational change of the backbone, which is unique to a polymer chain. This type of statement is well-reflected in our MD simulation of temperature-induced phase transition, which is reported in the following section. By using time domain measurement of electric displacement, the switching feature of ferroelectric PVDF was investigated. They conclude that the cooperative effects in the switching process plays an important role by applying an electric field, where the switching time increases significantly as field or temperature decreases.[227] We would also study this type of phase transition, deformation-induced type with applied electric field, and provide some discussion in the level of atomistic point of view.

4.5.2 Temperature-Induced Phase Transition

In order to better describe the interaction between atoms, the reliability of semi-empirical potential parameters is the key factor to capture the underlying mechanisms. Here again, we list all the bonded and non-bounded energy term and its schematic representations as follows

$$\begin{aligned} E_{\text{tot}} &= E_{val} + E_{nb} \\ &= E_b + E_a + E_t + E_{ab} + E_{bb} + E_{1aa} + E_{2aa} \\ &+ E_{vdWij} + E_Q \end{aligned} \tag{4.5.1}$$

where valence energy E_{val} consists of E_b (bond stretch), E_a (angle bend), E_t (torsional), E_{ab} and E_{bb} (cross terms), E_{1aa} and E_{2aa} (angle-angle terms). Non-bonded

energy E_{nb} consists of E_{vdWij} (van der Waals) and E_Q (Coulomb interactions). The 1-2 (bond) and 1-3 (angle) of Coulomb interactions are excluded because these interactions are covered in the valence energy terms. The detailed description of each energy expression can be found in the original work.[204]

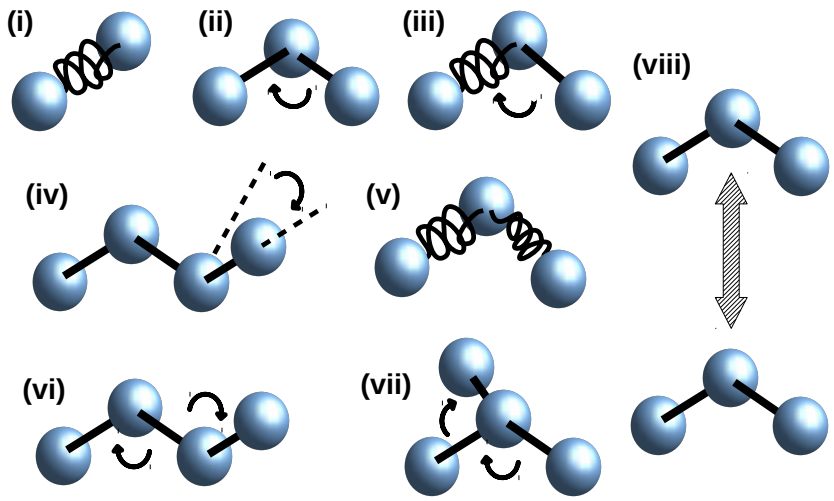

Figure 4.5.1: Each individual energy term is written as (i)E_b (bond stretch), (ii) E_a (angle bend), (iii) E_t (torsional), (iv) E_{ab} and (v) E_{bb} (cross terms), (vi) E_{1aa} and (vii) E_{2aa} (angle-angle terms). (viii) Non-bonded energy term E_{nb} consists of E_{vdWij} (van der Waals) and E_Q (Coulomb interactions). The sphere represents the carbon atom.

The tortional energy term ((iv) in Fig. 4.5.1) plays an important role in our PVDF system, and in polymeric chain, since the crystal structure highly depend on the conformational change of the backbone. In our simulation, initially we provide the uniformly distributed $\beta-$ phase PVDF. The temperature rises from theoretical 0 K, 100K, 200K up to 500K. At each desired temperature, we wait

until the system reaches its equilibrium, more specifically dynamical equilibrium, and record the desired physical quantities. More precisely, the properties were sampled for an NPT (isothermal-isobaric) ensemble. The result shows the different phase transition behaviors of copolymer with different TrFE content. Since we are interested in the polarization change with respect to the temperature. The same rigid-bond approximation is applied to calculate the dipole moment, and the corresponding polarization. It is worthy to mention again that even though replacing one hydrogen atom by fluorite decreases the electric dipole moment unit in each monomer, a larger steric hindrance of TrFE unit assists the stability of the ferroelectric polymer chain. More importantly, the P(VDF-*co*-TrFE) shows the Curie temperature below the melting temperature, which isn't the case for pure PVDF. In this way, one would be able to study the ferroelectric (FE) to paraelectric (PE) phase transition, before melting happens. The trans-to-gauche conformational change was done with large thermal rotation of the chains, resulting in the extinction of the electric polarization of the whole unit cell in the high-temperature phase.

The ferroelectric $\beta-$phase PVDF is shown in Fig. 4.5.2(a1). In Fig. 4.5.2(b1), the arrow indicated the direction of the electric dipole moment due to the contribution from the electronegative fluorine. It can be easily recognized from Fig. 4.5.3, the corresponding polarization decreases while increasing the TrFE content at same temperature. Below the Curie temperature, polarization of pure PVDF and its P(VDF-*co*-TrFE) decrease while temperature increases. It

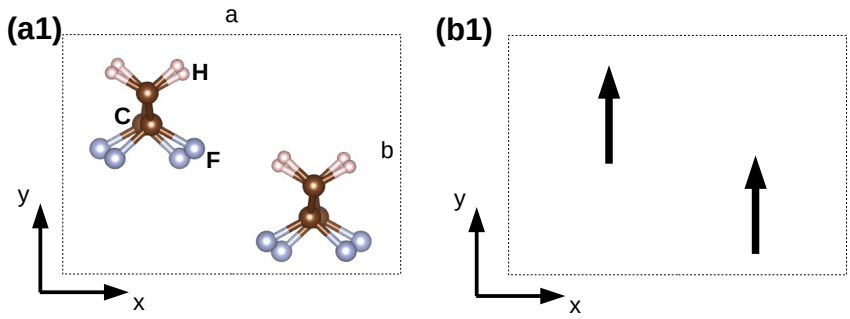

Figure 4.5.2: (a1) The crystal sturcture of $\beta-$phase PVDF (b1) the arrow representation of the electric dipole moment. a and b are the lattice parameters. $c-$axis is the direction of backbone chain, which points out of the plane.

is due to the combination of thermal fluctuation and thermal expansion. We note that the change in volume mainly because of the expansion in $a-b$ plane. The stronger carbon-carbon bond holds the chain rigidly in backbone direction, comparing to the non-bonded interaction between each polymer chain. While temperature keeps increasing, the transition gradually appears on low content VDF structure, but not for the cases with higher content of VDF unit. This observation is consistent with the experimental measurement.[228]

4.5.3 Deformation-Induced Phase Transition

As we mentioned earlier, the polymorphs of PVDF (α (form II),[186] β (form I),[186] γ (form III)[187] and δ (form VI).) is determined by the conformation and molecular packing. The non-polar α and polar δ, both α and δ forms include TGTG' (trans-gauche-trans-gauche) chain conformations, only differ by the orderings of the monomer dipole moments. PVDF polymorphs can be produced by a number of different processing techniques,[167] *e.g.*, the α phase can be readily synthesized by melt crystallization, while the β phase is normally obtained

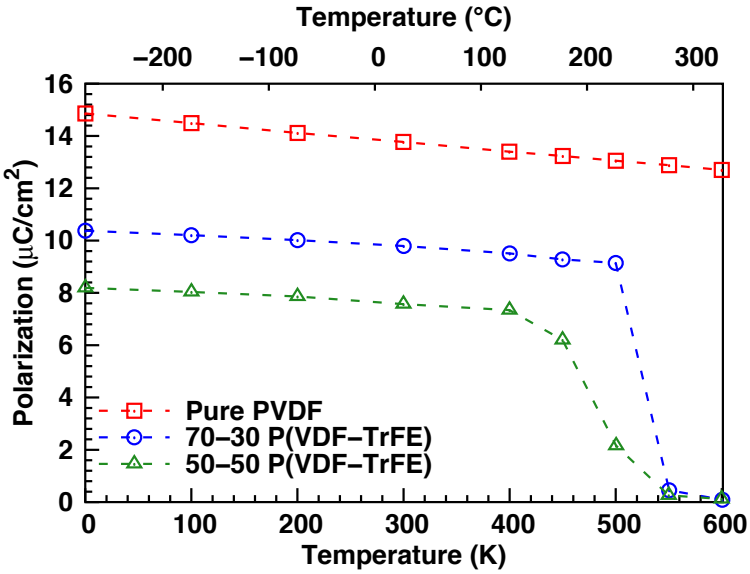

Figure 4.5.3: Temperature-induced phase transition of PVDF and its P(VDF-*co*-TrFE) The first-order and second-order like phase transitions are observed with different composition of polymer units.

by the combination of mechanical stretching[189] and electrical poling[190] of α-crystalline PVDF. Such approach to obtain the film with ferroelectric phase involves the deformation of the materials. It has been shown that the uniaxial plastic deformation induces the macroscopically polarization by turning the spherulitic structure into an array of crystallites. The re-orientation of the molecular is achieved by this external stimuli to increase the aligning order of each dipole moment from individual monomer.

In Fig. 4.5.4, we demonstrate the more realistic representation of (a) $\alpha-$phase and (b) $\beta-$phase PVDF related copolymer chain. We note that it might have the effect from abnormal linkages to the stability of a polymer chain, for instance,

20 % of head-to-head tail-to-tail (HHTT) linkage of polymer chain, the energy of the all-trains (TTTT) conformation is lower by about 5 kcal mol^{-1} than that of TGTG' (trans-gauche-trans-gauche) chain conformations.[229] Here in our simulations, we ignore this effect for simplicity, especially the consideration of abnormal linkage might have to be included while the force field potential is parameterized.

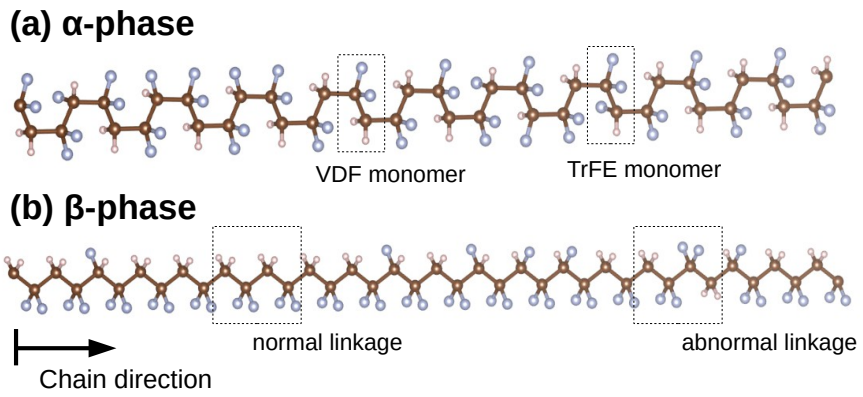

Figure 4.5.4: a) $\alpha-$phase, and (b) $\beta-$phase model representation of P(VDF-*co*-TrFE). The VDF and TrFE monomer are separately indicated. Normal linkage and abnormal linkage are shown, represent head-to-head (HH) and head-to-tail (HT) monomer arrangement, respectively. Hydrogen (H) and carbon (C) atoms are represented by small ivory and medium-sized brown spheres, respectively. Fluorine (F) atoms are represented by large blue spheres.

As one can imagine, the processing condition can change the morphology in a very different way by viewing the phase content of PVDF. When an $\alpha-$phase sample is subjected to a stretching and a poling process (the most usual way of achieving poles $\beta-$PVDF samples ready for application) the stretching is responsible for the main α to β conversion and the poling is responsible for the reorientation of the dipolar moments along the electric field, together with

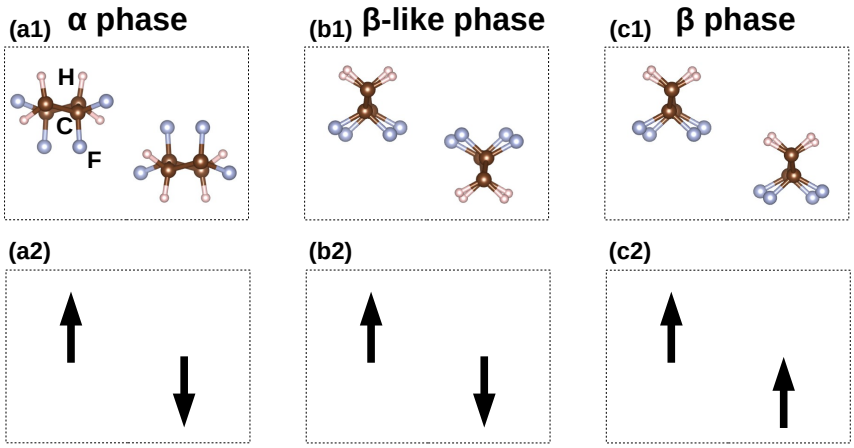

Figure 4.5.5: (a)α, (b)$\beta-$like, and (c)β phase of PVDF unit, viewing in the backbond direction. The path of transformation from (a) to (b) is associated with deformation-induced transition only. Arrow indicates the direction of dipole moment within the crystal unit cell.

some minor structural rearrangements. Here in our simulations, we have observed two different type of transformation, namely, (i) α to $\beta-$like (Fig. 4.5.5), and (ii) α to δ to β (Fig. 4.5.6) type deformation and electric-field-induced phase transition. The initial structure is prepared as uniformly crystalized $\alpha-$ phase and total energy is minimized before NPT (isothermal-isobaric ensemble) is applied. The sampling at constant pressure and constant temperature is well-reflected the common reaction environment. As the standard procedure of molecular dynamics simulations, the physical quantities were determined by the reasonable recording time period. The inadequate recording time might cause the results being not representative enough for the system at certain circumstances. The thermostatting and barostatting is achieved, where thermostatting is by adding dynamic variables coupled to the particle velocities

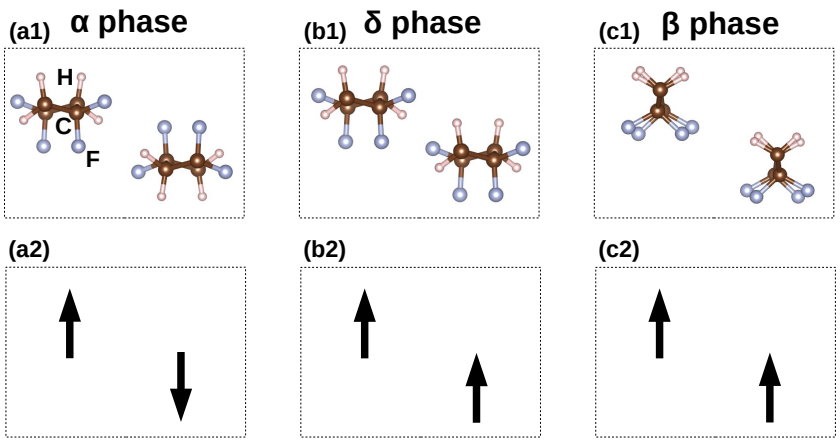

Figure 4.5.6: (a)α, (b)δ, and (c)β phase of PVDF unit, viewing in the backbond direction. The path of transformation from (a) to (b) then (c) is associated with deformation-induced and electric-field-induced phase transition. Arrow indicates the direction of dipole moment within the crystal unit cell.

and barostatting is by adding dynamic variables coupled to the simulation domain dimensions, as described in the LAMMPS package. The temperature and pressure, obtained through the time-averaged quantities, is recorded and set to the desired value. The Nose-Hoover thermostat, by fixing the average temperature of the system, but allowing for temperature fluctuation with a canonical distribution. We have shown that the simulation box size of 27Å $\times$ 30Å $\times$ 52Å ($\sim 3a \times 6b \times 20c$), *i.e.*, a arrangement of polymer chains each containing 20 monomers (720 monomers, 4320 atoms total), was found to be sufficiently large, *i.e.*, the change of the unit-cell lattice parameters upon further enlargement of the simulation box was below 0.1%. The size of simulation box remains the same as before and we proceed to the phase transition study. The simulation from low to high temperature with 100 K increment runs for 100

picoseconds (100K steps). The atomic coordinates are recorded to calculate the dipole moment. Without applying electric field, α to $\beta-$like phase transition occurs but still remain as ferroelectric due to net dipole moment remains zero. However, by applying electric field, we visualize the α to δ to β type transformation. (Fig. 4.5.7)

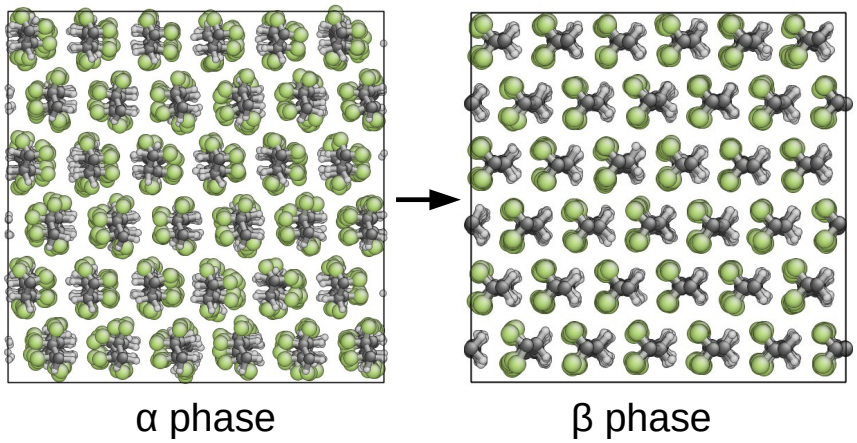

Figure 4.5.7: The simulation box of initial(α) and final(β) phase.

Moreover, the dynamical behavior can be recorded step-wisely while we perform the MD simulations. The intermediate phase, for this case δ phase, can be easily captured and further visualized. In Fig. 4.5.8, we show the number (ratio) of the dihedral angle showing between all of the carbon-carbon bond, indicating the TGTG' to TTTT type, or α to β type phase transition.

Lastly, we list few recent experimental papers which talk about phase transformation in a more general perspective, as long as the discussion of processing and application. The main characteristics of the electroactive phases of PVDF and copolymers have been reviewed, the experimental techniques to

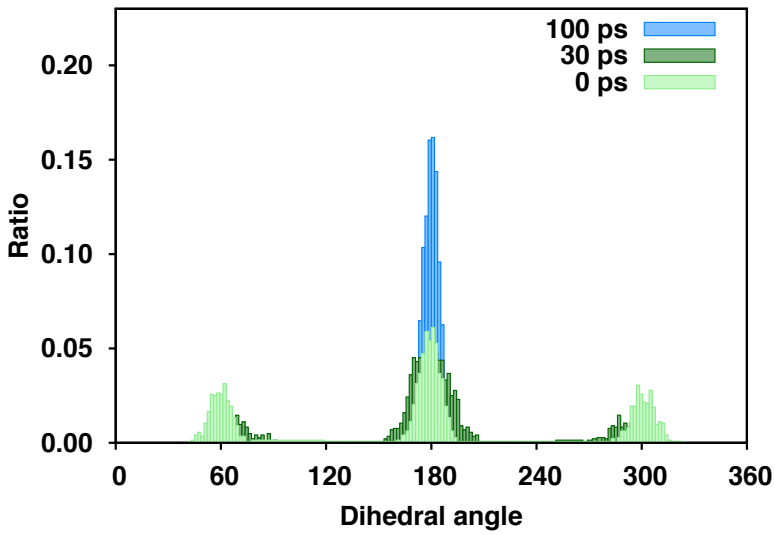

Figure 4.5.8: The number of counting from dihedral angle at different simulation time, where ps stands for picoseconds. It is the indication of α to β type phase transition.

identify them in a proper way, as well as the different processing strategies to achieve the desired materials characteristics.[174] The transformation from $\alpha-$crystal to $\beta-$crystal of PVDF membrane that carried out under the conditions of the different stretching temperature, stretching rate and tensile elongation was studied.[230] The stretched films were tested by FTIR and XRD to analyze quantitatively the transformation from $\alpha-$crystal to $\beta-$crystal. The results indicated that low temperature was conductive to the formation of $\beta-$crystal and the tensile temperature around 100 $^{\circ}C$ is suitable for the transformation under stretching processing. With the increase of the tensile elongation, the relative crystallinity would also increase and achieve the highest above λ(stretching

rate in the stress microscope) of 3. The stretching rate has less effect on the transformation from $\alpha-$crystal to $\beta-$crystal.

4.6 Conclusion

The molecular dynamics with FF potential was exploited to study the dynamic behavior of poly(VDF-*co*-TrFE) system, which essentially is the experimentally observed ferroelectric-to-paraelectric and deformation-induced phase transition. The temperature-induced phase transition reveals the behavior of order-disorder type phase transition. On the other hand, deformation-induced phase transition provides the evidence that the external electric field is essential to trigger this type of transformation. Since the implemented MD simulations with force field parameters have shown the capability of reproducing static physics quantities and dynamic physical behavior, this formalism might be applied to the system with higher complexity.

Chapter 5

First-Principles Calculations of Ferroelectric Bismuth Titanate

5.1 Introduction

Ferroelectric $Bi_4Ti_3O_{12}$ (BiT), belongs to Aurivillius phases, has attracted great interests in recent years. The ferroelectric properties have been realized back in 60s', but the growing interest starts very recently, especially for the thin film nonvolatile memory device. In order to reach as much of remanent polarization as possible, $PbZr_xTi_{1-x}O_3$ (PZT) thin films with various compositions becomes most promising and have been studied intensively. However, the severe disadvantage of PZT is that fatigue appears after cycles. The two characteristics of BiT, which is considered as a promising materials for electronic device, are the large spontaneous polarization P $\sim$ 50 μC/cm^2 at room temperature and the low band gap E_g $\sim$ 3 eV.[231] However, the direction of the polarization in the pure BiT is not in the same as the epitaxial film growing axis. In order to obtain the switchable polarization along such axis, Roy *et. al.* has reported the effect from the rare earth element doping on Bi-site[232] and the epitaxial strain. However, they concluded that large out-of-plane po-

larization wasn't feasible by epitaxial strain and by doping, 1.34 $\mu C/cm^2$ in bismuth lanthanum titanate (BLaT) and 2.95 $\mu C/cm^2$ in bismuth Neodymium titanate (BNdT). Shah *et. al.* has investigated the effect of oxygen vacancy on the ferroelectric fatigue properties of pure and La-doped BiT. They concluded that doping with lanthanum can increase the formation energy of oxygen vacancy, and can therefore prevent the oxygen segregation and diffusion at the domain walls, which is believed to influence the polarization switching and cause fatigue.[233] Very importantly, the fatigue free behavior of the Aurivillius layered structure is likely due to the crystal geometry, where Bi_2O_2 layer is considered as the insulting layer to compensate the space charge. It has been reported that the acoustic anomalies in Heusler alloys might be driven by the low-energy optical vibration.[234] The optical frequency appears to be lower at unstable phase, comparing to the stable one. The vibrational frequency, therefore the structrual stability, is related to the interaction between the acoustic and optical mode. Nowadays, the healthy and environmental concern have been addressed seriously so that lead-free materials attract more attention than ever. $SrBi_2Ta_2O_9$ (SBT), a two perovskite-like layered structure, is one of the strong candidate replacing the conventional PZT for ferroelectric raondom access memories (FeRAMs). However, high processing temperature, around 750 $^\circ C$, is required for SBT, which might hinder the developement of the silicon device. Therefore, the substituted forms of BiT have a great potential for the electronic application,[235,236] particularly for multiferroics,[237,238] non-volitile

ferroelectric memories,[239] low-fatigue lead-free ferroelectric,[240] photoelectronic devices,[241] and photocatalysts.[242]

5.2 Crystal Symmetry

The formula of aurivillius phase can be expressed as $Bi_2A_{n-1}B_nO_{3n+3}$, where Bi_2O_2 represents the flourite-like layer, $A_{n-1}B_nO_{3n+1}$ represents the fluorite-like layer, and n represents the number of BO_6 octahedra within the perovskite unit [Fig. 5.2.1]. Due to the subtle differences of the complex Aurivillius crystal structure, the low temperature phase of BiT have created lots of confusion between the reported literatures. General speaking, x-ray diffraction, where the technique highly depends on atomic mass, is commonly used to analyze crystal structure. In our BiT system, the signal is more sensitive to the most heaviest bismuth atom. The lack of information from lighter species in weight might give different crystal structure due to the limitation of the experimental apparatus. In order to better describe, for instance the coordinates of the oxygen atom, the neutron diffraction can be considered to analyze the structure in metal oxide, where the technique depends on the nuclear scattering length of the atoms. Oh *et al.*[243] have synthesized $Bi_{4-x}La_xTi_3O_{12}$ (x = 0, 0.25, 0.5, 0.75) through standard solid-state reactions and characterized by power x-ray and neutron diffractions. They have reported the materials crystallizes in the orthorhombic space group *B*2*cb* (Number 41), where angles between lattice parameters remain 90°. Kim *et al.*[244] have studied the direct observation of

oxygen stabilization in $Bi_{3.25}La_{0.75}Ti_3O_{12}$, where the analyze is done by the $B2cb$ structure. On the other hand, Rae *et al.* have suggested a monoclinic $B1a1$ (or $P1c1$ in space group Number 7 as a non-standard form)[245] as for the low temperature phase of ferroelectric BiT. By using neutron power diffraction and Rietveld analysis based method, the crystal structure of low temperature BiT has been determined as the monoclinic space group of $B1a1$, where lattice parameters a = 5.44 Å, b = 5.41 Å, c = 32.81 Å, and β = 89.99°.[246] Later, the crystal structure of $Bi_4Ti_3O_{12}$ (BiT) at low temperature is monoclinic (space group $B1a1$), which has been confirmed through group-subgroup instability study.[247]

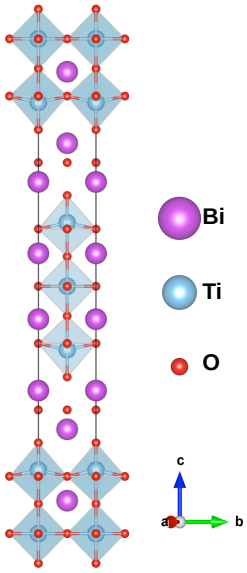

Figure 5.2.1: Schematic representation of high temperature phase (I4/mmm) of bismuth titanate. Bismuth, titanium, and oxygen atoms are represented as purple, water blue and red spheres, respectively. TiO_6 octahedra is considered for visualizing the corresponding distortion.

5.3 Solid Solutions

As a potential candidate for the functional materials, the various physical properties are strongly desirable by improving the performance or enhance the functionality. Even though it is an ongoing research topic with great challenge, one of the standard approach is to introduce different type of elements into the system. To be more specifically, fatigue is the most common defect of pure BiT materials to be observed, as the number of switching cycles increases. In order to taking care of this situation, A-site of the perovskite-like layers substitution has been investigated extensively in ferroelectric bismuth titanate. The improved fatigue phenomena in the La-substituted BiT attracts great interest after being experimentally observed.[239,248] Park *et al.* have reported the fatigue-free films on metal electrodes, in a relatively lower deposition temperature $\sim 650\,^{\circ}C$, and a relatively higher remnant polarization around 20 $\mu C/cm^2$. This idea was initiated from the strontium bismuth tantalate, or $SrBi_2Ta_2O_9$ (SBT), which also belongs to Aurivillius phase. It has been found that the Bi_2O_2 layer is responsible for overcoming the fatigue problem by compensating the free charge within the layer. However, oxygen vacancy also plays a role to determine the fatigue behavior. Using x-ray photoemission spectroscopy, the defects can be analyzed such that the oxygen vacancies[249,250] is identified being only near the Bi_2O_2 layer for SBT, but all through out the sample of BiT. Therefore, both the existence of Bi_2O_2 layer[251] and the geometrical configura-

tion of the oxygen vacancies should be both taken into account as a screening factor for finding the new materials as the potential candidate of non-volatile memories device. By varying the composition of La, or other species, might be considered as a nob to fine tuning the desired electrical properties.[252] For BiT, or $(Bi_2O_2)^2(A_{n-1}B_nO_{3n+1})^{2-}$, the potential A-site substitution could be monovalent, divalent, or trivalent cations, such as Sr, Ca, or Ba.[253] Moreover, other techniques, such as doping (B-site) and epitaxial strain engineering, could be useful for manipulating the complex oxide, and suggest the suitable configuration yielding desirable polarization[232] and other properties.

5.4 Modern theory of polarization

In order to determine the polarization of the crystal structure, one needs to have a formalism to compute the electric dipole moment within the periodic boundary condition. The difficult has hindered and the discussion has been raised that whether the polarization should be considered as intrinsic properties in bulk. The breakthrough has been realized once the researchers found that one should work with changes in polarization, but rather the absolute value.[254] Later on, the modern theory of polarization comes to rescue that one should view the polarization in the crystal structure as a lattice but a vector.[255,256] For instance, if we consider a one-dimensional periodically repeated system, where having alternating anions and cations in a row. The electric dipole moment (or polarization) can be differ while the unit cell is selected differently. However,

there is a certain pattern showing in the collection values, and the series of polarization are called polarization lattice. If one moves one anion to the right, outside from the unit cell, due to the periodicity of the lattice, one anion from the left of the unit cell will appear to fill into the empty spot. Without making the mark, one could not even observed the difference after the displacement. In other word, there has been no change in the physics. However, the computed polarization with such displacement of the atom will be changed by the integer value. We then call the integer value of the change in polarization as polarization quantum, or P_q.[257] Even though the computed absolute value of polarization in a periodic system can be infinite number of possibilities, there is only one value can be observed from the measurement. One have to plot the polarization of the centrosymmetric, where it is considered as a reference phase that no displacement is made in the lattice, and the polarization of the system with displacing atoms as a ferroelectric state. Practically, it is also important to compute the polarization of the intermediate states to estimate the correct spontaneous polarization.[258]

5.4.1 Phase Transition of $Bi_4Ti_3O_{12}$

As described in previous section, it is well-established that the space group of the high and low temperature phases of $Bi_4Ti_3O_{12}$ are I4/mmm and B1a1, respectively.[259–261] In Fig. 5.4.1, we show that the ferroelectric (monoclinic) to paraelectric (tetragonal) phase transition of BiT happens around 675 $^{\circ}C$.[262] By

visualizing the change in crystal structure, one can observe that the displacement of the atoms is rather subtle, especially in the easy axis ($c-$axis). The major difference in crystal structure is dominated by the distortion of the TiO_6 octahedra, where provides the net electric dipole moment in $a-b$ plane. However, we note that the two end member phases are not directly transform from one to another, neither through experimental observation,[259] nor from theoretical group-subgroup analysis.[247] The intermediate phase should be responsible of linking one phase to another.

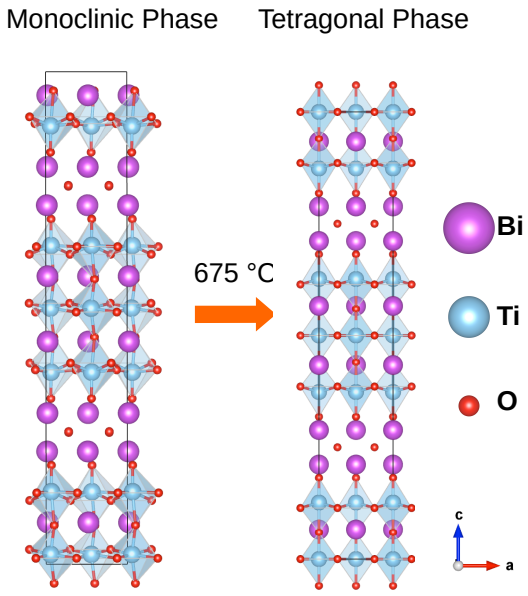

Figure 5.4.1: Schematic representation of low temperature ($B1a1$) and high temperature phase (I4/mmm) of bismuth titanate. Here, 76 atoms model are considered in both phases, in order to demonstrate the displacement of atoms, showing the corresponding change in geometry. The major polarization is attributed from the perovskite-like layer, for the distortion of TiO_6 octahedra.

5.4.2 Spontaneous polarization

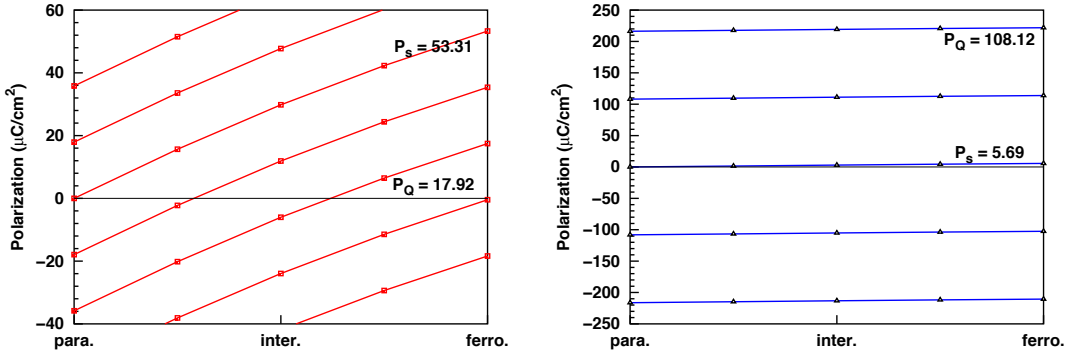

(a) Polarization along $a-axis$ (b) Polarization along $c-axis$

Figure 5.4.2: Polarization along (a) $a-axis$ and (b) $c-axis$ using modern theory of polarization. P_s and P_Q represent the spontaneous polarization and polarization quantum, respectively. The para., inter. and ferro. indicate in x-axis represent paraelectric, intermediate, and ferroelectric phases, respectively.

Here, we implement the idea of modern theory of polarization, which has been introduced in Sec. 5.4. First, we construct the ferroelectric B1a1 phase and the paraelectric I4/mmm phase. The spontaneous polarization can be computed using

$$P_s = P_f - P_p + n|P_Q|,$$

where P_s represents the spontaneous polarization, P_f represents polarization of ferroelectric phase, P_p represents polarization of paraelectric phase, P_Q represents polarization quantum, and n is an integer. $P_q = 2e\mathbf{R}/\Omega$ is determined by the shortest lattice vector $\mathbf{R}$ along the polarization direction and Ω is the volume of the cell.[263] Practically, the two end member phases should be fully relaxed with the restriction that the crystal structure remains at the same space

group. Once the structural relaxation is achieved, the intermediate phases are constructed by displacing the atoms from the paraelectric end phase to the ferroelectric end phase, which is illustrated in Fig. 5.4.2. The connection between each phases should be taken care with caution, since the polarization quantum is in the same order magnitude as the spontaneous polarization (especially along a−asix). The polarization quanta along a−asix and c−asix are deduced as 17.92 $\mu C/cm^2$ and 108.12 $\mu C/cm^2$, respectively. The order of magnitude is about 5 times larger along c−asix, which can be realized as lattice parameters c ~ 32.8 Å is larger than a ~ 5.4 Å. The polarization along a−asix is deduced as 53.31 $\mu C/cm^2$, where the polarization along c−asix is deduced as 5.69 $\mu C/cm^2$. The majority of polarization is attributed to the in-plane (a−b) component, which was dominated by the large TiO_6 structural distortions. For ferroelectric BiT, there are two different type of locations where oxygen vacancy might accumulate, one is within fluorite-like layer, and the other is perovskite-like layer. Through the ground-state energy calculations, we note that the oxygen vacancy formation energies of BiT is most likely to exist within Bi_2O_2 layer, which has a rather small effect on the polarization, especially it is well-believed that the ferroelectricity is dominated by the perovskite layers. The observation is along the same line as the study on similar aurivillius $SrBi_2Ta_2O_9$ crystal structure.[264] The atom relaxation is mainly observed and concentrated on the Bi_2O_2 region, not only polarization but also structural orientation remains unaltered significantly from the perfect crystal.[250] Furthermore, the consideration of

	x = 0	x = 0.25	x = 0.5	x = 0.56
$P_x(\mu C/cm^2)$	53.31	48.53	43.65	41[268]
$P_z(\mu C/cm^2)$	5.69	5.20	3.57	-

Table 5.4.4: The polarization of Lanthanum-doped BiT, $Bi_{4-x}La_xTi_3O_{12}$ where $x = 0,\ 0.25,$ and 0.5, is computed through modern theory of polarization. The experimental measurement of x = 0.56 is provided as comparison.[268]

Lanthanum-doped bismuth titanate were studied from the early 60's for the ferroelectric and optoelectronic devices,[265,266] 00's for ferroelectric random-access memory (FeRAM),[239] until very recently for wide bandgap optoelectronic and energy applications.[267] The polarization of La-doped $Bi_4Ti_3O_{12}$ ($Bi_{4-x}La_xTi_3O_{12}$) with $x = 0,\ 0.25,$ and 0.5 were computed through Berry phase method and the results are listed in Table 5.4.4, which are consistent with experimental results.[268]

5.5 Electronic Band Structure of BiT

Differ to the interest of ferroelectric properties on BiT materials, the band gap $E_g \sim 3.6$ eV,[245] which is in the visible spectrum region, also open up the opportunity for the application on optoelectronic properties. The dielectric and optical properties of BiT therefore becomes the targeting research topic, in order to achieve wide band gap tunability in such the layered oxide. The experimental and theoretical effort were made simultaneously and hence enrich the potential candidate pool. For instance, optical properties of ferroelectric BiT was reported based on spectroscopic ellipsometry and calculation, where

E_g ~ 2.9 eV.[269] Alloying of BiT-$LaCoO_3$ showed the band gap reduction by ~ 1 eV, which were suggested being a promising material for highly efficient opto-electronic devices.[270] Iron-doped BiT was reported that BLFT (Fe-doped lanthanum-modified BiT) epitaxial thin-films prepared by RF sputtering for the band-gap narrowing is sensitive to the deposition temperature.[271,272]

5.5.1 Computational Details

First-principles calculations were performed using Vienna *Ab initio* Simulation Package (VASP).[273] Projector-augmented-wave (PAW) potentials were used for the treatment of the core electrons. Within the general gradient approximation (GGA), the electron exchange correlation interaction were computed using the Perdew−Burke−Ernzefhof (PBE) functional.[19] Energy cutoff = 500 eV was adopted in the calculations, and Γ centered $6\times6\times2$ k-point sampling is utilized in the Monkhorst−Pack scheme.[274] The equilibrium geometries were obtained by fully optimizing the atomic position until reaching the desired tolerance 0.01 eV $Å^{-1}$. Since the band gap is always underestimated through both LDA and GGA functional,[275] the HSE06[276,277] functional methods is also considered to overcome the deficiency of the exchange−correlation in DFT scheme. Because of the computational demanding on the hybrid functionals, the k-point sampling is down scaled to Γ centered $4\times4\times2$ in the Monkhorst−Pack scheme. The electronic band structure calculations and optical properties were reported using GGA and HSE functional.

5.5.2 Results and Discussion

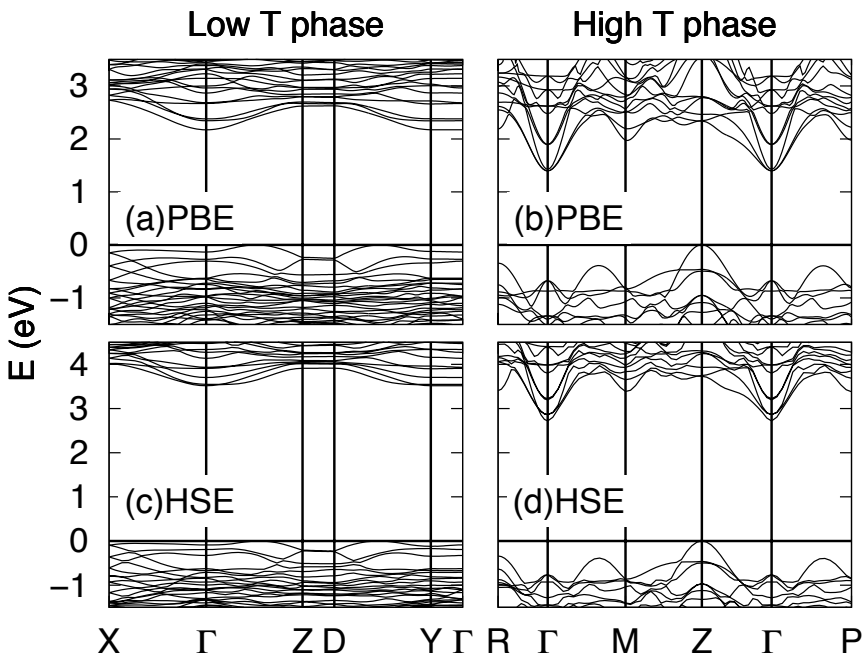

Figure 5.5.1: The band structure of (a), (c) low temperature ($B1a1$), and (b), (d) of high temperature phase (I4/mmm) of bismuth titanate. The fermi level is set to 0 eV.

The electronic band structure of low temperature and high temperature phase calculated by GGA and HSE06 functional were shown in Fig. 5.5.1. The computed indirect band gap is 2.16 eV and 1.37 eV, for low temperature and high temperature phase using GGA functional, respectively. On the other hand, the more accurate band gap value is obtained as 3.52 eV at low temperature phase using HSE06 functional. Since the dielectric function plays an important role of connecting the understanding between the microscopic structure of materials and macroscopic physical quantities, the ”better” description of band structure calculations becomes the essential factor to predict the optical

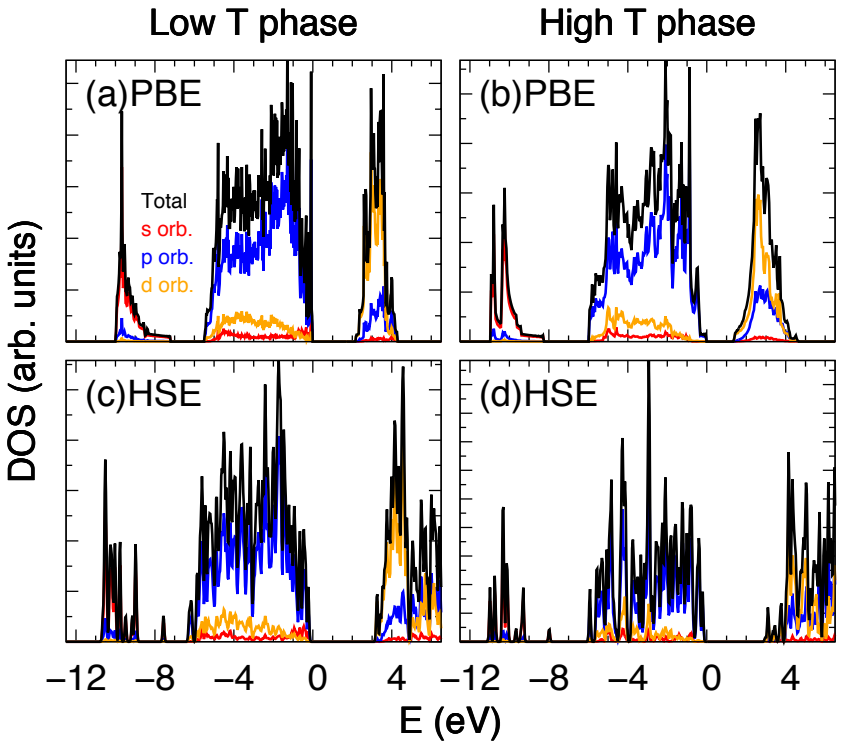

Figure 5.5.2: First-principles calculations density of states (DOS), where s, p, d, and total orbital contribution were indicted using red, blue, orange, and black in color, respectively.

related properties. However such properties are associated with the excited states, where the concept is very different to the standard ground state energy first-principle method. The computed band gap therefore highly depends on exchange and correlation term. It is well known that local density functional (LDA) or generalized gradient approximation (GGA) doesn't provide satisfied band gap value due to the limitation of its functional. HSE06,[276,278] the hybrid functional with partial Hartree-Fock screening, has been applied in various materials showing the reliable band gap. The drawback of most of the hybrid functional is the demanding computational cost. It might take 10 times longer

or more to compute while every setting remains the same but the applied functionals. This critical decision of accuracy or computational cost sustains to the researchers, depending on their questions in hand.

For low and high temperature phase of BiT, all the conduction band minimum (CBM) are located at Γ point. Within HSE functionals scheme, the valence band maximum (VBM) is located between high symmetry Γ and Z point, and Z point, for low temperature and high temperature phase, respectively. The electronic density of states (DOS) are reported here that indicating the characteristic feature of ferroelectric oxide. The covalent interaction, which originates from the hybridization between titanium 3d and oxygen 2p orbitals, plays an important role of the ferroelectric stability. We note that the chemical stability of oxygen ions in the perovskite-like layer are associated with the fatigue and reduction of leakage current density.[239] Subsequent calculations of optical constants such as dielectric permittivity, refractive index (n), absorption coefficient (α), and conductivity are shown in Figs. 5.5.3 and 5.5.4, respectively. The different optical behavior along in-plane (x-,y-axis) and out-of-plane (z-axis) show the optical anisotropy in BiT, and our calculations are consistent with the experimental measurement.[279] For instance, dielectric permittivity as a functional of photon energy is used to identify the band gap. It is determined by the intersection of x-axis and the extended linear fitting line of the slope where the imaginary part of dielectric permittivity begins to response. Fig. 5.5.3 (a) and (c) indicate the band gap difference is more than 1 eV by PBE and HSE

functionals at low temperature phase of BiT. The behavior is very similar for high temperature phase of BiT, showing in Fig. 5.5.3 (b) and (d). The refractive index using PBE and HSE at low and high temperature phase are shown in Figs. 5.5.3, where its indices are in the range of 0 to 4 while photon energy is less than 6 eV. Absorption coefficient and conductivity are indicates in Figs. 5.5.4 using PBE and HSE functionals. As what we have addressed above, the behavior are very similar between two functionals as a function of phonon energy. The most noticeable change is the right shift with around 1 eV from PBE to HSE plots. We note that for BiT, the advanced hybrid screening functional, for our case (HSE) is unforbidenly required to obtain the more accurate optical properties, where accurate is referring to experimental measurements. However, if the exact value of band gap or optical property isn't but the tendency of the behavior is the point of interest, one might consider using the standard PBE functional to obtain the rough picture of its optical responses. From my experience of BiT system, it saves about 10 times computational time.

5.6 Conclusion

The electronic structure of bismuth titanate are performed using first-principles calculations at low and high temperature with standard PBE and hybrid HSE06 functionals. There is an indirect band gap of 2.16 and 3.52 eV using PBE and HSE06, respectively. We also compute the spontaneous polarization by modern theory of polarization, showing the large polarization

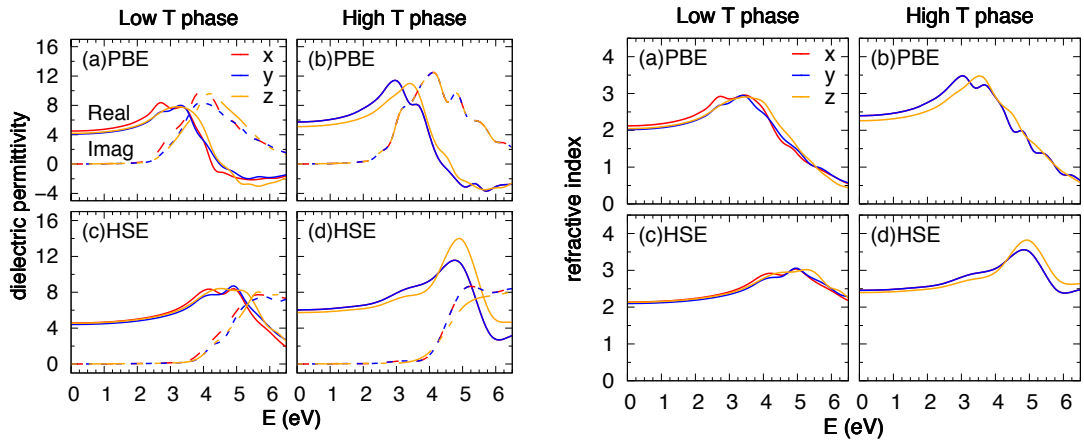

(a) Dielectric permittivity (b) Refractive index

Figure 5.5.3: Optical properties of low and high T phase of (a) dielectric permittivity, and (b) refractive index as a function of incident photon energy of BiT are calculated using PBE and HSE functionals.These physical quantities are experimentally used to evaluate the band gap.

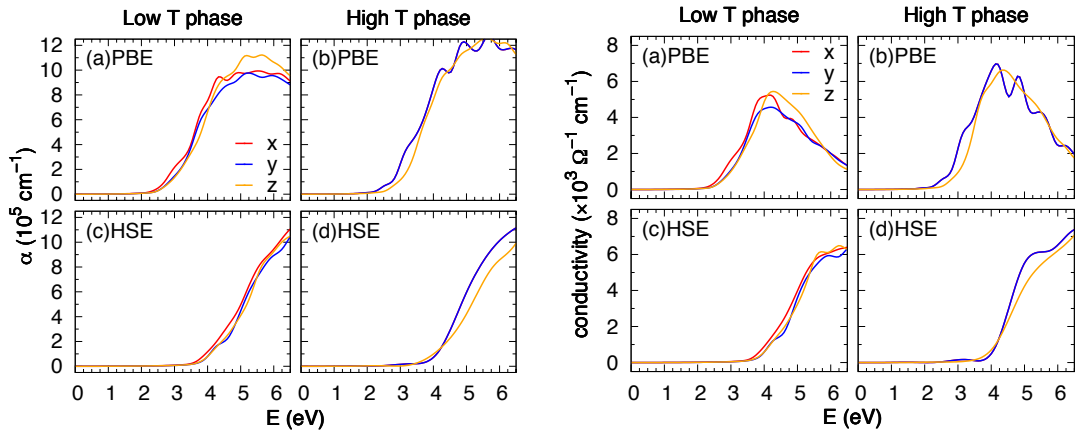

(a) Absorption coefficient (b) Conductivity

Figure 5.5.4: Optical properties of low and high T phase of (a) absorption coefficient, and (b) conductivity as a function of incident photon energy of BiT are calculated using PBE and HSE functionals. These physical quantities are experimentally used to evaluate the band gap.

$\sim$ 53.31 $\mu C/cm^2$ is in the direction perpendicular to the film growing z-axis. The magnitude of polarization is one order smaller along z-axis, indicating a large anisotropy. Dielectric function, refractive index, absorption coefficient, and conductivity are also reported. The behavior of optical properties as a function of incident photon energy remains similar, with the right shift about 1 eV by using PBE and HSE06 functionals due to the exchange and correlation energy term. The stability of bismuth titanate, or even other Aurivillius phase, would play the major role for the opto-electric devices. The first-principles approach can further applied to other complex oxides materials, including but not limited to doping and alloying materials, to investigate its microscopic structure and macroscopic behavior at fundamental level.

Chapter 6

Summary and Future Work

Significant advances have been made in the past few decades with accurate experimental measurements being achieved and computational resources becoming more feasible. New techniques have been developed to progress fundamental understanding and powerful computing. In previous chapters specific systems were examined to understand particular phenomena in those confined regions. Now, the works will be summarized and suggestions for further works will be provided. Brief literature reviews will also be discussed to provide the scopes in more general perspectives.

6.1 Summary

In this Thesis, various computational approaches including nonlinear thermodynamics model, classical molecular dynamics simulations, and first-principle calculations were considered to investigate the structural-property relations of organic and inorganic ferroelectric materials in different time and length scales. Landau-based thermodynamics method is used to study the piezoelectric behavior of epitaxial (001) strontium titanate films by considering the electromechnical coupling between the polarization and the in-plane lat-

tice mismatch. The strain engineering approach has been utilized to provide the possible stimuli and to tailor the material to desired behavior for sensor, actuators, and surface acoustic wave applications. Moreover, such method can provide new insight for reducing the cost in communications, radar, and wireless data application prior to design and fabrication.

The classical molecular dynamics simulations were utilized to investigate the properties of crystalline ferroelectric β phase poly(vinylidene fluoride), PVDF, and its P(VDF-*co*-TrFE) copolymer. The structural, elastic, and polar properties were obtained through thermodynamic ensembling. Furthermore, the evolution trajectory was recorded to analyze the intermediate phase where phase transformation occurs. For instance, the computational results of deformation-induced phase transitions of PVDF reveal the existence of an intermediate phase, which might not be so perceptive in an experimental setting. With such evidence, modeling can be useful to provide the systematic study at atomistic level.

Finally, the quantum-mechanical based density functional theory was used to study a complex, ferroelectric layered oxide. The electronic and optical properties of BiT were performed at a more fundamental level, where the electron distribution of the system, with suitable approximation, was taken into account. It showed that the GGA method could provide qualitative description of the optical properties, although such properties could be better evaluated using the HSE method. It is worthwhile to mention that considering the demanding

computational resources of hybrid functionals, GGA should be the pragmatic choice for most DFT calculations since it can always provide qualitative results.

6.2 Suggestions for Future Work

Even though various type of modeling approaches for ferroelectric materials are discussed in this Thesis, a great amount of challenges still go beyond the current effort. The motivation of this work was initialized from the diverse electrical properties of ferroelectric materials for multi-functional devices, such as memories, sensors, actuators, and filters. For such applications, not only switchable ferroelectric polarization is necessary, but also piezoelectric and pyroelectric properties are in the range of interest. The proposed applications greatly rely on the behavior of the ferroelectric domain walls as it becomes extremely important to understand the underlying mechanisms in applied electric field or varied temperature. The motion of domain walls, including its stability and growth, determine its performance and reliability in electronic devices. From the microscopic point of view, the ferroelectric domain behaves very differently than the ferromagnetic domain, in which the direction of magnetization rotates step-wisely between opposite domains. However, the orientation of the polarization changes abruptly from one end to another in ferroelectrics, and the intermediate region are in the order of two lattice constants.

One of the pioneering works of domain wall investigation using first-

principles calculations was reported by Padilla *et al.* using prototypical $BaTiO_3$ perovskite.[280] The domain phases are determined by the balance between long-range dipole-dipole interactions in which the ferroelectric state is preferred, and short-range interaction where paraelectric state is favorable. Since then, first-principles calculations have become a standard approach to study ferroelectric materials, including lattice dynamics, phase transformations, dielectric and piezoelectric properties, which considering defects and surface configurations.[281] Boundaries, defects, interfaces, domains and the mixture of these, play a critical role in the determination of crystal structure and thus materials properties. For example, He and Vanderbilt have reported the interaction of oxygen vacancies and 180° domain walls in tetragonal $PbTiO_3$ (PTO) using DFT.[282] Compared to bulk PTO, the formation energy with oxygen vacancies are lower in the domain wall, indicating the pinning of domain walls. Furthermore, the presence of acceptor Fe and donor Nb dopants were introduced to investigate the defect ordering and domain wall interactions in PTO.[283] Chandrasekaran *et al.* conclude that not only oxygen vacancies, but also lead vacancies, niobium substitutional defects, and lanthanum substitutional defects are more stable at the domain wall. Moreover, the magnetic ordering combined with ferroelectric polarization in multiferroic materials show profound physical properties, which attracts great attention in the community for its potential magnetoelectronic applications.[284,285] To understand such a length scale (~nanometer) using first-principles approach is scientifically important and useful for fine tailoring

of electronic properties of materials.

In regards to the formerly discussed research problems, the high demand of electronic structure computations is impractical for larger lengths and longer time scales, which are of desire. For the system where experimental measurements are lacking, the input parameters from first-priciples calculations are essentially required to construct the model. There are two main approaches to create such a model: the effective Hamiltonian[286,287] and atomic-level simulations.[288] The advantage of atomistic modeling over effective Hamiltonian approach is that all interactions are included in detail so that one can trace the effect on individual energy term. In general, the well-designated model should always contain accurate results when compared to available experimental or theoretical values, while taking computational complexity at long time and large length scales into account.

In order to describe changes of electronic structures resulting from interacting atoms, the shell model has been greatly used due to its straightforward representation. The atom of shell model is constructed as two charged and coupled particles linked by a spring. One particle is massive core and the other is massless shell. In a shell model, the electrostatic interactions are taken into account as between the cores and shells from different atoms but not between the core and shell of the same atom. There are several developments along the same line to the ferroelectric oxides. For example, Goddard *et al.* have reported the shell model, where charge transfer is incorporated into the model for study-

ing the phase transitions of $BaTiO_3$.[289] Ponomareva *et al.* have investigated the ferroelectric systems in zero- and one-dimensional.[290] The same methodology might be extended to other geometry such as a series of nanowires and an array of nanodots, which contain lots of technological potential for electronic applications. Furthermore, for the situation that experimental results have been reported in particular material, the development of similar materials might still be very challenging due to the lack of understanding in fundamental level. Shin *et al.* have successfully implemented various modeling techniques, including atomistic molecular dynamics and coarse-grained Monte Carlo simulations to demonstrate the nucleation and growth mechanism of PTO domain-wall motion.[291] They have also show the analytical model discussing the experimental rate in PTO and BTO. By combining the first-principles calculations with phase-field simulations, 180° ferroelectric domain walls of BTO on different crystallographic planes have been reported, and Bloch and Néel type ising character of polarization have been revealed.[292] The atomistic model has been extended to more complicated alloys, in which there is great interest for actual applications. For instance, both PTO and $PbZrO_3$ (PZO) do not exhibit high piezoelectric properties, but its solid solution ($PbZr_{1-x}Ti_xO_3$, or PZT) contains an exceptionally high piezoelectric response at the morphotropic phase boundary (MPB).[293] The shell model has been developed to reproduce the phase diagram of PZT as a function of temperature and Ti content.[294] New techniques have been developed and these model have provided the platform

to understand such mechanisms. Ferroelectric phase instabilities, electromechanical coupling, phonon dispersion, dielectric and optical properties, and some interface and surface configurations have been successfully investigated for a better rudimentary understanding. Lastly, but most importantly, one has to carefully validate the model prior to the investigation of more complex systems due to the nature of parameterization of the atomic simulation. Based on the knowledge of the well-studied materials, do we have the ability to design new materials using computational method? Even further, can we really design materials to achieve desired properties in the laboratory?

In the century of modern technology, innovative scientific and engineering solution has been provoked to conduct basic and applied physics research. With the assistance of high performance computational resources and efficient algorithms, the new branch of research has delivered great success complementing traditional theoretical and experimental approaches. While increasing productivity and reducing cost, computational materials science has simultaneously expedited the discovery of searching, predicting, and improving new materials. This idea has been successfully applied on functional, structural, electronic, biological material systems, while challenges still remain.

Ultimately, multi-scale modeling and machine learning type of research will grow faster than ever. In reality, a certain level of approximations are necessary to build models and if the subtle importance of the system has been screened in the first instance, the model will by no mean ”see” the feature.

If the model was based on less empirical input parameters, then a predictive capability should be realized for other conditions. The advent of high performance, efficient algorithms, and even intellectual computing will guide the development of modern materials modeling to a new era.

Bibliography

[1] S. M. Nakhmanson, M. Buongiorno Nardelli, and J. Bernholc. Collective polarization effects in β-polyvinylidene fluoride and its copolymers with tri- and tetrafluoroethylene. *Phys. Rev. B*, 72:115210, 2005.

[2] Koh Nakamura, Daisuke Sawai, Yuuji Watanabe, Daisuke Taguchi, Yoshiyuki Takahashi, Takeo Furukawa, and Tetsuo Kanamoto. Effect of annealing on the structure and properties of poly(vinylidene fluoride) β-form films. *J. Polym. Sci. Part B Polym. Phys.*, 41:1701, 2003.

[3] Hiroji Ohigashi, Kenji Omote, and Teruhisa Gomyo. Formation of single crystalline films" of ferroelectric copolymers of vinylidene fluoride and trifluoroethylene. *Appl. Phys. Lett.*, 66(24):3281–3283, 1995.

[4] Yoshiro Tajitsu, Hiroshi Ogura, Akio Chiba, and Takeo Furukawa. Investigation of Switching Characteristics of Vinylidene Fluoride/Trifluoroethylene Copolymers in Relation to Their Structures. *Jpn. J. Appl. Phys.*, 26:554–560, 1987.

[5] H Kliem and R Tadros-Morgane. Extrinsic versus intrinsic ferroelectric switching: experimental investigations using ultra-thin PVDF Langmuir-Blodgett films. *J. Phys. D. Appl. Phys.*, 38:1860–1868, 2005.

[6] Mp Allen. Introduction to molecular dynamics simulation. *Comput. Soft Matter From Synth. Polym. to Proteins*, 23:1–28, 2004.

[7] Daan Frenkel and Berend Smit. In *Understanding Molecular Simulation (Second Edition)*. Academic Press, San Diego, second edition edition, 2002.

[8] M P Allen and D J Tildesley. *Computer Simulation of Liquids*. Clarendon Press, New York, NY, USA, 1989.

[9] JiÅí Klimeš, David R. Bowler, and Angelos Michaelides. Van der Waals density functionals applied to solids. *Phys. Rev. Beview B*, 83:195131, 2011.

[10] T. Björkman, A. Gulans, A. V. Krasheninnikov, and R. M. Nieminen. Van der Waals bonding in layered compounds from advanced density-functional first-principles calculations. *Phys. Rev. Lett.*, 108:235502, 2012.

[11] George M Whitesides and Bartosz Grzybowski. Self-assembly at all scales. *Science*, 295(5564):2418–21, 2002.

[12] Svetla D. Chakarova-Käck, Elsebeth Schröder, Bengt I. Lundqvist, and David C. Langreth. Application of van der Waals density functional to an extended system: Adsorption of benzene and naphthalene on graphite. *Phys. Rev. Lett.*, 96:146107, 2006.

[13] Javier Carrasco, Biswajit Santra, JiÅí Klimeš, and Angelos Michaelides. To wet or not to wet? dispersion forces tip the balance for water ice on metals. *Phys. Rev. Lett.*, 106(2):1–4, 2011.

[14] P. Hohenberg and W. Kohn. Inhomogeneous electron gas. *Phys. Rev.*, 136:B864, 1964.

[15] W. Kohn and L. J. Sham. Self Consistent Equations Including Exchange and Correlation Effects. *Phys. Rev.*, 140:A1133, 1965.

[16] P. A. M. Dirac. Note on Exchange Phenomena in the Thomas Atom. *Math. Proc. Cambridge Philos. Soc.*, 26:376, 1930.

[17] D M Ceperley and B J Alder. Ground state of the electron gas by a stochastic model. *Phys. Rev. Lett.*, 45(7):566–569, 1980.

[18] S. H. Vosko, L. Wilk, and M. Nusair. Accurate spin-dependent electron liquid correlation energies for local spin density calculations: a critical analysis. *Can. J. Phys.*, 58(8):1200–1211, 1980.

[19] John Perdew, J. Chevary, S. Vosko, Koblar Jackson, Mark Pederson, D. Singh, and Carlos Fiolhais. Atoms, molecules, solids, and surfaces: Applications of the generalized gradient approximation for exchange and correlation. *Phys. Rev. B*, 46:6671, 1992.

[20] John P. Perdew, Kieron Burke, and Matthias Ernzerhof. Generalized Gradient Approximation Made Simple. *Phys. Rev. Lett.*, 77(18):3865–3868, 1996.

[21] A. D. Becke. Density-functional exchange-energy approximation with correct asymptotic behavior. *Phys. Rev. A*, 38(6):3098–3100, 1988.

[22] Michele Lazzeri, Claudio Attaccalite, Ludger Wirtz, and Francesco Mauri. Impact of the electron-electron correlation on phonon dispersion: Failure of LDA and GGA DFT functionals in graphene and graphite. *Phys. Rev. B*, 78:081406, 2008.

[23] Philip J. Hasnip, Keith Refson, Matt I. J. Probert, Jonathan R. Yates, Stewart J. Clark, and Chris J. Pickard. Density functional theory in the solid state. *Phil. Trans. R. Soc. A*, 372:20130270, 2013.

[24] Axel D. Becke. Density-functional thermochemistry. III. The role of exact exchange. *J. Chem. Phys.*, 98(7):5648, 1993.

[25] Aron J. Cohen, Paula Mori-Sanchez, and Weitao Yang. Challenges for density functional theory. *Chem. Rev.*, 112:289–320, 2012.

[26] Antonín Vlček and Stanislav Záliš. Modeling of charge-transfer transitions and excited states in d6 transition metal complexes by DFT techniques. *Coord. Chem. Rev.*, 251(3-4):258–287, 2007.

[27] Stephan N. Steinmann, Cyril Piemontesi, Aurore Delachat, and Clemence Corminboeuf. Why are the interaction energies of charge-transfer complexes challenging for DFT? *J. Chem. Theory Comput.*, 8(5):1629–1640, 2012.

[28] Erich Runge and E. K U Gross. Density-functional theory for time-dependent systems. *Phys. Rev. Lett.*, 52(12):997–1000, 1984.

[29] R. O. Jones. Density functional theory: Its origins, rise to prominence, and future. *Rev. Mod. Phys.*, 87(3):897, 2015.

[30] M. C. Payne, M. P. Teter, D. C. Allan, T. A. Arias, and J. D. Joannopoulos. Iterative minimization techniques for ab initio total-energy calculations: Molecular dynamics and conjugate gradients. *Rev. Mod. Phys.*, 64(4):1045–1097, 1992.

[31] J. C. Phillips. Energy-Band Interpolation Scheme Based on a Pseudopotential. *Phys. Rev.*, 112:685, 1958.

[32] James C. Phillips and Leonard Kleinman. New Method for Calculating Wave Functions in Crystals and Molecules. *Phys. Rev.*, 116:287, 1959.

[33] Jacques Curie and Pierre Curie. Development by pressure of polar electricity in hemihedral crystals with inclined faces. *Bull. soc. min. de France*, 3:90, 1880.

[34] H S Tzou and C I Tseng. Distributed piezoelectric sensor/actuator design for dynamic measurement/control of distributed parameter systems: A piezoelectric finite element approach. *J. Sound Vib.*, 138(1):17–34, 1990.

[35] Ahmad Safari and E. Koray Akdogan. *Piezoelectric and Acoustic Materials for Transducer Applications*. Springer US, 2008.

[36] Hua-Bin Fang, Jing-Quan Liu, Zheng-Yi Xu, Lu Dong, Li Wang, Di Chen, Bing-Chu Cai, and Yue Liu. Fabrication and performance of MEMS-based piezoelectric power generator for vibration energy harvesting. *Microelectronics J.*, 37(11):1280–1284, 2006.

[37] M I H Yaacob, M R Arshad, and A Abd. Manaf. Modeling of circular piezoelectric micro ultrasonic transducer using CuAl10Ni5Fe4 on ZnO film for sonar applications. *Acoust. Phys.*, 57(2):151, 2011.

[38] Robert E Newnham. *Properties of materials: anisotropy, symmetry, structure*. Oxford University Press on Demand, 2005.

[39] Dragan Damjanovic. Ferroelectric, dielectric and piezoelectric properties of ferroelectric thin films and ceramics. *Reports on Progress in Physics*, 61(9):1267, 1998.

[40] A L Kholkin, M L Calzada, P Ramos, J Mendiola, and N Setter. Piezoelectric properties of Ca-modified PbTiO3 thin films. *Appl. Phys. Lett.*, 69(23):3602, 1996.

[41] Gabriel L Smith, Jeffrey S Pulskamp, Luz M Sanchez, Daniel M Potrepka, Robert M Proie, Tony G Ivanov, Ryan Q Rudy, William D Nothwang, Sarah S Bedair, Christopher D Meyer, and Ronald G Polcawich. PZT-Based Piezoelectric MEMS Technology. *J. Am. Ceram. Soc.*, 95(6):1777–1792, 2012.

[42] Satoshi W Wada, Shingo S Uzuki, Tatsuo N Oma, Takeyuki S Uzuki, and Minoru O Sada. Enhanced Piezoelectric Property of Barium Titanate Single Crystals with Engineered Domain Configurations Enhanced Piezoelectric Property of Barium Titanate Single Crystals with Engineered Domain Configurations. *Jpn. J. Appl. Phys.*, 38:5505, 1999.

[43] G Shirane, R Newnham, and R Pepinsky. Dielectric Properties and Phase Transitions of NaNbO3 and (Na,K)NbO3. *Phys. Rev.*, 96(3):581–588, 1954.

[44] R. Nath, S. Zhong, S. P. Alpay, B. D. Huey, and M. W. Cole. Enhanced piezoelectric response from barium strontium titanate multilayer films. *Appl. Phys. Lett.*, 92:012916, 2008.

[45] Cihangir Duran, Susan Trolier-McKinstry, and Gary L. Messing. Fabrication and Electrical Properties of Textured Sr0.53Ba0.47Nb2O6 Ceramics by Templated Grain Growth. *J. Am. Ceram. Soc.*, 83(9):2203–2213, 2004.

[46] Don L. DeVoe. Piezoelectric thin film micromechanical beam resonators. *Sensors Actuators, A Phys.*, 88(3):263–272, 2001.

[47] Seung-Eek Park and Thomas R. Shrout. Ultrahigh strain and piezoelectric behavior in relaxor based ferroelectric single crystals. *J. Appl. Phys.*, 82(4):1804, 1997.

[48] B Jaffe, R S Roth, and S Marzullo. Properties of piezoelectric ceramics in the solid-solution series lead titanate-lead zirconate-lead oxide: tin oxide

and lead titanate-lead hafnate. *J. Res. Natl. Bur. Stand. (1934).*, 55(5):239–254, 1955.

[49] JN Kim, Michael J Haun, Sej Joo Jang, Lesli E Cross, and XR Xue. Temperature behavior of dielectric and piezoelectric properties of samarium-doped lead titanate ceramics. *IEEE transactions on ultrasonics, ferroelectrics, and frequency control*, 36(4):389–392, 1989.

[50] Shoufu Shao, Jialiang Zhang, Zhong Zhang, Peng Zheng, Minglei Zhao, Jichao Li, and Chunlei Wang. High piezoelectric properties and domain configuration in BaTiO3 ceramics obtained through solid-state reaction route. *J. Phys. D. Appl. Phys.*, 42(18):189801–189801, 2009.

[51] D. A. Barrow, T. E. Petroff, R. P. Tandon, and M. Sayer. Characterization of thick lead zirconate titanate films fabricated using a new sol gel based process. *J. Appl. Phys.*, 81(2):876–881, 1997.

[52] Z Huang, G Leighton, R Wright, F Duval, H C Chung, P Kirby, and R W Whatmore. Determination of piezoelectric coefficients and elastic constant of thin films by laser scanning vibrometry techniques. *Sensors Actuators A Phys.*, 135(2):660–665, 2007.

[53] Dan Liu and JiangYu Li. The enhanced and optimal piezoelectric coefficients in single crystalline barium titanate with engineered domain configurations. *Appl. Phys. Lett.*, 83(6):1193–1195, 2003.

[54] Seung-Eek Park, Satoshi Wada, L E Cross, and Thomas R Shrout. Crystallographically engineered BaTiO3 single crystals for high-performance piezoelectrics. *J. Appl. Phys.*, 86:2746–2750, 1999.

[55] Walter J Merz. The effect of hydrostatic pressure on the Curie point of barium titanate single crystals. *Phys. Rev.*, 78(1):52, 1950.

[56] Hirofumi Takahashi, Yoshiki Numamoto, Junji Tani, Kazuya Matsuta, Jinhao Qiu, and Sadahiro Tsurekawa. Lead-free barium titanate ceramics with large piezoelectric constant fabricated by microwave sintering. *Jpn. J. Appl. Phys.*, 45(1):L30, 2006.

[57] M G Harwood, P Popper, and D F Rushman. Curie point of barium titanate. *Nature*, 160:58–59, 1947.

[58] Richard J Meyer, Robert E Newnham, Ahmed Amin, and Bernard M Kulwicki. Flextensional barium strontium titanate actuators. *J. Am. Ceram. Soc.*, 86(6):934–938, 2003.

[59] D-S Paik, S-E Park, T R Shrout, and W Hackenberger. Dielectric and piezoelectric properties of perovskite materials at cryogenic temperatures. *J. Mater. Sci.*, 34(3):469–473, 1999.

[60] Moumita Ghosh and Mohan G Rao. Growth mechanism of ZnO nanostructures for ultra-high piezoelectric d 33 coefficient. *Mater. Express*, 3(4):319–327, 2013.

[61] Min-Hua Zhao, Zhong-Lin Wang, and Scott X Mao. Piezoelectric characterization of individual zinc oxide nanobelt probed by piezoresponse force microscope. *Nano Lett.*, 4(4):587–590, 2004.

[62] F Martin, P Muralt, M-A Dubois, and A Pezous. Thickness dependence of the properties of highly c-axis textured AlN thin films. *J. Vac. Sci. Technol. A*, 22(2):361–365, 2004.

[63] Hongliang Du, Wancheng Zhou, Fa Luo, Dongmei Zhu, Shaobo Qu, Ye Li, and Zhibin Pei. Structure and electrical properties' investigation of (K0.5Na0.5) NbO3–(Bi0.5Na0.5) TiO3 lead-free piezoelectric ceramics. *J. Phys. D. Appl. Phys.*, 41(8):85416, 2008.

[64] A A Ballman and H Brown. The growth and properties of strontium barium metaniobate, Sr1-xBaxNb2O6, a tungsten bronze ferroelectric. *J. Cryst. Growth*, 1(5):311–314, 1967.

[65] Kazuo Matsuo, Rong-Jun Xie, Yoshio Akimune, and Tatsuo Sugiyama. Preparation of Lead-Free Sr2_xCaxNaNb5O15 (x=0.1)-Based Piezoceramics with Tungsten Bronze Structure. *J. Ceram. Soc. Japan*, 110(5):491–494, 2002.

[66] S Karimi, I M Reaney, Y Han, J Pokorny, and I Sterianou. Crystal chemistry and domain structure of rare-earth doped BiFeO3 ceramics. *J. Mater. Sci.*, 44(19):5102–5112, 2009.

[67] Nick M Sbrockey, Gary S Tompa, Thottam S Kalkur, Jialan Zhang, S Pamir Alpay, and Melanie W Cole. Voltage induced acoustic resonance in metal organic chemical vapor deposition srtio3 thin film. *Journal of Vacuum Science & Technology B*, 30(6):061202, 2012.

[68] H. Y. Kuo, Y. C. Shu, H. Z. Chen, C. J. Hsueh, C. H. Wang, and Y. H. Chu. Domain pattern and piezoelectric response across polymorphic phase transition in strained bismuth ferrite films. *Appl. Phys. Lett.*, 97:242906, 2010.

[69] Alexandre Zirpoli Simões, A H M Gonzalez, E C Aguiar, C S Riccardi, Elson Longo, and José Arana Varela. Piezoelectric behavior of SrRuO3 buffered lanthanum modified bismuth ferrite thin films grown by chemical method. *Appl. Phys. Lett.*, 93:142902, 2008.

[70] H. Khassaf, G. A. Ibanescu, I. Pintilie, I. B. Misirlioglu, and L. Pintilie. Potential barrier increase due to Gd doping of BiFeO3 layers in Nb:SrTiO3-BiFeO3-Pt structures displaying diode-like behavior. *Appl. Phys. Lett.*, 100:252903, 2012.

[71] P K Panda. Review: environmental friendly lead-free piezoelectric materials. *J. Mater. Sci.*, 44(19):5049–5062, 2009.

[72] Daniel E Grupp and Allen M Goldman. Giant piezoelectric effect in strontium titanate at cryogenic temperatures. *Science (80-.).*, 276(5311):392–394, 1997.

[73] Srivatsan Sathyamurthy and Kamel Salama. Chemical solution deposition of highly oriented strontium titanate buffer layers for coated conductors. *Supercond. Sci. Technol.*, 13(7):L1, 2000.

[74] J. Zhang, I. B. Misirlioglu, S. P. Alpay, and G. a. Rossetti. Electrocaloric properties of epitaxial strontium titanate films. *Appl. Phys. Lett.*, 100(22):222909, 2012.

[75] P. A. Fleury, J. F. Scott, and J. M. Worlock. Soft phonon modes and the 110K phase transition in SrTiO3. *Phys. Rev. Lett.*, 21(1):16–19, 1968.

[76] J G Bednorz and K A Müller. Sr1-xCaxTiO3: An XY Quantum Ferroelectric with Transition to Randomness. *Phys. Rev. Lett.*, 52(25):2289, 1984.

[77] A F Devonshire. Theory of ferroelectrics. *Adv. Phys.*, 3(10):85–130, 1954.

[78] C. V. Weiss, J. Zhang, M. Spies, L. S. Abdallah, S. Zollner, M. W. Cole, and S. P. Alpay. Bulk-like dielectric properties from metallo-organic solution-deposited SrTiO3 films on Pt-coated Si substrates. *J. Appl. Phys.*, 111(5):054108, 2012.

[79] JH Haeni, P Irvin, W Chang, R Uecker, P Reiche, YL Li, S Choudhury, W Tian, ME Hawley, B Craigo, et al. Room-temperature ferroelectricity in strained srtio3. *Nature*, 430(7001):758–761, 2004.

[80] L Pardo, J Mendiola, and C Alemany. Theoretical treatment of ferroelectric composites using Monte Carlo calculations. *J. Appl. Phys.*, 64(10):5092–5097, 1988.

[81] Long-Qing Chen. Phase-Field Method of Phase Transitions/Domain Structures in Ferroelectric Thin Films: A Review. *J. Am. Ceram. Soc.*, 91(6):1835–1844, 2008.

[82] M Sepliarsky, SR Phillpot, MG Stachiotti, and RL Migoni. Ferroelectric phase transitions and dynamical behavior in knbo3/ktao3 superlattices by

molecular-dynamics simulation. *Journal of applied physics*, 91(5):3165–3171, 2002.

[83] R Khenata, M Sahnoun, H Baltache, M Rerat, A H Rashek, N Illes, and B Bouhafs. First-principle calculations of structural, electronic and optical properties of BaTiO3 and BaZrO3 under hydrostatic pressure. *Solid State Commun.*, 136(2):120–125, 2005.

[84] W F Li and G J Weng. A micromechanics-based thermodynamic model for the domain switch in ferroelectric crystals. *Acta Mater.*, 52(8):2489–2496, 2004.

[85] N. A. Pertsev, A. K. Tagantsev, and N. Setter. Phase transitions and strain-induced ferroelectricity in SrTiO3 epitaxial thin films. *Phys. Rev. B*, 61(2):R825–R829, 2000.

[86] N. A. Pertsev, A. K. Tagantsev, and N. Setter. Erratum: Phase transitions and strain-induced ferroelectricity in SrTiO3 epitaxial thin films [Phys. Rev. B 61, R825 (2000)]. *Phys. Rev. B*, 65(21):219901, 2002.

[87] A V Tumarkin, M M Gaidukov, S V Razumov, and A G Gagarin. Capacitor structures based on strontium titanate films. *Phys. Solid State*, 54(5):968–971, 2012.

[88] K Fröhlich, D Machajdik, A Rosova, I Vavra, F Weiss, B Bochu, and J P Senateur. Growth of SrTiO3 thin epitaxial films by aerosol MOCVD. *Thin Solid Films*, 260(2):187–191, 1995.

[89] Maitri P Warusawithana, Cheng Cen, Charles R Sleasman, Joseph C Woicik, Yulan Li, Lena Fitting Kourkoutis, Jeffrey A Klug, Hao Li, Philip Ryan, Li-Peng Wang, and Others. A ferroelectric oxide made directly on silicon. *Science (80-.).*, 324(5925):367–370, 2009.

[90] Dooho Choi, Dongsoo Lee, Hyunjun Sim, Man Chang, and Hyunsang Hwang. Reversible resistive switching of SrTiOx thin films for nonvolatile memory applications. *Appl. Phys. Lett.*, 88(8):82904, 2006.

[91] Z G Ban, S P Alpay, Feizhou He, B O Wells, and X X Xi. Multiple relaxation mechanisms in SrTiO3/SrRuO3 heterostructures. *Appl. Phys. Lett.*, 84(24):4848, 2004.

[92] J W Matthews and A E Blakeslee. Defects in epitaxial multilayers: I. Misfit dislocations. *J. Cryst. Growth*, 27:118–125, 1974.

[93] Luke S J Peng, X X Xi, Brian H Moeckly, and S P Alpay. Strain relaxation during in situ growth of SrTiO3 thin films. *Appl. Phys. Lett.*, 83(22):4592–4594, 2003.

[94] H. Khassaf, N. Khakpash, F. Sun, N. M. Sbrockey, G. S. Tompa, T. S. Kalkur, and S. P. Alpay. Strain engineered barium strontium titanate for tunable thin film resonators. *Appl. Phys. Lett.*, 104:202902, 2014.

[95] R. B. Karabalin, M. H. Matheny, X. L. Feng, E. Defa, G. Le Rhun, C. Marcoux, S. Hentz, P. Andreucci, and M. L. Roukes. Piezoelectric nanoelectromechanical resonators based on aluminum nitride thin films. *Appl. Phys. Lett.*, 95(10):103111, 2009.

[96] J Hees, N Heidrich, W Pletschen, R E Sah, M Wolfer, O a Williams, V Lebedev, C E Nebel, and O Ambacher. Piezoelectric actuated micro-resonators based on the growth of diamond on aluminum nitride thin films. *Nanotechnology*, 24(2):025601, 2013.

[97] N.M. Sbrockey, Gary S Tompa, T.S. Kalkur, Jialan Zhang, S.P. Pamir Alpay, and M.W. Cole. Voltage induced acoustic resonance in metal organic chemical vapor deposition SrTiO3 thin film. *J. Vac. Sci. Technol. B*, 30(6):61202, 2012.

[98] Qing Guo, G Z Cao, and I Y Shen. Measurements of Piezoelectric Coefficient d33 of Lead Zirconate Titanate Thin Films Using a Mini Force Hammer. *J. Vib. Acoust.*, 135(1):11003, 2013.

[99] Zhaorong Huang, Qi Zhang, Silvana Corkovic, Robert Dorey, and Roger W. Whatmore. Comparative measurements of piezoelectric coefficient of PZT films by berlincourt, interferometer, and vibrometer methods. *IEEE Trans. Ultrason. Ferroelectr. Freq. Control*, 53(12):2287–2292, 2006.

[100] A. N. Cleland, M. Pophristic, and I. Ferguson. Single-crystal aluminum nitride nanomechanical resonators. *Appl. Phys. Lett.*, 79(13):2070–2072, 2001.

[101] John Berge, Andrei Vorobiev, William Steichen, and Spartak Gevorgian. Tunable solidly mounted thin film bulk acoustic resonators based on BaxSr1-xTiO3 films. *IEEE Microw. Wirel. Components Lett.*, 17(9):655–657, 2007.

[102] Vl. M. Mukhortov, S. V. Biryukov, Yu. I. Golovko, G. Ya. Karapet'yan, S. I. Masychev, and Vas. M. Mukhortov. Surface acoustic waves in thin films of barium strontium titanate on magnesium oxide substrates. *Tech. Phys. Lett.*, 37(3):207–209, 2011.

[103] Andreas Noeth, Tomoaki Yamada, Vladimir O. Sherman, Paul Muralt, Alexander K. Tagantsev, and Nava Setter. Tuning of direct current bias-induced resonances in micromachined Ba0.3Sr0.7TiO3 thin-film capacitors. *J. Appl. Phys.*, 102:114110, 2007.

[104] Kentaro Morito, Yoshiki Iwazaki, Toshimasa Suzuki, and Masayuki Fujimoto. Electric field induced piezoelectric resonance in the micrometer to millimeter waveband in a thin film SrTiO3 capacitor. *J. Appl. Phys.*, 94(8):5199–5205, 2003.

[105] G. N. Saddik, D. S. Boesch, S. Stemmer, and R. A. York. Dc electric field tunable bulk acoustic wave solidly mounted resonator using SrTiO3. *Appl. Phys. Lett.*, 91(4):043501, 2007.

[106] S. Tappe, U. Böttger, and R. Waser. Electrostrictive resonances in (Ba0.7Sr0.3)TiO 3 thin films at microwave frequencies. *Appl. Phys. Lett.*, 85(4):624–626, 2004.

[107] Guru Subramanyam, M. W. Cole, Nian X. Sun, Thottam S. Kalkur, Nick M. Sbrockey, Gary S. Tompa, Xiaomei Guo, Chonglin Chen, S. P. Alpay, G. A. Rossetti, Kaushik Dayal, Long Qing Chen, and Darrell G. Schlom. Challenges and opportunities for multi-functional oxide thin films for voltage tunable radio frequency/microwave components. *J. Appl. Phys.*, 114(19):191301, 2013.

[108] N. K. Pervez, P. J. Hansen, and R. A. York. High tunability barium strontium titanate thin films for rf circuit applications. *Appl. Phys. Lett.*, 85(19):4451–4453, 2004.

[109] Wontae Chang, Charles M. Gilmore, Won-Jeong Kim, Jeffrey M. Pond, Steven W. Kirchoefer, Syed B. Qadri, Douglas B. Chirsey, and James S. Horwitz. Influence of strain on microwave dielectric properties of (Ba,Sr)TiO3 thin films. *J. Appl. Phys.*, 87(6):3044, 2000.

[110] Jaemo Im, O. Auciello, P. K. Baumann, S. K. Streiffer, D. Y. Kaufman, and A. R. Krauss. Composition-control of magnetron-sputter-deposited (BaxSr1-x)Ti 1+yO3+z thin films for voltage tunable devices. *Appl. Phys. Lett.*, 76(2000):625–627, 2000.

[111] C. L. Chen, J. Shen, S. Y. Chen, G. P. Luo, C. W. Chu, F. A. Miranda, F. W. Van Keuls, J. C. Jiang, E. I. Meletis, and H. Y. Chang. Epitaxial growth of dielectric Ba0.6Sr0.4TiO3 thin film on MgO for room temperature microwave phase shifters. *Appl. Phys. Lett.*, 78(5):652–654, 2001.

[112] S. Gevorgian, A. Vorobiev, and T. Lewin. Dc field and temperature dependent acoustic resonances in parallel-plate capacitors based on SrTiO3 and Ba0.25Sr0.75TiO3 films: Experiment and modeling. *J. Appl. Phys.*, 99:124112, 2006.

[113] Z. G. Ban and S. P. Alpay. Phase diagrams and dielectric response of epitaxial barium strontium titanate films: A theoretical analysis. *J. Appl. Phys.*, 91(11):9288–9296, 2002.

[114] M. Tyunina, I. Jaakola, J. Levoska, and M. Plekh. Diffuse phase transitions in epitaxial (Ba, Sr)TiO3 superlattices. *Phys. Rev. B*, 76:134107, 2007.

[115] R. Dittmann, R. Plonka, E. Vasco, N. A. Pertsev, J. Q. He, C. L. Jia, S. Hoffmann-Eifert, and R. Waser. Sharp ferroelectric phase transition in strained single-crystalline SrRuO3/Ba0.7Sr0.3TiO3/SrRuO3 capacitors. *Appl. Phys. Lett.*, 83(24):5011–5013, 2003.

[116] L. B. Kong, S. Li, T. S. Zhang, J. W. Zhai, F. Y C Boey, and J. Ma. Electrically tunable dielectric materials and strategies to improve their performances. *Prog. Mater. Sci.*, 55(8):840–893, 2010.

[117] J H Haeni, P Irvin, W Chang, R Uecker, P Reiche, Y L Li, S Choudhury, W Tian, M E Hawley, B Craigo, A K Tagantsev, X Q Pan, S K Streiffer, L Q Chen, S W Kirchoefer, J Levy, and D G Schlom. Room-temperature ferroelectricity in strained SrTiO3. *Nature*, 430:758–761, 2004.

[118] Pierre-Eymeric Janolin. Strain on ferroelectric thin films. *J. Mater. Sci.*, 44(19):5025–5048, 2009.

[119] R.E. Newnham. *Properties of Materials: Anisotropy, Symmetry, Structure*. OUP Oxford, 2004.

[120] J. S. Speck and W. Pompe. Domain configurations due to multiple misfit relaxation mechanisms in epitaxial ferroelectric thin films. I. Theory. *J. Appl. Phys.*, 76(1):466, 1994.

[121] J W Matthews and A E Blakeslee. Defects in epitaxial multilayers. *J. Cryst. Growth*, 27:118–125, 1974.

[122] Luke S J Peng, X X Xi, Brian H Moeckly, and S P Alpay. Strain relaxation during in situ growth of SrTiO[sub 3] thin films. *Appl. Phys. Lett.*, 83(22):4592–4594, 2003.

[123] Deepam Maurya, Fu-Chang Sun, S. Pamir Alpay, and Shashank Priya. A new method for achieving enhanced dielectric response over a wide temperature range. *Sci. Rep.*, 5:15144, 2015.

[124] A Ohtomo and H Y Hwang. A high-mobility electron gas at the LaAlO3/SrTiO3 heterointerface. *Nature*, 427:423–426, 2004.

[125] J B Neaton and K M Rabe. Theory of polarization enhancement in epitaxial BaTiO3/SrTiO3 superlattices. *Appl. Phys. Lett.*, 82(10):1586–1588, 2003.

[126] M. Dawber, C. Lichtensteiger, M. Cantoni, M. Veithen, P. Ghosez, K. Johnston, K. M. Rabe, and J.-M. M. Triscone. Unusual Behavior of the Ferroelectric

Polarization in PbTiO3/SrTiO3 Superlattices. *Phys. Rev. Lett.*, 95:177601, oct 2005.

[127] Karen Johnston, Xiangyang Huang, J. B. Neaton, and Karin M. Rabe. First-principles study of symmetry lowering and polarization in BaTiO3/SrTiO3 superlattices with in-plane expansion. *Phys. Rev. B*, 71:100103, 2005.

[128] Javier Junquera and Philippe Ghosez. First-Principles Study of Ferroelectric Oxide Epitaxial Thin Films and Superlattices: Role of the Mechanical and Electrical Boundary Conditions. *J. Comput. Theor. Nanosci.*, 5(11):2071–2088, 2008.

[129] Xifan Wu, Karin M Rabe, and David Vanderbilt. Interfacial enhancement of ferroelectricity in CaTiO3/BaTiO3 superlattices. *Phys. Rev. B*, 83(2):20104, 2011.

[130] D Schwenk, F Fishman, and F Schwabl. Phase transitions and soft modes in ferroelectric superlattices. *J. Phys. Condens. Matter*, 2(24):5409, 1990.

[131] Yulan Li, S. Y. Hu, D. Tenne, A. Soukiassian, Darrell G. Schlom, X. X. Xi, K J. Choi, Chang-Beom Eom, A. Saxena, T. Lookman, Q X. Jia, and Long-Qing Chen. Prediction of ferroelectricity in BaTiO3/SrTiO3 superlattices with domains. *Appl. Phys. Lett.*, 91(11):112914–112916, 2007.

[132] Toru Shimuta, Osamu Nakagawara, Takahiro Makino, Seiichi Arai, Hitoshi Tabata, and Tomoji Kawai. Enhancement of remanent polarization in epitaxial BaTiO3/SrTiO3 superlattices with "asymmetric" structure. *J. Appl. Phys.*, 91(4):2290–2294, 2002.

[133] M Dawber, P Chandra, P B Littlewood, and J F Scott. Depolarization corrections to the coercive field in thin-film ferroelectrics. *J. Phys. Condens. Matter*, 15(24):L393, 2003.

[134] Z.-G. Ban, S P Alpay, and J V Mantese. Fundamentals of graded ferroic materials and devices. *Phys. Rev. B*, 67(18):184104, may 2003.

[135] I. B. Misirlioglu, G. Akcay, S. Zhong, and S. P. Alpay. Interface effects in ferroelectric bilayers and heterostructures. *J. Appl. Phys.*, 101(3):36107, 2007.

[136] Eric Bousquet, Matthew Dawber, Nicolas Stucki, Céline Lichtensteiger, Patrick Hermet, Stefano Gariglio, Jean-Marc Triscone, and Philippe Ghosez. Improper ferroelectricity in perovskite oxide artificial superlattices. *Nature*, 452:732–736, 2008.

[137] A. L. Roytburd, S. Zhong, and S. P. Alpay. Dielectric anomaly due to electrostatic coupling in ferroelectric- paraelectric bilayers and multilayers. *Appl. Phys. Lett.*, 87(9):092902–092904, 2005.

[138] P. Zubko, N. Stucki, C. Lichtensteiger, and J. M. Triscone. X-ray diffraction studies of 180 Ferroelectric ferroelectric domains in PbTiO3/SrTiO3 superlattices under an applied electric field. *Phys. Rev. Lett.*, 104(May):187601, 2010.

[139] Q Zou, H E Ruda, and B G Yacobi. Improved dielectric properties of lead zirconate titanate thin films deposited on metal foils with LaNiO3 buffer layers. *Appl. Phys. Lett.*, 78(9):1282–1284, feb 2001.

[140] V Reymond, D Michau, S Payan, and M Maglione. Substantial reduction of the dielectric losses of Ba0.6Sr0.4TiO3 thin films using a SiO2 barrier layer. *J. Phys. Condens. Matter*, 16(50):9155, 2004.

[141] Koji Aizawa, Byung-Eun Park, Yoshihito Kawashima, Kazuhiro Takahashi, and Hiroshi Ishiwara. Impact of HfO2 buffer layers on data retention characteristics of ferroelectric-gate field-effect transistors. *Appl. Phys. Lett.*, 85(15):3199–3201, 2004.

[142] Y. Lin, B. R. Zhao, H. B. Peng, B. Xu, H. Chen, F. Wu, H. J. Tao, Z. X. Zhao, and J. S. Chen. Growth and polarization features of highly (100) oriented Pb(Zr0.53Ti0.47)O3 films on Si with ultrathin SiO2 buffer layer. *Appl. Phys. Lett.*, 73(19):2781–2783, 1998.

[143] N Izyumskaya, Y.-I. Alivov, S.-J. Cho, H Morkoç, H Lee, and Y.-S. Kang. Processing, Structure, Properties, and Applications of PZT Thin Films. *Crit. Rev. Solid State Mater. Sci.*, 32(3-4):111–202, 2007.

[144] Hong-Cheng Li, Weidong Si, Alexander D West, and X X Xi. Thickness dependence of dielectric loss in SrTiO3 thin films. *Appl. Phys. Lett.*, 73(4):464–466, 1998.

[145] L. J. Sinnamon, R. M. Bowman, and J. M. Gregg. Investigation of dead-layer thickness in SrRuO3/Ba0.5Sr0.5TiO3/Au thin-film capacitors. *Appl. Phys. Lett.*, 78(12):1724–1726, 2001.

[146] B Chen, H Yang, L Zhao, J Miao, B Xu, X G Qiu, B R Zhao, X Y Qi, and X F Duan. Thickness and dielectric constant of dead layer in Pt/(Ba0.7Sr0.3)TiO3/YBa2Cu3O7-x capacitor. *Appl. Phys. Lett.*, 84(4):583–585, 2004.

[147] Takakiyo Harigai, Song-Min Nam, Hirofumi Kakemoto, Satoshi Wada, Keisuke Saito, and Takaaki Tsurumi. Structural and dielectric properties of perovskite-type artificial superlattices. *Thin Solid Films*, 509(12):13–17, 2006.

[148] F C Kartawidjaja, C H Sim, and J Wang. Ferroelectric and dielectric behavior of heterolayered PZT thin films. *J. Appl. Phys.*, 102:124102, 2007.

[149] Dinghua Bao. Multilayered dielectric/ferroelectric thin films and superlattices. *Curr. Opin. Solid State Mater. Sci.*, 12(34):55–61, 2008.

[150] Ming Liu, Jian Liu, Chunrui Ma, Gregory Collins, Chonglin Chen, Andy D Alemayehu, Guru Subramanyam, Jie He, Jiechao Jiang, Efstathios I Meletis, and Amar Bhalla. Enhanced dielectric properties of (Ba,Sr)TiO3//Ba(Zr,Ti)O3 heterostructures with optimized structure design. *CrystEngComm*, 15(34):6641–6644, 2013.

[151] M. B. Okatan, I. B. Misirlioglu, and S. P. Alpay. Contribution of space charges to the polarization of ferroelectric superlattices and its effect on dielectric properties. *Phys. Rev. B*, 82(9):094115–094121, 2010.

[152] Y. Y. Liu and J. Y. Li. Space charges and size effects in semiconducting ferroelectric BaTiO3/SrTiO3 superlattices. *Appl. Phys. Lett.*, 97(4):042905, 2010.

[153] Giovanni A Salvatore, Alexandru Rusu, and Adrian M Ionescu. Experimental confirmation of temperature dependent negative capacitance in ferroelectric field effect transistor. *Appl. Phys. Lett.*, 100:163504, 2012.

[154] Daniel J R Appleby, Nikhil K Ponon, Kelvin S K Kwa, Bin Zou, Peter K Petrov, Tianle Wang, Neil M Alford, and Anthony O'Neill. Experimental Observation of Negative Capacitance in Ferroelectrics at Room Temperature. *Nano Lett.*, 14(7):3864–3868, 2014.

[155] Muhammad Masuduzzaman and Muhammad Ashraful Alam. Effective Nanometer Airgap of NEMS Devices Using Negative Capacitance of Ferroelectric Materials. *Nano Lett.*, 14(6):3160–3165, 2014.

[156] Asif Islam Khan, Debanjan Bhowmik, Pu Yu, Sung Joo Kim, Xiaoqing Pan, Ramamoorthy Ramesh, and Sayeef Salahuddin. Experimental evidence of ferroelectric negative capacitance in nanoscale heterostructures. *Appl. Phys. Lett.*, 99(11):113501–113503, 2011.

[157] Weiwei Gao, Asif Khan, Xavi Marti, Chris Nelson, Claudy Serrao, Jayakanth Ravichandran, Ramamoorthy Ramesh, and Sayeef Salahuddin. Room-Temperature Negative Capacitance in a FerroelectricDielectric Superlattice Heterostructure. *Nano Lett.*, 14(10):5814–5819, 2014.

[158] M. B. Okatan, J. V. Mantese, and S. P. Alpay. Polarization coupling in ferroelectric multilayers. *Phys. Rev. B*, 79(17):174113, 2009.

[159] Shan Zhong, S P Alpay, A L Roytburd, and Joseph V Mantese. Interlayer coupling in ferroelectric bilayer and superlattice heterostructures. *Ultrason. Ferroelectr. Freq. Control. IEEE Trans.*, 53(12):2349–2356, dec 2006.

[160] F M Pontes, E R Leite, E Longo, J A Varela, E B Araujo, and J A Eiras. Effects of the postannealing atmosphere on the dielectric properties of (Ba, Sr)TiO3 capacitors: Evidence of an interfacial space charge layer. *Appl. Phys. Lett.*, 76(17):2433–2435, 2000.

[161] Jinwen Shi and Liejin Guo. ABO3-based photocatalysts for water splitting. *Prog. Nat. Sci. Mater. Int.*, 22(6):592–615, 2012.

[162] Huanping Zhou, Q. Qi Chen, Gang Li, Song Luo, Tze-bing T.-b. Song, Hsin-Sheng H.-S. Duan, Ziruo Hong, Jingbi You, Yongsheng Liu, and Yang Yang. Interface engineering of highly efficient perovskite solar cells. *Science (80-.).*, 345(6196):542–546, 2014.

[163] S. K. Sahoo, D. Misra, M. Sahoo, C. A. MacDonald, H. Bakhru, D. C. Agrawal, Y. N. Mohapatra, S. B. Majumder, and R. S. Katiyar. Improved dielectric properties and their temperature insensitivity in multilayered Ba0.8Sr0.2TiO3/ZrO2 thin films. *J. Appl. Phys.*, 109(6):064108–064113, 2011.

[164] Hui Chen, Tianquan Lü, Chuanwen Chen, and Wenwu Cao. Theoretical studies on the pyroelectric properties of two component composite ferroelectric thin film. *Phys. Lett. Sect. A Gen. At. Solid State Phys.*, 360:357–361, 2006.

[165] Ho Nyung Lee, Hans M Christen, Matthew F Chisholm, Christopher M Rouleau, and Douglas H Lowndes. Strong polarization enhancement in asymmetric three-component ferroelectric superlattices. *Nature*, 433:395–399, 2005.

[166] I. B. Misirlioglu, M. B. Okatan, and S. P. Alpay. Asymmetric hysteresis loops and smearing of the dielectric anomaly at the transition temperature due to space charges in ferroelectric thin films. *J. Appl. Phys.*, 108:034105, 2010.

[167] K Tashiro. Ferroelectric Polymers: Chemistry: Physics, and Applications. In Hari Singh Nalwa, editor, *Ferroelectr. Polym. Chem. Physics, Appl.*, pages 63–181. Marcel Dekker, New York, 1995.

[168] Andrew J Lovinger. Ferroelectric Polymers. *Science (80-.).*, 220:1115–1121, 1983.

[169] J F Legrand. Structure and ferroelectric properties of P(VDF-TrFE) copolymers. *Ferroelectrics*, 91:303–317, 1989.

[170] R. Costa, C. Ribeiro, A. C. Lopes, P. Martins, V. Sencadas, R. Soares, and S. Lanceros-Mendez. Osteoblast, fibroblast and in vivo biological response to poly(vinylidene fluoride) based composite materials. *J. Mater. Sci. Mater. Med.*, 24:395–403, 2013.

[171] J. Nunes-Pereira, A. C. Lopes, C. M. Costa, L. C. Rodrigues, M. M. Silva, and S. Lanceros-Méndez. Microporous membranes of NaY zeolite/poly(vinylidene fluoride- trifluoroethylene) for Li-ion battery separators. *J. Electroanal. Chem.*, 689:223–232, 2013.

[172] Yoseph Bar-Cohen and Qiming Zhang. Electroactive Polymer Actuators and Sensors. *MRS Bull.*, 33:173–181, 2008.

[173] P Martins, X Moya, L C Phillips, S Kar-Narayan, N D Mathur, and S Lanceros-Mendez. Linear anhysteretic direct magnetoelectric effect in Ni0.5Zn0.5Fe2O4/poly(vinylider fluoride-trifluoroethylene) 0-3 nanocomposites. *J. Phys. D. Appl. Phys.*, 44:482001–482004, 2011.

[174] P. Martins, a. C. Lopes, and S. Lanceros-Mendez. Electroactive phases of poly(vinylidene fluoride): Determination, processing and applications. *Prog. Polym. Sci.*, 39(4):683–706, 2014.

[175] C. S. Lee, J. Joo, S. Han, and S. K. Koh. Multifunctional transducer using poly (vinylidene fluoride) active layerand highly conducting poly (3,4-ethylenedioxythiophene) electrode: Actuator and generator. *Appl. Phys. Lett.*, 85(10):1841–1843, 2004.

[176] Kakimoto Ken-ichi, Fukata Keisuke, and Ogawa Hidetoshi. Fabrication of fibrous BaTiO3-reinforced PVDF composite sheet for transducer application. *Sensors Actuators A. Phys.*, 200:21–25, 2013.

[177] S Pamir Alpay, Joseph Mantese, Susan Trolier-McKinstry, Qiming Zhang, and Roger W Whatmore. Next-generation electrocaloric and pyroelectric materials for solid-state electrothermal energy interconversion. *MRS Bull.*, 39:1099–1111, 2014.

[178] Dong Jun Li, Seungbum Hong, Shiyuan Gu, YoonYoung Choi, Serge Nakhmanson, Olle Heinonen, Dmitry Karpeev, and Kwangsoo No. Polymer piezoelectric energy harvesters for low wind speed. *Appl. Phys. Lett.*, 104:012902–012905, 2014.

[179] Takeo Furukawa. Ferroelectric properties of vinylidene fluoride copolymers. *Phase Transitions*, 18(3-4):143–211, 1989.

[180] Alexandru D Asandei, Christopher P Simpson, Olumide I Adebolu, and Yanhui Chen. *Towards Metal Mediated Radical Polymerization of Vinylidene Fluoride*, chapter 5, pages 47–63. American Chemical Society, 2012.

[181] Alexandru D Asandei, Olumide I Adebolu, and Christopher P Simpson. Mild-temperature Mn2(CO)10-photomediated controlled radical polymerization of vinylidene fluoride and synthesis of well-defined poly(vinylidene fluoride) block copolymers. *J. Am. Chem. Soc.*, 134:6080–6083, 2012.

[182] Alexandru D. Asandei, Olumide I. Adebolu, Christopher P. Simpson, and Joon Sung Kim. Visible-light hypervalent iodide carboxylate photo(trifluoro)methylations and controlled radical polymerization of fluorinated alkenes. *Angew. Chemie - Int. Ed.*, 52:10027–10030, 2013.

[183] A. D. Asandei, Olumide I. Adebolu, and C. P. Simpson. *Handbook of fluoropolymer science and technology*. John Wiley & Sons, Inc., 2014.

[184] Heiji Kawai. The Piezoelectricity of Poly (vinylidene Fluoride). *Jpn. J. Appl. Phys.*, 8:975–976, 1969.

[185] J. G. Bergman, J. H. McFee, and G. R. Crane. Pyroelectricity and optical second harmonic generation in polyvinylidene fluoride films. *Appl. Phys. Lett.*, 18:203–205, 1971.

[186] Ryozo Hasegawa, Yasuhiro Takahashi, Yozo Chatani, and Hiroyuki Tadokoro. Crystal Structures of Three Crystalline Forms of Poly(vinylidene fluoride). *Polym. J.*, 3:600–610, 1972.

[187] Andrew J Lovinger. Unit cell of the γ phase of poly(vinylidene fluoride). *Macromolecules*, 14(2):322–325, 1981.

[188] M. Bachmann, W. L. Gordon, S. Weinhold, and J. B. Lando. The crystal structure of phase IV of poly(vinylidene fluoride). *J. Appl. Phys.*, 51(1980):5095–5099, 1980.

[189] V Sencadas, R Gregorio, and S Lanceros-Mendez. α to β phase transformation and microestructural changes of PVDF films induced by uniaxial stretch. *J. Macromol. Sci. Part B*, 48:514–525, 2009.

[190] G. T. Davis, J. E. McKinney, M. G. Broadhurst, and S. C. Roth. Electric-field-induced phase changes in poly(vinylidene fluoride). *J. Appl. Phys.*, 49(1978):4998–5002, 1978.

[191] S Weinhold, M H Litt, and B Lando. The crystal structure of the gamma phase of poly(vinylidene fluoride). *Am. Chem. Soc.*, 13:1178–1183, 1980.

[192] Mengyuan Li, Harry J Wondergem, Mark-Jan Spijkman, Kamal Asadi, Ilias Katsouras, Paul W M Blom, and Dago M de Leeuw. Revisiting the δ-phase of poly(vinylidene fluoride) for solution-processed ferroelectric thin films. *Nat. Mater.*, 12(14):433–438, 2013.

[193] Tosiharu Yagi, Masayoshi Tatemoto, and Jun-ichi Sako. Transition behavior and dielectric properties in trifluorethylene and vinylidene fluoride copolymers. *Polym. J.*, 12:209–223, 1980.

[194] Keiko Koga and Hiroji Ohigashi. Piezoelectricity and related properties of vinylidene fluoride and trifluoroethylene copolymers. *J. Appl. Phys.*, 59(1986):2142–2150, 1986.

[195] Haruko Kakutani. Dielectric absorption in oriented poly(vinylidene fluoride). *J. Polym. Sci. Part A-2 Polym. Phys.*, 8:1177–1186, 1970.

[196] R. Al-Jishi and P. L. Taylor. Equilibrium polarization and piezoelectric and pyroelectric coefficients in poly(vinylidene fluoride). *J. Appl. Phys.*, 57(3):902–905, 1985.

[197] C. K. Purvis and P. L. Taylor. Piezoelectricity and pyroelectricity in polyvinylidene fluoride: Influence of the lattice structure. *J. Appl. Phys.*, 54(2):1021–1028, 1983.

[198] Zhi-Yin Wang, Ke-He Su, Hui-Qing Fan, and Zhen-Yi Wen. Structure and electric properties of poly(vinylidene fluoride-tetrafluoroethylene) copolymer studied with density functional theory. *Polymer (Guildf).*, 48(24):7145–7155, 2007.

[199] Martin Bohlén and Kim Bolton. Conformational studies of poly(vinylidene fluoride), poly(trifluoroethylene) and poly(vinylidene fluoride-co-trifluoroethylene) using density functional theory. *Phys. Chem. Chem. Phys.*, 16:12929–12939, 2014.

[200] Yong Pei and Xiao Cheng Zeng. Elastic properties of poly(vinyldene fluoride) (PVDF) crystals: A density functional theory study. *J. Appl. Phys.*, 109:093514–093520, 2011.

[201] Naoki Karasawa and William A. Goddard III. Force fields, structures, and properties of poly(vinylidene fluoride) crystals. *Macromolecules*, 25:7268–7281, 1992.

[202] Jeffrey D Carbeck, Daniel J Lacks, and Gregory C Rutledge. A model of crystal polarization in βpoly(vinylidene fluoride). *J. Chem. Phys.*, 103:10347–10355, 1995.

[203] Jeffrey D Carbeck and Gregory C Rutledge. Temperature dependent elastic, piezoelectric and pyroelectric properties of β-poly(vinylidene fluoride) from molecular simulation. *Polymer (Guildf).*, 37:5089–5097, 1996.

[204] K. Tashiro, Y. Abe, and M. Kobayashi. Computer simulation of structure and ferroelectric phase transition of vinylidene fluoride copolymers (1) vdf content dependence of the crystal structure. *Ferroelectrics*, 171:281–297, 1995.

[205] Y. Abe and K. Tashiro. Computer simulation of structure and ferroelectric phase transition of vinylidene fluoride copolymers. *Polymer (Guildf).*, 42:3409–3417, 2001.

[206] Y Abe and K Tashiro. Computer simulation of structure and ferroelectric phase transition of vinylidene fluoride copolymers. 5. Influence of orientational disorder of dipole moments and domain walls on phase transitional behavior. *Polymer (Guildf).*, 42:9671–9678, 2001.

[207] Y. Abe and K. Tashiro. Computer simulation of structure and ferroelectric phase transition of vinylidene fluoride copolymers. IV. the factors governing the ferroelectric phase transition of VDF-TrFE copolymers. *J. Polym. Sci. Part B Polym. Phys.*, 39:689–702, 2001.

[208] N. Neumann, R. Köhler, and G. Hofmann. Pyroelectric thin film sensors and arrays based on P(VDF/TrFE). *Integr. Ferroelectr.*, 6(1-4):213–230, 1995.

[209] Y Abe, K Tashiro, and M Kobayashi. Computer simulation of structural changes in the ferroelectric phase transition of vinylidene fluoridetrifluoroethylene copolymers. *Comput. Theor. Polym. Sci.*, 10:323–333, 2000.

[210] Andrew Jewett and Jason Lambert. Moltemplate (Version 1.29) [Computer software], 2015.

[211] Bruno Ameduri. From Vinylidene Fluoride (VDF) to the Applications of VDF-Containing Polymers and Copolymers: Recent Developments and Future Trends. *Chem. Rev.*, 109(12):6632–6686, 2009.

[212] Steve Plimpton. Fast Parallel Algorithms for Short-Range Molecular Dynamics. *J. Comput. Phys.*, 117(1):1–19, 1995.

[213] M Parrinello and A Rahman. Polymorphic transitions in single crystals: A new molecular dynamics method. *J. Appl. Phys.*, 52(12):7182–7190, 1981.

[214] William G Hoover. Canonical dynamics: Equilibrium phase-space distributions. *Phys. Rev. A*, 31(3):1695–1697, 1985.

[215] Shuichi Nosé. A unified formulation of the constant temperature molecular dynamics methods. *J. Chem. Phys.*, 81(1):511–519, 1984.

[216] J F Nye. *Physical Properties of Crystals: Their Representation by Tensors and Matrices*. Oxford science publications. Clarendon Press, 1985.

[217] Haibin B. Su, Alejandro Strachan, and William A. Goddard. Density Functional Theory and Molecular Dynamics Studies on Energetics and Kinetics for Electro-Active Polymers: PVDF and P(VDF-TrFE). *Phys. Rev. B*, 70(6):064101–064108, 2004.

[218] J B Lando, H G Olf, and A Peterlin. Nuclear magnetic resonance and x-ray determination of the structure of poly(vinylidene fluoride). *J. Polym. Sci. Part A-1 Polym. Chem.*, 4(4):941–951, 1966.

[219] Serge M. Nakhmanson, R. Korlacki, J. Travis Johnston, Stephen Ducharme, Zhongxin Ge, and James M. Takacs. Vibrational properties of ferroelectric β-vinylidene fluoride polymers and oligomers. *Phys. Rev. B*, 81:174120–174127, may 2010.

[220] Kenji Omote, Hiroji Ohigashi, and Keiko Koga. Temperature dependence of elastic, dielectric, and piezoelectric properties of single crystalline" films of vinylidene fluoride trifluoroethylene copolymer. *J. Appl. Phys.*, 81:2760, 1997.

[221] Kohji Tashiro, Masamichi Kobayashi, Hiroyuki Tadokoro, and Eiichi Fukada. Calculation of Elastic and Piezoelectric Constants. *Macromolecules*, 13:691–698, 1980.

[222] Ichiro Sakurada and Keisuke Kaji. relation between the polymer conformation and the elastic modulus of the crystalline region of polymer. *J. Polym. Sci. Part C Polym. Symp.*, 31(1):57–76, 1970.

[223] R F Schaufele and T Shimanouchi. Longitudinal Acoustical Vibrations of Finite Polymethylene Chains. *J. Chem. Phys.*, 47(9):3605–3610, 1967.

[224] A V Bune, Chuanxing Zhu, Stephen Ducharme, L M Blinov, V M Fridkin, S P Palto, N G Petukhova, and S G Yudin. Piezoelectric and pyroelectric properties of ferroelectric LangmuirBlodgett polymer films. *J. Appl. Phys.*, 85(11):7869–7873, 1999.

[225] H. H S Chang and Z. Huang. Pyroelectric effect enhancement through product property under open circuit condition. *J. Appl. Phys.*, 106:014101–014109, 2009.

[226] T. Furukawa, G. E. Johnson, H. E. Bair, Y. Tajitsu, A. Chiba, and E. Fukada. Ferroelectric phase transition in a copolymer of vinylidene fluoride and trifluoroethylene. *Ferroelectrics*, 32:61–67, 1981.

[227] T. Furukawa and G. E. Johnson. Measurements of ferroelectric switching characteristics in polyvinylidene fluoride. *Appl. Phys. Lett.*, 38(12):1027–1029, 1981.

[228] F. J. Baltá Calleja, A. González Arche, T. A. Ezquerra, C. Santa Cruz, F. Batallán, B. Frick, and E. López Cabarcos. Structure and Properties of Ferroeletric Copolymers of Poly(Vinylidene Fluoride). *Adv. Polym. Sci.*, 108:1–48, 1993.

[229] Kohji Tashiro, Kohji Takano, Masamichi Kobayashi, Yozo Chatani, and Hiroyuki Tadokoro. Structure and ferroelectric phase transition of vinylidene fluoride-trifluoroethylene copolymers: 2. VDF 55% copolymer. *Polymer (Guildf).*, 25(2):195–208, 1984.

[230] Li Li, Mingqiu Zhang, Minzhi Rong, and Wenhong Ruan. Studies on the transformation process of PVDF from α to β phase by stretching. *RSC Adv.*, 4(8):3938, 2014.

[231] R.C. Oliveira, L.S. Cavalcante, J.C. Sczancoski, E.C. Aguiar, J.W.M. Espinosa, J.a. Varela, P.S. Pizani, and E. Longo. Synthesis and photoluminescence behavior of Bi4Ti3O12 powders obtained by the complex polymerization method. *J. Alloys Compd.*, 478(1-2):661–670, 2009.

[232] Amritendu Roy, Rajendra Prasad, Sushil Auluck, and Ashish Garg. Engineering polarization rotation in ferroelectric bismuth titanate. *Appl. Phys. Lett.*, 102(18):182901, 2013.

[233] S H Shah and P D Bristowe. Ab initio energetics of lanthanum substitution in ferroelectric bismuth titanate. *J. Phys. Condens. Matter*, 23(15):155902, 2011.

[234] A. T. Zayak, P. Entel, K. M. Rabe, W. A. Adeagbo, and M. Acet. Anomalous vibrational effects in nonmagnetic and magnetic Heusler alloys. *Phys. Rev. B*, 72:054113, 2005.

[235] Wenbo Li, Shaozhen Ma, Zhe Chen, and Niloy K. Dutta. All-optical logic gates based on two-photon absorption in semiconductor optical amplifiers. *J. Opt. Soc. Am. B*, 29:2603–2609, 2012.

[236] Wenbo Li, Shaozhen Ma, Hongyu Hu, and Niloy K. Dutta. All optical latches using quantum-dot semiconductor optical amplifier. *Opt. Commun.*, 285(24):5138–5143, 2012.

[237] A. B. Missyul, I. A. Zvereva, T. T M Palstra, and A. I. Kurbakov. Double-layered Aurivillius-type ferroelectrics with magnetic moments. *Mater. Res. Bull.*, 45(5):546–550, 2010.

[238] N Ortega, Ashok Kumar, J F Scott, and Ram S Katiyar. Multifunctional magnetoelectric materials for device applications. *J. Phys. Condens. Matter*, 27(50):504002, 2015.

[239] B. H. Park, B. S. Kang, S. D. Bu, T. W. Noh, J. Lee, and W. Jo. Lanthanum-substituted bismuth titanate for use in non-volatile memories. *Nature*, 401(6754):682–684, 1999.

[240] J. F. Scott. High-Dielectric Constant Thin Films for Dynamic Random Access Memories (Dram). *Annu. Rev. Mater. Sci.*, 28(1):79–100, 1998.

[241] Xiaobo Chen, Shaohua Shen, Liejin Guo, and Samuel S Mao. Semiconductor-based Photocatalytic Hydrogen Generation. *Chem. Rev.*, 110:6503, 2010.

[242] Wei F. Yao, Hong Wang, Xiao H. Xu, Shu X. Shang, Yun Hou, Yin Zhang, and Min Wang. Synthesis and photocatalytic property of bismuth titanate Bi4Ti3O12. *Mater. Lett.*, 57(13-14):1899–1902, 2003.

[243] Seung-Jin Oh, Yiseul Shin, T Thao Tran, Dong Woo Lee, Anne Yoon, P Shiv Halasyamani, and Kang Min Ok. Structure-property relationships in solid solutions of noncentrosymmetric Aurivillius phases, Bi(4-x)La(x)Ti3O12 (x = 0-0.75). *Inorg. Chem.*, 51(19):10402–7, 2012.

[244] Su Jae Kim, Chikako Moriyoshi, Sayaka Kimura, Yoshihiro Kuroiwa, Kenichi Kato, Masaki Takata, Yuji Noguchi, and Masaru Miyayama. Direct observation of oxygen stabilization in layered ferroelectric Bi3.25La0.75Ti3O12. *Appl. Phys. Lett.*, 91(6):062913, 2007.

[245] A. D. Rae, J. G. Thompson, R. L. Withers, and A. C. Willis. Structure refinement of commensurately modulated bismuth titanate, Bi4Ti3O12. *Acta Crystallogr. Sect. B Struct. Sci.*, 46(4):474–487, 1990.

[246] Min Ku Jeon, Yong-Il Kim, Seung-Hoon Nahm, Jung Min Sohn, Chang Hwa Jung, and Seong Ihl Woo. Studied By Using Neutron Powder Diffraction Data. *J. Phys. D. Appl. Phys.*, 40(15):4647–4652, 2007.

[247] J. M. Perez-Mato, P. Blaha, K. Schwarz, M. Aroyo, D. Orobengoa, I. Etxebarria, and Alberto García. Multiple instabilities in Bi4Ti3O12: A ferroelectric beyond the soft-mode paradigm. *Phys. Rev. B*, 77:184104, 2008.

[248] Uong Chon, Hyun M Jang, M G Kim, and C H Chang. Layered perovskites with giant spontaneous polarizations for nonvolatile memories. *Phys. Rev. Lett.*, 89(8):087601, 2002.

[249] Yuji Noguchi, Masayuki Soga, Masatake Takahashi, and Masaru Miyayama. Oxygen stability and leakage current mechanism in ferroelectric La-substituted Bi4Ti3O12 single crystals. *Japanese J. Appl. Physics, Part 1 Regul. Pap. Short Notes Rev. Pap.*, 44(9 B):6998–7002, 2005.

[250] T. Hashimoto and H. Moriwake. Oxygen vacancy formation energy and its effect on spontaneous polarization in Bi4Ti3O12: A first-principles theoretical study. *Phys. Rev. B*, 78:092106, 2008.

[251] Yuji Noguchi, Masaru Miyayama, and Tetsuichi Kudo. Direct evidence of A-site-deficient strontium bismuth tantalate and its enhanced ferroelectric properties. *Phys. Rev. B*, 63(21):214102, 2001.

[252] Yuji Noguchi, Ichiro Miwa, Yu Goshima, and Masaru Miyayama. Defect control for large remanent polarization in bismuth titanate ferroelectrics - doping effect of higher-valent cations. *Jpn. J. Appl. Phys.*, 39:L1259, 2000.

[253] Eric J. Nichols, Jiawanjun Shi, Ashfia Huq, Sven C. Vogel, and Scott T. Misture. Controlling structure distortions in 3-layer ferroelectric Aurivillius oxides. *J. Solid State Chem.*, 197:475–482, 2013.

[254] Stefano Baroni, Paolo Giannozzi, and Andrea Testa. Green's-function approach to linear response in solids. *Phys. Rev. Lett.*, 58:1861, 1987.

[255] R. D. King-Smith and David Vanderbilt. Theory of polarization of crystalline solids. *Phys. Rev. B*, 47(3):1651–1654, 1993.

[256] David Vanderbilt and R. D. King-Smith. Electric polarization as a bulk quantity and its relation to surface charge. *Phys. Rev. B*, 48(7):4442–4455, 1993.

[257] Nicola A Spaldin. A beginner's guide to the modern theory of polarization. *J. Solid State Chem.*, 195:2–10, 2012.

[258] J. B. Neaton, C. Ederer, U. V. Waghmare, N. A. Spaldin, and K. M. Rabe. First-principles study of spontaneous polarization in multiferroic BiFeO3. *Phys. Rev. B*, 71:014113, 2005.

[259] Qingdi Zhou, Brendan J. Kennedy, and Christopher J. Howard. Structural Studies of the Ferroelectric Phase Transition in Bi4Ti3O12. *Chem. Mater.*, 15(26):5025–5028, 2003.

[260] Anurag Shrinagar, Ashish Garg, Rajendra Prasad, and Sushil Auluck. Phase stability in ferroelectric bismuth titanate: A first-principles study. *Acta Crystallogr. Sect. A Found. Crystallogr.*, 64(3):368–375, 2008.

[261] Amritendu Roy, Rajendra Prasad, Sushil Auluck, and Ashish Garg. First-principles calculations of Born effective charges and spontaneous polarization of ferroelectric bismuth titanate. *J. Phys. Condens. Matter*, 22(16):165902, 2010.

[262] Charles H Hervoches and Philip Lightfoot. A Variable-Temperature Powder Neutron Diffraction Study of Ferroelectric Bi4Ti3O12. *Chem. Mater.*, 11:3359–3364, 1999.

[263] Hania Djani, Eric Bousquet, Abdelhafid Kellou, and Philippe Ghosez. First-principles study of the ferroelectric Aurivillius phase Bi2WO6. *Phys. Rev. B*, 86(5):054107, 2012.

[264] J F Scott. Applications of modern ferroelectrics. *Science*, 315(5814):954–959, 2007.

[265] S. E. Cummins and L. E. Cross. Crystal symmetry, optical properties, and ferroelectric polarization of Bi4Ti3O12 single crystals. *Appl. Phys. Lett.*, 10(1):14–16, 1967.

[266] R A Armstrong and R E Newnham. Bismuth titanate solid solutions. *Mater. Res. Bull.*, 7(10):1025–1034, 1972.

[267] Woo Seok Choi, Matthew F. Chisholm, David J. Singh, Taekjib Choi, Gerald E. Jellison, and Ho Nyung Lee. Wide bandgap tunability in complex transition metal oxides by site-specific substitution. *Nat. Commun.*, 3:689, 2012.

[268] M S Tomar, R E Melgarejo, A Hidalgo, S B Mazumder, and R S Katiyar. Structural and ferroelectric studies of Bi3.44La0.56Ti3O12 films. *Appl. Phys. Lett.*, 83:341, 2003.

[269] David Singh, Sung Seo, and Ho Lee. Optical properties of ferroelectric Bi4Ti3O12. *Phys. Rev. B*, 82:180103, 2010.

[270] Woo Seok Choi and Ho Nyung Lee. Band gap tuning in ferroelectric Bi4Ti3O12 by alloying with LaTMO3 (TM = Ti, V, Cr, Mn, Co, Ni, and Al). *Appl. Phys. Lett.*, 100(13):132903, 2012.

[271] Jun Young Han and Chung Wung Bark. Influence of transition metal doping (X = Co, Fe) on structural, optical properties of Ferroelectric Bi3.25La0.75X1Ti2O12. *Nano Converg.*, 2:1, 2015.

[272] Jun Young Han and Chung Wung Bark. Structural and optical properties of Fe doped bismuth titanate thin film deposited by RF sputtering Structural. *Jpn. J. Appl. Phys.*, 55:02BC09, 2016.

[273] G. Kresse and J. Hafner. Ab initio molecular dynamics for open-shell transition metals. *Phys. Rev. B*, 48(17):13115–13118, 1993.

[274] Hendrik J. Monkhorst and James D. Pack. Special points for Brillouin-zone integrations. *Phys. Rev. B*, 13(12):5188–5192, 1976.

[275] D. I. Bilc, R. Orlando, R. Shaltaf, G. M. Rignanese, Jorge Íñiguez, and Ph Ghosez. Hybrid exchange-correlation functional for accurate prediction of the electronic and structural properties of ferroelectric oxides. *Phys. Rev. B*, 77:165107, 2008.

[276] Jochen Heyd, Gustavo E. Scuseria, and Matthias Ernzerhof. Hybrid functionals based on a screened Coulomb potential. *J. Chem. Phys.*, 118(18):8207–8215, 2003.

[277] J. Paier, M. Marsman, K. Hummer, G. Kresse, I. C. Gerber, and J. G. Angyán. Screened hybrid density functionals applied to solids. *J. Chem. Phys.*, 124:154709, 2006.

[278] Kerstin Hummer, Judith Harl, and Georg Kresse. Heyd-Scuseria-Ernzerhof hybrid functional for calculating the lattice dynamics of semiconductors. *Phys. Rev. B*, 80(11):115205, 2009.

[279] Caihong Jia, Yonghai Chen, and W. F. Zhang. Optical properties of aluminum-, gallium-, and indium-doped Bi4Ti3O12 thin films. *J. Appl. Phys.*, 105:113108, 2009.

[280] J Padilla, W Zhong, and D Vanderbilt. First-principles investigation of 180 domain walls in BaTiO3. *Phys. Rev. B*, 53(10):R5969–R5973, 1996.

[281] David Vanderbilt. First-principles based modelling of ferroelectrics. *Curr. Opin. Solid State Mater. Sci.*, 2(6):701–705, 1997.

[282] Lixin He and David Vanderbilt. First-principles study of oxygen-vacancy pinning of domain walls in PbTiO3. *Phys. Rev. B*, 68:134103, 2003.

[283] Anand Chandrasekaran, Dragan Damjanovic, Nava Setter, and Nicola Marzari. Defect ordering and defect-domain-wall interactions in PbTiO3: A first-principles study. *Phys. Rev. B*, 88:214116, 2013.

[284] T Zhao, a Scholl, F Zavaliche, K Lee, M Barry, a Doran, M P Cruz, Y H Chu, C Ederer, N a Spaldin, R R Das, D M Kim, S H Baek, C B Eom, and R Ramesh. Electrical control of antiferromagnetic domains in multiferroic BiFeO3 films at room temperature. *Nat. Mater.*, 5(10):823–9, 2006.

[285] Ying-Hao Chu, Lane W Martin, Mikel B Holcomb, Martin Gajek, Shu-Jen Han, Qing He, Nina Balke, Chan-Ho Yang, Donkoun Lee, Wei Hu, Qian Zhan, Pei-Ling Yang, Arantxa Fraile-Rodríguez, Andreas Scholl, Shan X Wang, and R Ramesh. Electric-field control of local ferromagnetism using a magnetoelectric multiferroic. *Nat. Mater.*, 7(6):478–82, 2008.

[286] K. M. Rabe and U. V. Waghmare. Ferroelectric Phase Transitions from First Principles. *J. Phys. Chem. Solids*, 57:1397, 1995.

[287] L. Bellaiche. Piezoelectricity of ferroelectric perovskites from first principles. *Curr. Opin. Solid State Mater. Sci.*, 6:19–25, 2002.

[288] M. Sepliarsky, A. Asthagiri, S. R. Phillpot, M. G. Stachiotti, and R. L. Migoni. Atomic-level simulation of ferroelectricity in oxide materials. *Curr. Opin. Solid State Mater. Sci.*, 9(3):107–113, 2005.

[289] William A. Goddard III, Qingsong Zhang, Mustafa Uludogan, Alejandro Strachan, and Tahir Cagin. The ReaxFF Polarizable Reactive Force Fields for Molecular Dynamics Simulation of Ferroelectrics. *AIP Conf. Proc.*, 626:45–55, 2002.

[290] I. Ponomareva, I. Naumov, I. Kornev, H. Fu, and L. Bellaiche. Modelling of nanoscale ferroelectrics from atomistic simulations. *Curr. Opin. Solid State Mater. Sci.*, 9(3):114–121, 2005.

[291] Young-Han Shin, Ilya Grinberg, I-Wei Chen, and Andrew M Rappe. Nucleation and growth mechanism of ferroelectric domain-wall motion. *Nature*, 449(7164):881–884, 2007.

[292] Menglei Li, Yijia Gu, Yi Wang, Long-Qing Chen, and Wenhui Duan. First-principles study of 180 domain walls BaTiO3: Mixed Bloch-Néel-Ising character. *Phys. Rev. B*, 90(5):054106, 2014.

[293] R. Guo, L. E. Cross, S-E. Park, B. Noheda, D. E. Cox, and G. Shirane. Origin of the high piezoelectric response in PbZr1-xTixO3. *Phys. Rev. Lett.*, 84(23):5423–5426, 2000.

[294] Oliver Gindele, Anna Kimmel, Markys G. Cain, and Dorothy Duffy. Shell Model force field for Lead Zirconate Titanate Pb(Zr1-xTix)O3. *J. Phys. Chem. C*, 119(31):17784–17789, 2015.